Author:
Kao, Min-Hsien

Title:
Photochemical reaction dynamics of organic chromophores in solution investigated with ultrafast transient absorption spectroscopy

Photochemical Reaction Dynamics of Organic Chromophores in Solution Investigated with Ultrafast Transient Absorption Spectroscopy

Min-Hsien Kao

A dissertation submitted to the University of Bristol in accordance with the requirement of the degree of Doctor of Philosophy in the School of Chemistry, Faculty of Science.

July 2021

Word count: ~26,000

Abstract

The photochemical dynamics of various organic molecules in solution are investigated using ultrafast transient electronic and vibrational absorption spectroscopy to explore the effects of molecular structure and solvent environment on the photochemical reaction pathways. First, the influence of ring strain on photoinduced ring opening of cyclic ketones is revealed by using different excitation energies to reach the first excited electronic singlet (S_1) states of cyclobutanone, cyclopentanone and cyclohexanone. The fraction of the excited state population undergoing ultrafast ring opening in <1 ps increased with greater ring strain in the cyclic ketones and with higher excitation energies, both of which help to overcome the energy barrier to C-C bond breaking. Furthermore, the lifetimes of the S_1 states were found to be shorter for smaller ring sizes. The excited-state dynamics of a photoexcited sunscreen molecule, diethylamino hydroxybenzoyl hexyl benzoate, were then studied in four different solvents. The competition between alternative relaxation pathways involving enol-keto tautomerization and central C-C bond twisting showed a clear solvent-dependence, with the former favoured in non-polar solvents, and the latter in polar and protic solvents. Moreover, the choice of solvent played a role in the ground-state recovery rate, and in the likelihood of populating the DHHB triplet states which could sensitise other molecules used in sunscreen formulations. Finally, progress is reported with an ongoing studying on phenyl cation generation from the photodissociation of chlorobenzene, motivated by new strategies for N_2 activation photochemistry. The photoexcitation was performed in two solvents, cyclohexane and perfluorohexane. Transient absorption bands at wavelengths of 500 - 600 nm, prominent in the non-reactive perfluorohexane solvent, identified an intermediate species proposed to be a complex with charge-transfer character corresponding to a phenyl cation and a chloride anion. Future work will seek further evidence for the chemical nature of the intermediate from transient IR spectroscopy.

Covid-19 statement

The coronavirus pandemic has caused national lockdowns in the UK in 2020 and 2021. Access to the research laboratories in the School of Chemistry was revoked from March to June 2020, and access to the postgraduate offices was revoked from March to October 2020. Since October 2020, the numbers of people being in the laboratories and offices are limit. As a result, data collection for the project described in Chapter 5 was stopped, and the inconvenience of working from home held up the data analysis.

Acknowledgement

I would like to appreciate my supervisor, Andrew Orr-Ewing, for his patience and guidance on physical chemistry, laser systems, writing journal articles and so on. He not only supports me in scientific research, but also shows consideration for my mental health especially during the pandemic. I felt lucky to meet him and Mike Ashfold while they were in Taipei for a conference and to have joined the Bristol Laser Group. Thank you also to Mike Ashfold and Tom Oliver for their constructive advice on my studies and optics for the laser system.

I wish to offer my thanks to the people in the Bristol Laser Group, especially Ravi Kumar Venkatraman, Mahima Sneha and Aditi Bhattacherjee for teaching me how to do laser experiments; Ryan Phelps and Georgia Thornton for being great company in the lab and office. Finally, I wish to thank my family and friends in Taiwan although I am afraid that I will not mention their names here because I do not know their English names. Thank you to my parents for the financial and mental support, and sorry that I could not be around much. Thank you to my siblings for chatting and gossiping with me weekly so that I do not feel like being left out. Thank you to my friends for occasional catching up and sparing their time to hang out with me while I go back to Taiwan on holidays.

Author’s declaration

I declare that the work in this dissertation was carried out in accordance with the requirements of the University's Regulations and Code of Practice for Research Degree Programmes and that it has not been submitted for any other academic award. Except where indicated by specific reference in the text, the work is the candidate's own work. Work done in collaboration with, or with the assistance of, others, is indicated as such. Any views expressed in the dissertation are those of the author.

SIGNED: Min-Hsien Kao DATE: 15th July 2021

Table of Contents

List of Figures

Chapter 6

List of Tables

Chapter 3

Chapter 4

Chapter 1. Introduction

This thesis presents the outcomes of research examining the ultrafast photochemical pathways in selected organic molecules: cyclic ketones, a sunscreen molecule, and chlorobenzene, all dissolved in organic solvents. The influences of the molecular structures and the solution environments on the photochemical pathways are investigated. The dynamics of the photochemistry are unravelled using transient absorption spectroscopy (TAS) with ~ 100 fs time resolution, combined with calculations of the ground and excited electronic state properties. This chapter introduces ultrafast photochemistry, the photochemical reactions of carbonyl compounds, the photochemistry of sunscreen molecules, the properties of the phenyl cation (posited to be a photoproduct of chlorobenzene), and the principles of transient absorption spectroscopy.

1.1 Ultrafast photochemistry and potential energy surfaces

Modern ultrafast spectroscopy of photochemical pathways in molecules employs so-called pump-and-probe methods in which the evolution of excited state population generated by the pump pulse of light is monitored by probe pulses at various different time delays. This strategy developed from the flash photolysis method of George Porter and Ronald Norrish, for which they were awarded a part of the Nobel Prize for Chemistry in 1967,[1] and which initiated research into the kinetics of photochemical reactions occurring on microsecond timescales. Ahmed Zewail and coworkers pioneered the observation of femtosecond dynamics of wavepacket motion in the gas phase, for example for I_2-Xe leading to formation of Xe-I, and Zewail was honored with the Nobel Prize for Chemistry in 1999.[2, 3] At about the same time, Fleming and coworkers pioneered the observation of wavepacket motion of iodine in an *n*-hexane solution.[4] Studies of ultrafast chemical dynamics in gases, liquids and solids have since multiplied, and various problems in molecular photochemistry such as dissociation, isomerization and charge/proton transfer have been investigated.[5-11]

$$i\frac{\partial}{\partial t}\Psi(R,r,t) = \hat{H}\Psi(R,r,t)$$

Equation 1-1

Chemical reactions involve changes of molecular geometries and energies, and are described quantum-mechanically by the time-dependent Schrödinger equations (Equation 1-1), where R and r are coordinates of all the nuclei and electrons. The molecular Hamiltonian, $\hat{H}$, includes operators for the nuclear kinetic energy ($\hat{T}_N$), the electron kinetic energy ($\hat{T}_e$), the Coulomb attraction of the nuclei and electrons ($\hat{V}_{Ne}$), and the electron-electron and nuclei-nuclei Coulomb repulsions, ($\hat{V}_{ee}$) and ($\hat{V}_{NN}$) respectively. However, it is impossible to obtain an exact solution for any molecule consisting of three particles or more. Therefore, Born and Oppenheimer introduced an approximation to treat the nuclear and electronic motions separately because of the considerable mass difference between a nucleus and an electron,[12] so nuclei are considered to remain stationary on the timescales for electron motion. Therefore, the nuclear kinetic energy can be separated from the motion of the electrons, giving rise to an electronic Hamiltonian, $\hat{H}_e$. Under the Born-Oppenheimer (BO) approximation, the electronic time-independent Schrödinger equation (Equation 1-2) for an electronic state *i* can then be solved by treating the nuclear coordinates as parametric constants. In this expression, $E_i(R)$ is the electronic energy and depends on the assumed nuclear positions. Relative to the nuclear motions, the electrons move rapidly and adjust to

$$\hat{H}_e \psi_{e,i}(r;R) = E_i(R)\psi_{e,i}(r;R)$$

Equation 1-2

the changes of nuclear coordinates essentially immediately, so the resulting time-independent Schrödinger equation for nuclear motion is shown in Equation 1-3. The $\hat{H}_N$

$$\hat{H}_N \phi_{N,i}(R) = E_{tot}\phi_{N,i}(R)$$

Equation 1-3

operator contains the nuclear kinetic energy and the electronic energy, and the total energy, E_{tot}, is the sum of translational, rotational, vibrational, and electronic energies. Solving Equations 1-3 and 1-2 can, respectively, obtain quantum information for the rotational and vibrational motions of a molecule, and the potential energy surfaces (PES) over which chemical reactions happen.

The BO approximation, also known as the adiabatic approximation, is usually good when the motions of the electrons and nuclei are not coupled, but it breaks down when two or more states are coupled and energetically close. The coupling of two electronic states can provide a pathway between them known as a conical intersection (CI), and these features often

participate prominently in photochemical reactions such as photodissociation and non-radiative relaxation after photoexcitation.[13] These concepts of nuclear dynamics on PESs coupled via conical intersections are central to the work presented in this thesis. The following sections provide some context by summarizing the known photochemistry of the classes of compounds examined, with further details provided in the introductory sections to Chapters 3 – 5.

1.2 Photochemistry of carbonyl compounds

Carbonyl groups are common chromophores in organic molecule photochemistry, and feature prominently in the systems described in this thesis. The photochemistry of aldehydes and ketones was studied by Norrish *et al.*, and they concluded that there were two types of photochemical reactions involving carbonyl functional groups.[14-17] A Norrish type I reaction is α-cleavage in which a C-C α-bond (with respect to the carbonyl group) breaks homolytically into radicals, and is usually followed by CO elimination (Figure 1-1a). A Norrish type II process involves hydrogen abstraction from a γ-carbon followed by formation of a 1,4-biradical (Figure 1-1b).[18-20] Moreover, the 1,4-biradical usually undergoes cleavage to enol and alkene products, or follows Yang cyclization adding a ring structure.[21, 22] Because of the reactive radical products, Norrish reactions have been widely studied and used not only for synthesis but also for photoinitiation and photodegradation of polymers.[23-27] In biochemistry, the radicals formed by Norrish reactions in RNA are studied to understand RNA reactivity and scission.[28-31] Moreover, carbonyl compounds are present in the atmosphere of the Earth, and Norrish reactions can be triggered by solar radiation.[32-36] Photoexcited carbonyl compounds can react with alkenes and undergo photocycloaddition (Figure 1-1c); this reaction is known as the Paternò-Büchi reaction, forming oxetanes, and has been developed for cancer treatment.[37-39] In Chapter 3, the photochemistry of cyclic ketones is studied with transient absorption spectroscopy, and since the γ-hydrogen of a cyclic ketone is not in the vicinity of the carbonyl group, the focus is on the Norrish type I reaction.

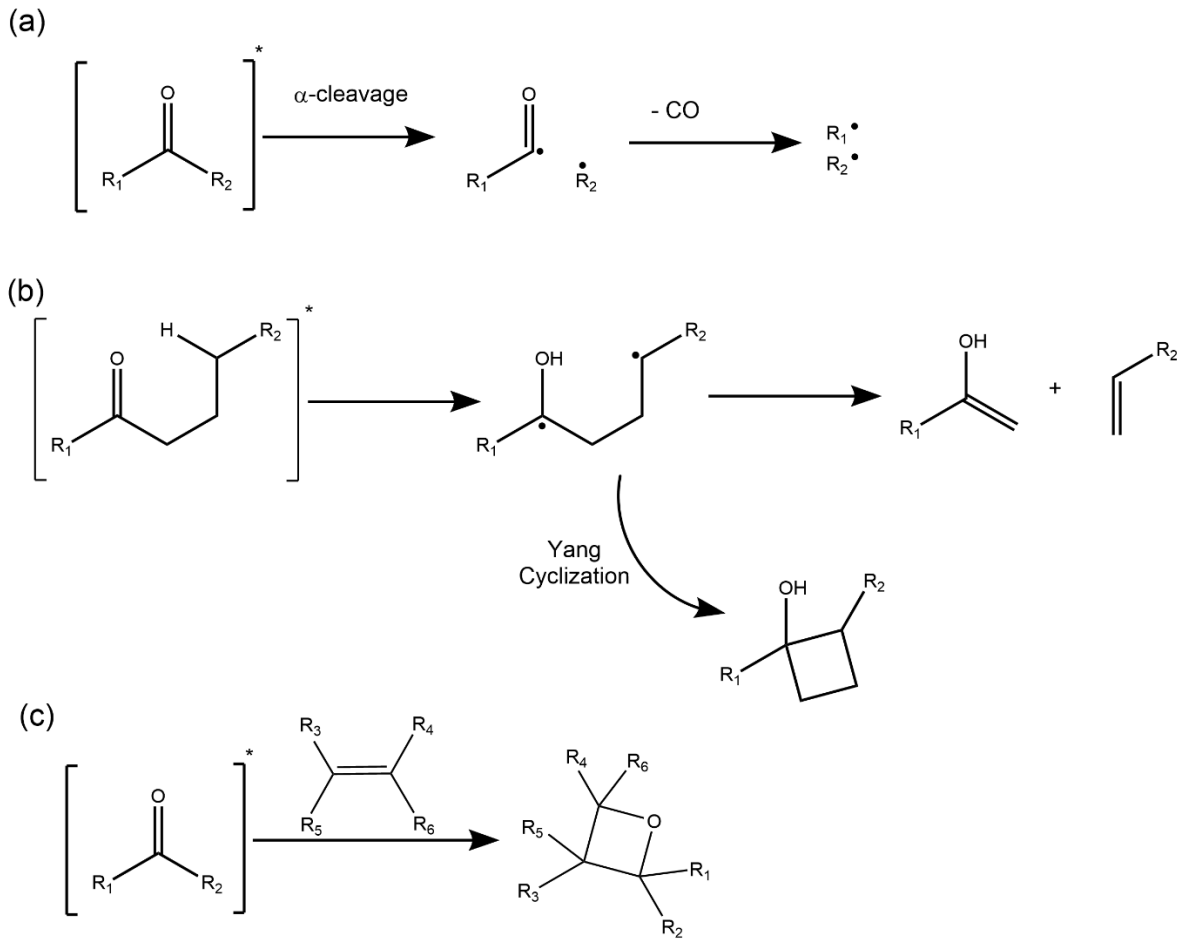

Figure 1- 1. Examples of photochemical reactions of carbonyl compounds. (a) Norrish type I reaction (b) Norrish type II reaction (c) Paternò-Büchi reaction.

1.2.1 Norrish type I reaction

The photochemistry of cyclic ketones involves two interesting aspects for photochemists: the initial Norrish type I bond-cleavage and the consequent ring opening dynamics leading to isomeric photoproducts. However, most prior studies have focused on acyclic ketones, with the photochemistry leading to two separate products that can be studied by spectroscopic or mass spectrometric methods. Norrish type I reactions were originally found to occur from the first excited triplet (T_1) state because of a smaller barrier to C-C bond cleavage than in the first excited singlet (S_1) state, but subsequent research has shown the availability of this pathway from the S_1 state using femtosecond laser methods.[15, 40, 41] The competition between two α-bonds cleaving in asymmetric ketones such as methyl isopropyl ketone were studied computationally, and the energy barrier on the S_1 state was found to be smaller for cleavage of the α-bond to the larger group.[40, 42] The energy barrier along the α-bond extension coordinate seems to decrease with larger aliphatic groups.[40] Taking methyl ethyl ketone

($CH_3COC_2H_5$) as an example, the energy barrier for the breaking methyl-propionyl (CH_3 – COC_2H_5) bond is calculated to be 70.7 kJ mol^{-1} with TDDFT, whereas the barrier for breaking the ethyl-acetyl (CH_3CO – C_2H_5) bond is 57.7 kJ mol^{-1},[40] and it is consistent with experimental results that C_2H_5 is the favored photofragment of methyl ethyl ketone.[42-44] The kinetics of photoexcited acetone in the gas phase were studied with time-resolved mass spectrometry by Zewail and coworkers, and they concluded S_1 α-cleavage occurs on a nanosecond time scale when the excitation energy is lower than the barrier on the S_1 state.[40]

For cyclic ketones, the energy barriers to α-cleavage are dependent on the ring strain.[40, 45, 46] Norrish type I reaction of cyclic ketones is used in cyclopropane-containing enediynes as a photoinitiated drug with potential use for cancer therapy.[47, 48] The ultrafast photochemistry of a series of cyclic ketones in solution, chosen for their different degrees of ring-strain, is studied and discussed in Chapter 3 of this thesis.

1.2.2 Roaming mechanism

The roaming mechanism in carbonyl photochemistry was first identified in the photodissociation of formaldehyde at excitation energies slightly above the barrier to C-H bond cleavage, and involves an unusual pathway that does not proceed over a well-defined transition state.[49] When reaction passes over the tight transition state for direct H_2 elimination, the products are rotationally excited CO and vibrationally cold H_2.[50] On the other hand, the roaming mechanism can be thought of as a frustrated loss of an H-atom: instead of dissociating to H + HCO, the hydrogen atom is not completely ejected after photoexcitation, and instead wanders around the partner HCO until it abstracts the other hydrogen atom. These unusual dynamics result in rotationally cold CO and highly vibrationally excited H_2.[49, 50] This mechanism does not go through a saddle point on the PES corresponding to a tight transition state. Subsequent experiments and dynamical simulations have revealed that this type of mechanism also arises in the photodissociation of acetaldehyde and acetone.[51, 52]

1.3 Photochemistry of sunscreen molecules

In contrast to the photochemistry of carbonyl compounds, natural and artificial sunscreen molecules such as the compound studied in Chapter 4 of this thesis dissipate the excess energy from absorption of light without bond cleavage. In this way, they avoid production of radicals which might damage living organisms. Exposure to ultraviolet (UV) radiation from

the sun can help plants and animals to synthesis pre-vitamin D by electrocyclic ring-opening reaction,[53-56] avoiding vitamin D deficiency which can encourage not only skeletal diseases but also some cancers.[57-59] However, excessive UV exposure can cause skin issues from aging to sunburn and skin cancers.[60-65] Therefore, application of a sunscreen with a proper amount of UV protection is recommended.

After UV radiation absorption by the sunscreen, there are several pathways that can happen from the excited state to dissipate the absorbed photon energy. Population from the singlet excited state can go back to the ground state via fluorescence or non-radiative electronic and vibrational relaxation. Nevertheless, some excited molecules will form photoproducts instead of returning to the ground state. Moreover, molecules in the singlet excited state can undergo intersystem crossing to triplet states, the lowest in energy of which is generally long-lived because the decay pathways for molecules to emit a photon (phosphorescence) or

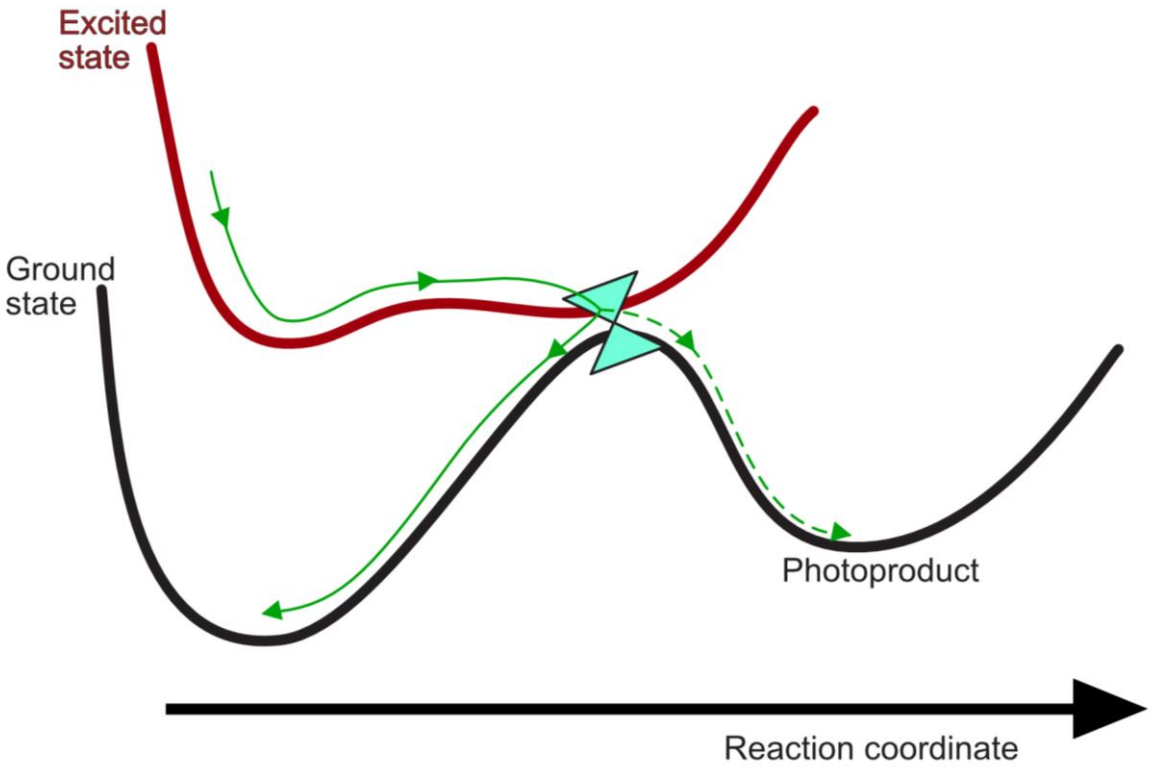

Figure 1- 2. General scheme of photoexcited sunscreen molecule relaxation via a conical intersection between an excited electronic state and the ground state. Most of the population in the excited state returns to the original structure (green solid line) via a conical intersection, with only a small part of the population forming other photoproducts after passage through the conical intersection.

intersystem cross to the ground state requires a change in electron spin multiplicity. Since the T_1 state usually has a longer lifetime than the S_1 state of a molecule, the triplet-state energy can instead transfer between molecules, especially when there are other kinds of sunscreen molecules present in a blend.[66] The resulting photosensitization is generally undesirable in sunscreen formulations because it may not safely quench the energy of the absorbed UV radiation. The mechanisms of sunscreen molecule function have been extensively studied with time resolved spectroscopy, and they often involve geometry changes along non-radiative relaxation pathways, with dynamics that are solvent dependent.[67] The rapid relaxation of a sunscreen is usually through a conical intersection between an excited state and the ground state, with most molecules returning to their ground state and only a small minority of other photoproducts formed (Figure 1-2). The following sub-sections review some of the relaxation mechanisms identified for sunscreen molecules.

1.3.1 Photoinduced cis-trans isomerization

Cinnamates:

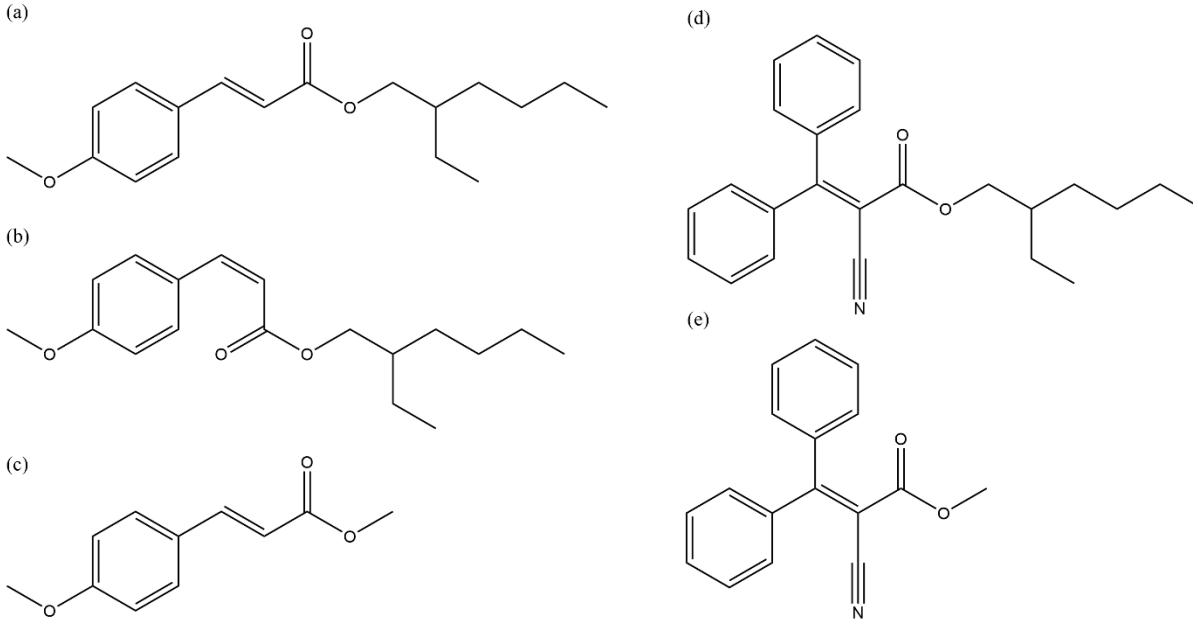

Figure 1- 3. (a) *trans*-octyl methoxycinnamate (b) *cis*-octyl methoxycinnamate (c) *trans*-p-methoxy methyl cinnamate (d) octocrylene (e) methyl 2-cyano-3,3-diphenylacrylate

Cinnamate derivatives such as octyl methoxycinnamate are commonly used as UVB absorbers.[68] Octyl methoxycinnamate can have *trans*- and *cis*- forms (Figure 1-3a and b). The *trans*-isomer is more stable than the cis-isomer in nonpolar and polar solvents, but the *cis*-isomer can be formed after UV absorption.[69-71] The calculated potential energy surfaces of a molecular sub-unit of octyl methoxycinnamate, p-methoxy methyl cinnamate (Figure 1-3c), suggest that there is a conical intersection from the S_1 state to the ground state along the cis-trans coordinate leading to the formation of the *cis*-form and the recovery of the *trans*-form.[72] In addition, the barrier between the CI and the S_1 minimum decreases when adding a water molecule coordinated to the carbonyl of p-methoxy methyl cinnamate, and the energy gap between the S_1 and S_0 states in the CI region also narrows, suggesting hydration dramatically accelerates the nonradiative relaxation from the S_1 state, consistent with experimental observations.[72, 73] With transient electronic spectroscopy, the time constant of relaxation via the CI to the ground state of octyl methoxycinnamate is found to be ~1.1 ps in methanol, and the lifetime of the *cis*-isomer is more than 2 ns.[74] Similarly, the PESs of a molecular component of octocrylene (Figure 1-2d), methyl 2-cyano-3,3-diphenylacrylate (Figure 1-3e), have been computed and suggest an ultrafast nonradiative excited state deactivation via a CI along the cis-trans coordinate on the S_1 state, observed to occur in 2 ps.[75, 76]

Camphor:

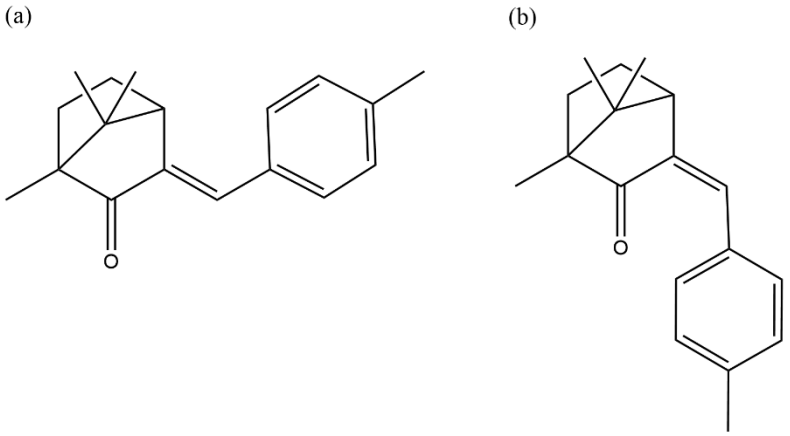

Figure 1- 4. 4-Methylbenzylidene camphor in its (a) *trans-(E)* form and (b) *cis-(Z)* form.

4-Methylbenzylidene camphor with a central carbon-carbon double bond has two isomers: *cis-(Z)* and *trans-(E)* shown in Figure 1-4. The *(E)*-isomer is more stable than the *(Z)*-isomer in the ground state, but it can convert to the (*Z*)-isomer after absorbing UVB radiation.[77, 78]

Computed PES show that there are two possible nonradiative relaxations of 4-methylbenzylidene camphor because two bright excited states (S_2 and S_3) are energetically close.[79] The first pathway is internal conversion from the photoexcited S_3 state to the S_2 state followed by another internal conversion to the S_1 state, and the second pathway is intersystem crossing from the S_3 state to the T_2 state. Eventually, both pathways lead to the T_1 state where an efficient crossing to the ground state occurs near the minimum of the T_1 state. After the crossing, some population returns to the *(E)*-isomer, and the rest of the population becomes the (*Z)*-isomer.[79] Only weak phosphorescence and a low quantum yield for singlet oxygen production are observed,[80] which is consistent with a predominantly non-radiative relaxation pathway from the T_1 to the S_0 state.[79]

1.3.2 Enol-keto tautomerization

Salicylates:

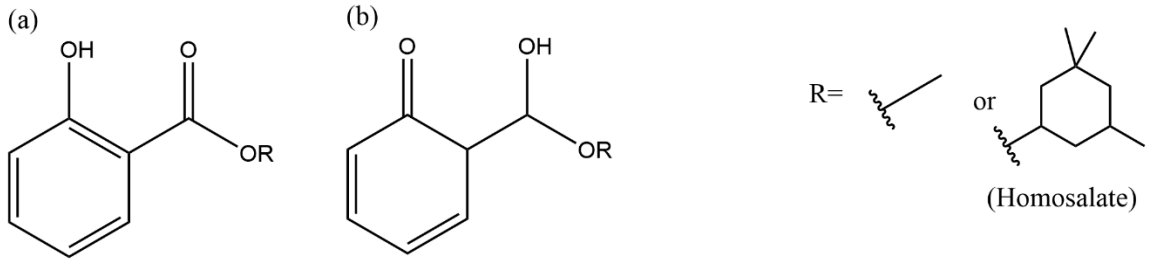

Figure 1- 5. Salicylates in the (a) enol form and (b) keto form.

Salicylate compounds (Figure 1-5) have been widely used as UV absorbers for sunscreen products since the 1950s.[68] To understand the relaxation mechanism of salicylates, the photochemistry of the subunit, methyl salicylate, has been studied, especially examining the dual fluorescence and excited state intramolecular hydrogen atom transfer from the enol form to the keto form.[81-87] The fluorescence emission spectrum of methyl salicylate shows two peaks, one centred at 350 nm and the other at 450 nm. The peak at 350 nm is weaker in non-polar solvents than in polar solvent, whereas the peak at 450 nm is weaker in polar solvents than in non-polar solvents.[88] It has been suggested that the emission at 350 nm is from the enol form which is the more stable structure in the ground state, and the emission at 450 nm is from the keto form after excited stated hydrogen transfer (ESHT). The barrier along the ESHT coordinate increases in polar solvents, hence a smaller population of the keto form emits at 450 nm.[88, 89] ESHT of methyl salicylate in the gas phase has been studied with

femtosecond laser spectroscopy and computer simulations, and the ESHT on the S_1 state can be completed within 100 fs.[87, 90, 91] Following ESHT, the S_1 keto form can relax to the S_0 state via a CI, and the hydrogen transfer from the keto to enol tautomers is a barrierless process in the ground state so completes on a picosecond time scale.[90, 92] With similar time constants observed by transient electronic absorption spectroscopy, the relaxation mechanism of homosalate in solution is proposed to be through an ESHT pathway analogous to that in methyl salicylate.[93]

Benzophenones:

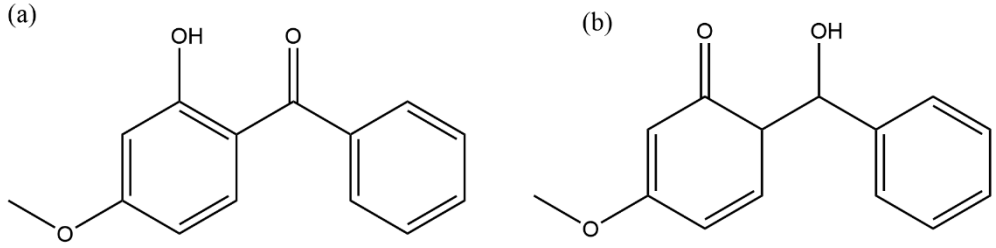

Figure 1- 6. Oxybenzone in its (a) enol form and (b) keto form

Oxybenzone (Figure 1-6) is a derivative of benzophenone, and ultrafast spectroscopy measurements combined with computational studies have helped to propose a complete mechanism of relaxation via enol- keto tautomerization.[94-97] Oxybenzone exists either in the enol form or the keto form, and the enol is the more stable structure in the ground state. After excitation at 325 nm populating the S_2 state, the oxybenzone undergoes excited state hydrogen transfer (ESHT) to the S_1 keto within ~100 fs.[94, 95, 97] Following ESHT, a central C−C bond twisting happens to the S_1 keto with a time constant of around 400 fs, making a CI between the S_1 and S_0 states accessible.[96, 97] Once the molecule has returned to the ground electronic state, the keto form undergoes hydrogen transfer to recover the enol form and vibrationally relaxes in 5-8 ps, with a precise timescale that is dependent on the polarity of the solvent.[94, 95] A small portion of a trans-keto isomer forms on the ground state PES as a photoproduct because of extended C−C bond twisting, and the lifetime of the trans-keto is longer than 1 ns.[95] These dynamics are contrasted with those found for diethylamino hydroxybenzoyl hexyl benzoate (DHHB), another benzophenone based sunscreen, in Chapter 4.

1.3.3 Solvent dependence

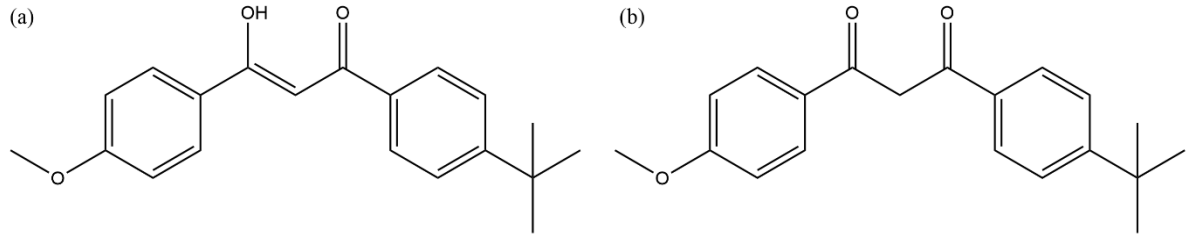

Figure 1- 7. Avobenzone in its (a) enol form and (b) keto form

The interactions between solvent molecules and sunscreen molecules can alter the photochemistry of the sunscreen chromophores. For example, the relaxation of cinnamates is drastically faster in solution than in the gas phase because solvent molecules can dissipate excess vibrational energy from the solute.[72, 73, 98] The dual fluorescence of methyl salicylate also shows solvent dependence, as described in Section 1.3.2. Transient electronic absorption spectra of avobenzone (Figure 1-7) in cyclohexane, acetonitrile and methanol show that not only the relaxation time constants vary, but also that the quantum yields of intermediates are different.[99] After vertical photoexcitation to the S_1 state, avobenzone can relax through a chelated enol and three structurally distinct non-chelated enols, and the proportions depend on the choice of solvent.[67, 100] The relaxation of the chelated enol form of avobenzone has a time constant of ~6 ps, and the relaxations through non-chelated enols have various time constants ranging from 1 ps to microseconds. Although there has been no direct observation of the keto form of avobenzone, the small unrecovered ground state population of avobenzone after photoexcitation suggests the partial formation of the keto tautomer.[99, 101] However, a recent study of protonated avobenzone with mass spectrometry shows prominent photoinduced enol - keto tautomerization, which suggests the protonation disrupts the stability of the enol form.[102]

1.4 Searching for phenyl cation

Another class of organic compounds showing potentially rich photochemical dynamics in solution after UV absorption is the aryl halides. The photochemistry of selected chlorobenzenes is studied in Chapter 5 of this thesis, with the objective of identifying both homolytic and heterolytic bond cleavage pathways. An aryl cation contains a positively charged aromatic ring, corresponding to one of the most reactive forms of intermediate used in organic synthesis, and the phenyl cation sought here contains a positively charged benzene

ring.[103] Aryl cations can be produced by thermal decomposition of an aryl diazonium compound, and they can undergo intramolecular cyclization or intramolecular hydride transfer followed by hydrolysis.[104-109] Moreover, the intramolecular cyclization can bind adjacent oxygen and sulfur to form alkyldibenzofuranium and alkyldibenzothiophenium species.[110] The current interest in the phenyl cation comes from its ability to capture molecular nitrogen to afford diazonium compounds, as observed by mass spectrometry.[111, 112] The phenyl cation can bind with N_2 in pressures of 505 Pa of nitrogen, with the N_2 capture finished within 30 milliseconds of trapping time.[112] This reaction has the potential to provide an alternative to the energy consuming Haber-Bosch process to extract nitrogen from the atmosphere for chemical feedstocks.[113] The product diazonium compound can be used for synthesis of azobenzene, which has been targeted for use in liquid crystals, photochemical molecular switches, and antibiotics.[114-116] In the solution phase, the photodissociation of aryl halides to aryl cations has been studied previously, with a general hypothesis that aryl cations are generated following electron transfer between radical pairs made by bond homolysis.[103, 117, 118] However, this mechanism has not been investigated or verified using ultrafast laser spectroscopy, and alternative pathways involving ion-pair states of the parent molecule may instead be responsible for the heterolytic bond dissociation.

1.4.1 Singlet and triplet phenyl cations

The phenyl cation has singlet and triplet spin-state forms. The singlet phenyl cation is closed shell ($\pi^6\sigma^0$) and is more stable than the open-shell triplet phenyl cation ($\pi^5\sigma^1$) by ~100 kJ mol^{-1} when there is no substituent group attached.[119, 120] The most obvious difference in the geometries of the two forms is the bond angle about the carbocation centre (i.e. the C atom formally carrying the positive charge). This ring bond angle in the singlet phenyl cation is about 147˚ whereas in the triplet phenyl cation it is about 125˚ which is closer to the angle found in a phenyl radical, suggesting the triplet state may be an intermediate formed before the singlet phenyl cation.[119, 121] Nevertheless, the triplet aryl cation is usually more stable than the singlet when an electron-donating group is attached on *para-* or *ortho-* sites of the phenyl ring.[122, 123] Moreover, because of the difference in electronic configurations, the chemoselectivities of the two forms of the phenyl cations are not the same. The singlet phenyl cation is a strong electrophile, whereas the triplet phenyl cation selectively reacts with π-nucleophiles like alkynes and aromatic compounds.[103, 124-126] Nitrogen fixation by a main

group element, boron, is based on σ donation from N_2 to an empty σ orbital of boron and π backdonation to the empty π^* orbital of N_2,[127] and a similar mechanism is proposed for nitrogen capture by the singlet phenyl cation.[128]

1.5 Transient absorption spectroscopy

The experimental technique used in the work presented in this thesis to study the ultrafast photochemical dynamics of organic compounds in solution is transient absorption spectroscopy. In general terms, TAS involves two beams of light passing through a sample with different timings, a rotating chopper, and a moving mirror, as shown in Figure 1-8. One of the beams of light is the pump laser beam, with pump pulses used to promote the target molecules to an excited electronic state. The other is the probe laser beam, with either a white-light continuum or mid-IR pulses intended to acquire information about either the populated electronic or vibrational energy levels of the molecules. The rotating chopper wheel alternately blocks and allows the pump beam to irradiate the sample, which means the pump light is switched on and off. Hence, the probe beam will transmit spectral information about both the excited sample, with the pump on, and the original sample, with the pump off, and the difference between the absorption spectra acquired for pump-on and pump-off configurations contains discernible contributions from photochemical intermediates such as excited state absorption, stimulated emission, and ground state depletion (bleaching). With

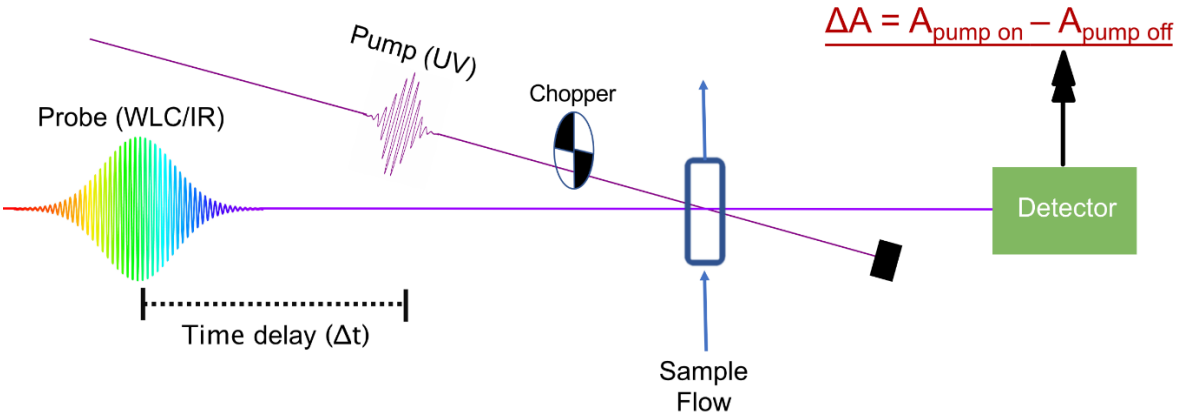

Figure 1- 8. Illustration of the layout for a transient absorption spectroscopy measurement. UV pump laser pulses are switched on and off by a chopper, and excite the sample; after a time delay in the sub-picosecond to nanosecond range, a broadband white light continuum (WLC) or mid-IR pulse probes the sample. The detector records the transmitted light intensity (and hence the amount of absorption) with the pump alternately on and off, and the difference in absorption caused by the UV pump pulses is deduced.

a moving mirror controlling the delay time between the pump and probe pulses, the kinetics and dynamics of photochemical reactions can be investigated on the sub-picosecond to nanosecond timescale.

After the excited state is populated by absorption of photons from the UV pump pulse, the population in the excited state can further absorb light from the probe pulse and be excited to a higher electronic state (Figure 1-9a), which results in the excited state absorption (ESA) illustrated in Figure 1-9b. In the transient absorption spectra shown in this thesis, processed as the change in absorbance $\Delta A = A_{pump\ on} - A_{pump\ off}$, ESA appears as a positive signal because there are no excited-state molecules to absorb the probe pulse photons without prior irradiation of the sample by the pump beam. However, the population in the excited state can also undergo stimulated emission when probe wavelengths match the wavelengths of emission back to the ground state (Figure 1-9c). Simulated emission appears as a negative signal because photons are emitted with the same frequency as some of the incident photons and more light is incident on the detector. Finally, the ground state bleach features result

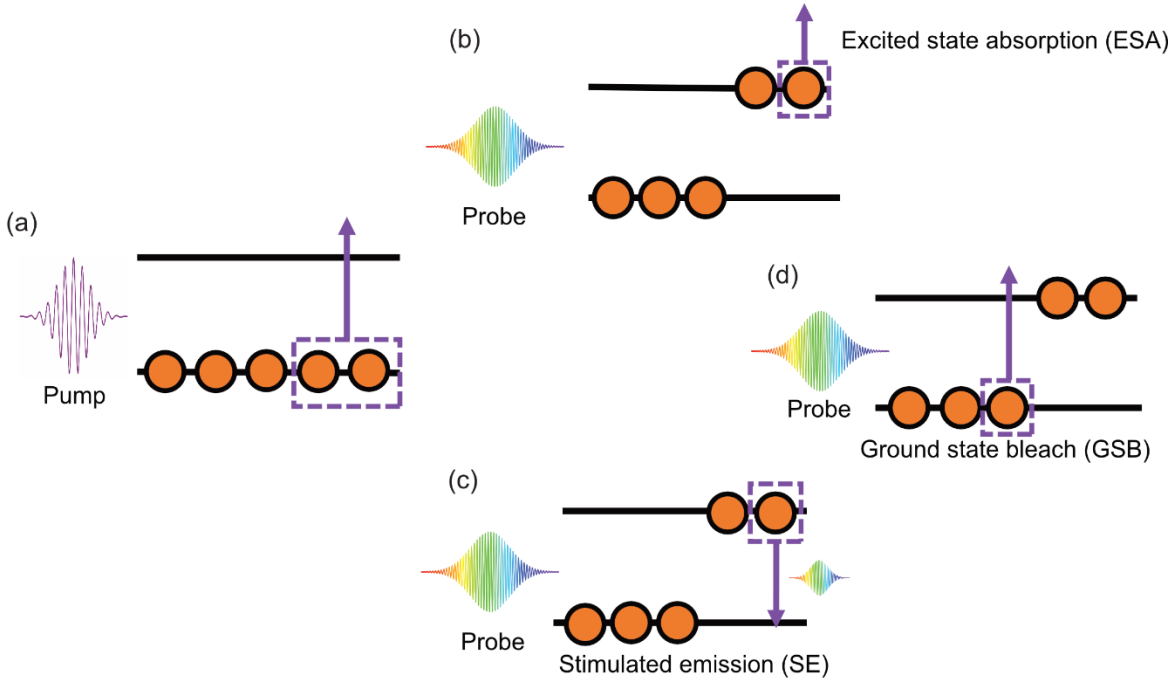

Figure 1- 9. Mechanisms for features contributing to transient absorption spectra. (a) The pump pulse excites some population from the ground state to an excited state. (b) The probe pulse is absorbed by the population in the excited state, giving excited state absorption (ESA). (c) The probe pulse causes stimulated emission (SE) from the excited state. (d) The probe pulse is absorbed by the remaining population in the ground state, which has been depleted by the pump pulse, giving a ground-state bleach feature.

from absorption of the probe light by the depleted population remaining in the ground state after pump-pulse excitation (Figure 1-9d). Since the population in the ground state is reduced by the pump pulse, the difference in absorption appears as a negative feature in transient absorption spectra. TAS methods have been used to study a broad range of photochemical systems, for example, electron transfer between organic compounds in solutions,[129, 130] radical cations formed by electron transfer from organic photocatalysts,[131] reactive carbenes produced by photoexcitation of α-diazocarbonyl compounds,[132] photo-induced proton transfer in DNA nucleobase pairs providing effective nonradiative relaxation and enhancing the photostability,[133, 134] relaxation pathways of photoexcited AT DNA oligonucleotides,[135] photochemistry of π–π stacking of the adenine,[136] and the solvent-dependence of the photochemistry of various photocatalysts and organic chromophores.[137, 138] TAS methods can also be used for solid samples, for instance, lead halide perovskites.[139, 140] The time delays used in TAS can be in the sub-picosecond to nanosecond range using optical delay lines, and can extend to microseconds using electronic delays.[141, 142]

The details of the laser system used for TAS are described in Chapter 2, and are followed by chapters reporting the main research results presented in this thesis. The photoinduced α-cleavages of three cyclic ketones are studied using different pump-laser wavelengths, and the effects of ring strain on the ring opening dynamics are reported in Chapter 3. In Chapter 4, a sunscreen molecule DHHB, which is structurally similar to oxybenzone, is shown to relax via competing excited state hydrogen transfer or internal conversion pathways. The competition between the two relaxation pathways is observed in different solvents, and the excited state hydrogen transfer is shown to be less favourable in polar solvents. These two projects examining the photochemistry of cyclic ketones and the DHHB sunscreen have been published,[143, 144] and the two chapters are adapted from the published journal articles. Finally, Chapter 5 presents a report of an ongoing project exploring the possibility of phenyl cation generation from the photodissociation of chlorobenzene. In this chapter, results for the photochemistry of chlorobenzene at different excitation wavelengths and in different solvents is reported.

References

1. J. Van Houten, *J. Chem. Educ.*, 2002, **79**, 548.
2. E. D. Potter, J. L. Herek, S. Pedersen, Q. Liu and A. H. Zewail, *Nature*, 1992, **355**, 66-68.
3. The Nobel Prize Organisation, The Nobel Prize in Chemistry 1999, https://www.nobelprize.org/prizes/chemistry/1999/summary/, (accessed 24 June, 2021).
4. N. F. Scherer, D. M. Jonas and G. R. Fleming, *J. Phys. Chem.*, 1993, **99**, 153-168.
5. O. F. Mohammed, *Science*, 2005, **310**, 83-86.
6. J. Zheng, *Science*, 2005, **309**, 1338-1343.
7. F. Ráksi, K. R. Wilson, Z. Jiang, A. Ikhlef, C. Y. Côté and J. C. Kieffer, *J. Chem. Phys.*, 1996, **104**, 6066-6069.
8. D. Polli, P. Altoè, O. Weingart, K. M. Spillane, C. Manzoni, D. Brida, G. Tomasello, G. Orlandi, P. Kukura, R. A. Mathies, M. Garavelli and G. Cerullo, *Nature*, 2010, **467**, 440-443.
9. T. Nägele, R. Hoche, W. Zinth and J. Wachtveitl, *Chem. Phys. Lett.*, 1997, **272**, 489-495.
10. X. Hong, J. Kim, S.-F. Shi, Y. Zhang, C. Jin, Y. Sun, S. Tongay, J. Wu, Y. Zhang and F. Wang, *Nat. Nanotechnol.*, 2014, **9**, 682-686.
11. A. Morandeira, A. Fürstenberg, O. Nicolet, S. Pages, B. Lang and E. Vauthey, *CHIMIA Int. J. Chem.*, 2002, **56**, 690-694.
12. M. Born and R. Oppenheimer, *Ann. Physik*, 1927, **389**, 457-484.
13. G. A. Worth and L. S. Cederbaum, *Annu. Rev. Phys. Chem.*, 2004, **55**, 127-158.
14. R. G. W. Norrish and M. E. S. Appleyard, *J. Chem. Soc.*, 1934, 874-880.
15. R. G. W. Norrish and C. H. Bamford, *Nature*, 1936, **138**, 1016-1016.
16. P. Liu, W. B. Liu and C. J. Li, *J. Am. Chem. Soc.*, 2017, **139**, 14315-14321.
17. O. Muraoka, M. Okumura, T. Maeda, L. C. Wang and G. Tanabe, *Chem. Pharm. Bull.*, 1995, **43**, 517-519.
18. A. Lauer, D. E. Fast, A.-M. Kelterer, E. Frick, D. Neshchadin, D. Voll, G. Gescheidt and C. Barner-Kowollik, *Macromolecules*, 2015, **48**, 8451-8460.
19. M. Shirai and H. Okamura, *Polym. Int.*, 2016, **65**, 362-370.
20. J. A. Dantas, J. T. M. Correia, M. W. Paixão and A. G. Corrêa, *ChemPhotoChem*, 2019, **3**, 506-520.
21. C. Chen, *Org. Biomol. Chem.*, 2016, **14**, 8641-8647.
22. N. C. Yang and D.-D. H. Yang, *J. Am. Chem. Soc.*, 1958, **80**, 2913-2914.
23. K. Arangdad, A. Detwiler, C. D. Cleven, C. Burk, R. Shamey, M. A. Pasquinelli, H. Freeman and A. El-Shafei, *J. Appl. Polym. Sci.*, 2019, **136**, 47148.
24. S. Arumugam, D. R. Vutukuri, S. Thayumanavan and V. Ramamurthy, *J. Am. Chem. Soc.*, 2005, **127**, 13200-13206.
25. R. W. Guo, P. B. Mei, Q. Zhong, Y. Yao, Q. Su and J. H. Zhang, *RSC Adv.*, 2015, **5**, 31365-31374.
26. J. Jakubiak, M. Nowakowska and X. Coqueret, *Bull. Pol. Acad. Sci.*, 1997, **45**, 71-77.
27. A. U. Shete, B. P. Sutherland and C. J. Kloxin, *Polym. Chem.*, 2020, **11**, 7515-7523.
28. C. A. Newman, M. J. E. Resendiz, J. T. Sczepanski and M. M. Greenberg, *J. Org. Chem.*, 2009, **74**, 7007-7012.
29. M. J. E. Resendiz, V. Pottiboyina, M. D. Sevilla and M. M. Greenberg, *J. Am. Chem. Soc.*, 2012, **134**, 3917-3924.
30. A. C. Jacobs, M. J. E. Resendiz and M. M. Greenberg, *J. Am. Chem. Soc.*, 2011, **133**, 5152-5159.

31. M. Okada, K. Yamada, T. Fukuyama, D. Ravelli, M. Fagnoni and I. Ryu, *J. Org. Chem.*, 2015, **80**, 9365-9369.
32. J. E. Scott, *Analyst*, 1977, **102**, 614-618.
33. H. K. Wang, C. H. Huang, K. S. Chen, Y. P. Peng and C. H. Lai, *J. Hazard. Mater.*, 2010, **179**, 1115-1121.
34. H.-K. Wang, C.-H. Huang, K.-S. Chen and Y.-P. Peng, *Aerosol Air Qual. Res.*, 2010, **10**, 559-570.
35. A. Chattopadhyay, K. Mondal, M. Samanta and T. Chakraborty, *Atmos. Environ.*, 2017, **157**, 125-134.
36. D. J. Jacob, B. D. Field, E. M. Jin, I. Bey, Q. Li, J. A. Logan, R. M. Yantosca and H. B. Singh, *J. Geophys. Res. Atmos.*, 2002, **107**, ACH 5-1.
37. M. Fréneau and N. Hoffmann, *J. Photochem. Photobiol. C*, 2017, **33**, 83-108.
38. G. Büchi, C. G. Inman and E. S. Lipinsky, *J. Am. Chem. Soc.*, 1954, **76**, 4327-4331.
39. H. Lechner, D. Pressnitz and W. Kroutil, *Biotechnol. Adv.*, 2015, **33**, 457-480.
40. E. W. G. Diau, C. Kotting and A. H. Zewail, *Chemphyschem*, 2001, **2**, 273-293.
41. S. Maeda, K. Ohno and K. Morokuma, *J. Phys. Chem. Lett.*, 2010, **1**, 1841-1845.
42. R. Nádasdi, G. L. Zügner, M. Farkas, S. Dóbé, S. Maeda and K. Morokuma, *Chemphyschem*, 2010, **11**, 3883-3895.
43. M. T. B. Romero, M. A. Blitz, D. E. Heard, M. J. Pilling, B. Price and P. W. Seakins, *Chem. Phys. Lett.*, 2005, **408**, 232-236.
44. V. Khamaganov, R. Karunanandan, A. Rodriguez and J. N. Crowley, *Phys. Chem. Chem. Phys.*, 2007, **9**, 4098.
45. E. W. G. Diau, C. Kotting and A. H. Zewail, *Chemphyschem*, 2001, **2**, 294-309.
46. S. H. Xia, X. Y. Liu, Q. Fang and G. L. Cui, *J. Phys. Chem. A*, 2015, **119**, 3569-3576.
47. S. J. Léger, B. Marchetti, M. N. R. Ashfold and T. N. V. Karsili, *Front. Chem.*, 2020, **8**.
48. D. R. Pandithavidana, A. Poloukhtine and V. V. Popik, *J. Am. Chem. Soc.*, 2009, **131**, 351-356.
49. D. Townsend, S. A. Lahankar, S. K. Lee, S. D. Chambreau, A. G. Suits, X. Zhang, J. Rheinecker, L. B. Harding and J. M. Bowman, *Science*, 2004, **306**, 1158-1161.
50. A. G. Suits, *Acc. Chem. Res.*, 2008, **41**, 873-881.
51. V. Goncharov, N. Herath and A. G. Suits, *J. Phys. Chem. A*, 2008, **112**, 9423-9428.
52. L. Rubio-Lago, G. A. Amaral, A. Arregui, J. G. Izquierdo, F. Wang, D. Zaouris, T. N. Kitsopoulos and L. Bañares, *Phys. Chem. Chem. Phys.*, 2007, **9**, 6123.
53. M. F. Holick, T. C. Chen, Z. Lu and E. Sauter, *J. Bone Miner. Res.*, 2007, **22**, V28-V33.
54. R. B. Jäpelt and J. Jakobsen, *Front. Plant Sci.*, 2013, **4**, Article 136.
55. T. J. A. Wolf, D. M. Sanchez, J. Yang, R. M. Parrish, J. P. F. Nunes, M. Centurion, R. Coffee, J. P. Cryan, M. Gühr, K. Hegazy, A. Kirrander, R. K. Li, J. Ruddock, X. Shen, T. Vecchione, S. P. Weathersby, P. M. Weber, K. Wilkin, H. Yong, Q. Zheng, X. J. Wang, M. P. Minitti and T. J. Martínez, *Nat. Chem.*, 2019, **11**, 504-509.
56. S. Deb and P. M. Weber, in *Annu. Rev. Phys. Chem.*, eds. S. R. Leone, P. S. Cremer, J. T. Groves and M. A. Johnson, Annual Reviews, Palo Alto, 2011, vol. 62, pp. 19-39.
57. R. M. Lucas and A. L. Ponsonby, *Med. J. Aust.*, 2002, **177**, 594-598.
58. M. F. Holick, *N. Engl. J. Med.*, 2007, **357**, 266-281.
59. M. F. Holick, *Am. J. Clin. Nutr.*, 2004, **80**, 1678S-1688S.
60. A. Sample, B. Z. Zhao, L. Qiang and Y. Y. He, *J. Biol. Chem.*, 2017, **292**, 14786-14795.
61. G. T. Wondrak, M. J. Roberts, D. Cervantes-Laurean, M. K. Jacobson and E. L. Jacobson, *J. Investig. Dermatol.*, 2003, **121**, 578-586.

62. N. R. Attard and P. Karran, *Photochem. Photobiol. Sci.*, 2012, **11**, 62-68.
63. E. Sage, P. M. Girard and S. Francesconi, *Photochem. Photobiol. Sci.*, 2012, **11**, 74-80.
64. J. A. Curtin, J. Fridlyand, T. Kageshita, H. N. Patel, K. J. Busam, H. Kutzner, K.-H. Cho, S. Aiba, E.-B. Bröcker, P. E. Leboit, D. Pinkel and B. C. Bastian, *N. Engl. J. Med.*, 2005, **353**, 2135-2147.
65. S. Madronich, R. L. Mckenzie, L. O. Björn and M. M. Caldwell, *j. Photochem. Photobiol. B*, 1998, **46**, 5-19.
66. S. Matsumoto, R. Kumasaka, M. Yagi and A. Kikuchi, *J. Photochem. Photobiol. A*, 2017, **346**, 396-400.
67. L. A. Baker, S. E. Greenough and V. G. Stavros, *J. Phys. Chem. Lett.*, 2016, **7**, 4655-4665.
68. N. A. Shaath, *Photochem. Photobiol. Sci.*, 2010, **9**, 464-469.
69. S. Pattanaargson, T. Munhapol, P. Hirunsupachot and P. Luangthongaram, *J. Photochem. Photobiol. A*, 2004, **161**, 269-274.
70. K. M. Hanson, S. Narayanan, V. M. Nichols and C. J. Bardeen, *Photochem. Photobiol. Sci.*, 2015, **14**, 1607-1616.
71. S. Pattanaargson and P. Limphong, *Int. J. Cosmet. Sci.*, 2001, **23**, 153-160.
72. X.-P. Chang, C.-X. Li, B.-B. Xie and G. Cui, *J. Phys. Chem. A*, 2015, **119**, 11488-11497.
73. E. M. M. Tan, M. Hilbers and W. J. Buma, *J. Phys. Chem. Lett.*, 2014, **5**, 2464-2468.
74. Y. Peperstraete, M. Staniforth, L. A. Baker, N. D. N. Rodrigues, N. C. Cole-Filipiak, W.-D. Quan and V. G. Stavros, *Phys. Chem. Chem. Phys.*, 2016, **18**, 28140-28149.
75. L. A. Baker, M. D. Horbury and V. G. Stavros, *Opt. Express*, 2016, **24**, 10.
76. X.-P. Chang, Y.-G. Fang and G. Cui, *J. Phys. Chem. A*, 2019, **123**, 8823-8831.
77. H.-R. Buser, M. D. Müller, M. E. Balmer, T. Poiger and I. J. Buerge, *Environ. Sci. Technol.*, 2005, **39**, 3013-3019.
78. H. Moneyron, R. Arnaud, J. Lemaire, A. Deflandre and M. Goetz, *J. Photochem. Photobiol. A*, 1993, **75**, 77-82.
79. Y.-G. Fang, C.-X. Li, X.-P. Chang and G. Cui, *Chemphyschem*, 2018, **19**, 744-752.
80. A. Kikuchi, K. Shibata, R. Kumasaka and M. Yagi, *J. Phys. Chem. A*, 2013, **117**, 1413-1419.
81. W. Klöpffer and G. Kaufmann, *J. Lumin.*, 1979, **20**, 283-289.
82. R. Lopez-Delgado and S. Lazare, *J. Phys. Chem.*, 1981, **85**, 763-768.
83. A. Mitsuzuka, A. Fujii, T. Ebata and N. Mikami, *J. Phys. Chem. A*, 1998, **102**, 9779-9784.
84. F. Toribio, J. Catalan, F. Amat and A. U. Acuna, *J. Phys. Chem.*, 1983, **87**, 817-822.
85. J. Catalán, *Phys. Chem. Chem. Phys.*, 2012, **14**, 8903.
86. K.-Y. Law and J. Shoham, *J. Phys. Chem.*, 1994, **98**, 3114-3120.
87. A. Watwiangkham, T. Roongcharoen and N. Kungwan, *J. Photochem. Photobiol. A*, 2020, **389**, 112267.
88. P. Zhou, M. R. Hoffmann, K. Han and G. He, *J. Phys. Chem. B*, 2015, **119**, 2125-2131.
89. S. Ghosh, J. Thomas, W. Huang, Y. Xu and W. Jäger, *J. Phys. Chem. Lett.*, 2015, **6**, 3126-3131.
90. F. Ling, D. Liu, S. Li, W. Li, B. Zhang and P. Wang, *J. Chem .Phys.*, 2019, **151**, 094302.
91. J. L. Herek, S. Pedersen, L. Banares and A. H. Zewail, *J. Chem. Phys.*, 1992, **97**, 9046-9061.
92. X. P. Chang, T. S. Zhang, Y. G. Fang and G. L. Cui, *J. Phys. Chem. A*, 2021, **125**, 1880-1891.
93. E. L. Holt, K. M. Krokidi, M. A. P. Turner, P. Mishra, T. S. Zwier, N. D. N. Rodrigues and V. G. Stavros, *Phys. Chem. Chem. Phys.*, 2020, **22**, 15509-15519.

94. L. A. Baker, M. D. Horbury, S. E. Greenough, M. N. R. Ashfold and V. G. Stavros, *Photochem. Photobiol. Sci.*, 2015, **14**, 1814-1820.
95. L. A. Baker, M. D. Horbury, S. E. Greenough, P. M. Coulter, T. N. Karsili, G. M. Roberts, A. J. Orr-Ewing, M. N. Ashfold and V. G. Stavros, *J. Phys. Chem. Lett.*, 2015, **6**, 1363-1368.
96. T. N. V. Karsili, B. Marchetti, M. N. R. Ashfold and W. Domcke, *J. Phys. Chem. A*, 2014, **118**, 11999-12010.
97. C. X. Li, W. W. Guo, B. B. Xie and G. Cui, *J. Chem. Phys.*, 2016, **145**, 074308.
98. A. Rosspeintner, B. Lang and E. Vauthey, *Annu. Rev. Phys. Chem.*, 2013, **64**, 247-271.
99. A. D. Dunkelberger, R. D. Kieda, B. M. Marsh and F. F. Crim, *J. Phys. Chem. A*, 2015, **119**, 6155-6161.
100. M. Kojić, M. Petković and M. Etinski, *Phys. Chem. Chem. Phys.*, 2016, **18**, 22168-22178.
101. M. Yamaji and M. Kida, *J. Phys. Chem. A*, 2013, **117**, 1946-1951.
102. J. A. Berenbeim, N. G. K. Wong, M. C. R. Cockett, G. Berden, J. Oomens, A. M. Rijs and C. E. H. Dessent, *J. Phys. Chem. A*, 2020, **124**, 2919-2930.
103. V. Dichiarante, S. Protti and M. Fagnoni, *J. Photochem. Photobiol. A*, 2017, **339**, 103-113.
104. T. Cohen, A. H. Dinwoodie and L. D. Mckeever, *J. Org. Chem.*, 1962, **27**, 3385-3390.
105. T. Cohen and J. Lipowitz, *J. Am. Chem. Soc.*, 1964, **86**, 2514-2515.
106. T. Cohen and J. Lipowitz, *J. Am. Chem. Soc.*, 1964, **86**, 2515-2516.
107. P. Martinson, C. A. Wachtmeister, B. Larsen, A. Haug and J. Paasivirta, *Acta Chem. Scand.*, 1968, **22**, 1357-1358.
108. R. Sikkar, P. Martinson, S.-O. Lawesson, H. Fritz and C. R. Enzell, *Acta Chem. Scand.*, 1980, **34b**, 551-557.
109. X. Li, L. Sun, Q. Zhang, S. Li, Y. Wang, D. Wei, W. Zhang and Y. Lan, *ChemCatChem*, 2019, **11**, 5068-5076.
110. I. M. Downie, H. Heaney(Rk), G. Kemp, D. King and M. Wosley, *Tetrahedron*, 1992, **48**, 4005-4016.
111. X. Xu, J. Dai, X. Guo, C. Qian, P. Zhang, Y. Duan and Y. Tian, *Phys. Chem. Chem. Phys.*, 2021, **23**, 10763-10767.
112. A. Y. Li, F. P. M. Jjunju and R. G. Cooks, *J. Am. Soc. Mass Spectrom.*, 2013, **24**, 1745-1754.
113. L. F. Razon, *Environ. Prog. Sustain. Energy*, 2014, **33**, 618-624.
114. E. Merino, *Chem. Soc. Rev.*, 2011, **40**, 3835.
115. S. Piotto, S. Concilio, L. Sessa, A. Porta, E. C. Calabrese, A. Zanfardino, M. Varcamonti and P. Iannelli, *Eur. J. Med. Chem.*, 2013, **68**, 178-184.
116. M. R. Lutfor, G. Hegde, S. Kumar, C. Tschierske and V. G. Chigrinov, *Opt. Mater.*, 2009, **32**, 176-183.
117. K. Hori, T. Sonoda, M. Harada and S. Yamazaki-Nishida, *Tetrahedron*, 2000, **56**, 1429-1436.
118. M. Winkler and W. Sander, *Angew. Chem.-Int. Edit.*, 2000, **39**, 2014-2016.
119. J. Hrušák, D. Schröder and S. Iwata, *J. Chem .Phys.*, 1997, **106**, 7541-7549.
120. A. Nicolaides, D. M. Smith, F. Jensen and L. Radom, *J. Am. Chem. Soc.*, 1997, **119**, 8083-8088.
121. J. N. Harvey, M. Aschi, H. Schwarz and W. Koch, *Theor. Chem. Acc.*, 1998, **99**, 95-99.
122. S. Lazzaroni, D. Dondi, M. Fagnoni and A. Albini, *J. Org. Chem.*, 2008, **73**, 206-211.
123. S. Protti, V. Dichiarante, D. Dondi, M. Fagnoni and A. Albini, *Chem. Sci.*, 2012, **3**, 1330.

124. M. Mella, P. Coppo, B. Guizzardi, M. Fagnoni, M. Freccero and A. Albini, *J. Org. Chem.*, 2001, **66**, 6344-6352.
125. S. Milanesi, M. Fagnoni and A. Albini, *Chem. Commun.*, 2003, 216-217.
126. M. Slegt, H. S. Overkleeft and G. Lodder, *Eur. J. Org. Chem.*, 2007, **2007**, 5364-5375.
127. M.-A. Légaré, G. Bélanger-Chabot, R. D. Dewhurst, E. Welz, I. Krummenacher, B. Engels and H. Braunschweig, *Science*, 2018, **359**, 896-900.
128. M. Winkler and W. Sander, *J. Org. Chem.*, 2006, **71**, 6357-6367.
129. C. A. Rumble and E. Vauthey, *Phys. Chem. Chem. Phys.*, 2019, **21**, 11797-11809.
130. H. N. Ghosh, S. Verma and E. T. J. Nibbering, *j. Phys. Chem. A*, 2011, **115**, 664-670.
131. D. Koyama, H. J. A. Dale and A. J. Orr-Ewing, *J. Am. Chem. Soc.*, 2018, **140**, 1285-1293.
132. R. Phelps and A. J. Orr-Ewing, *J. Am. Chem. Soc.*, 2020, **142**, 7836-7844.
133. K. Röttger, H. J. B. Marroux, A. F. M. Chemin, E. Elsdon, T. A. A. Oliver, S. T. G. Street, A. S. Henderson, M. C. Galan, A. J. Orr-Ewing and G. M. Roberts, *J. Phys. Chem. B*, 2017, **121**, 4448-4455.
134. H. Böhnke, K. Röttger, R. A. Ingle, H. J. B. Marroux, M. Bohnsack, N. K. Schwalb, A. J. Orr-Ewing and F. Temps, *J. Phys. Chem. B*, 2019, **123**, 2904-2914.
135. D. J. Skowron, Y. Zhang, A. A. Beckstead, J. M. Remington, M. Strawn and B. Kohler, *Chemphyschem*, 2016, **17**, 3558-3569.
136. J. Chen and B. Kohler, *J. Am. Chem. Soc.*, 2014, **136**, 6362-6372.
137. R. K. Venkatraman and A. J. Orr-Ewing, *J. Am. Chem. Soc.*, 2019, **141**, 15222-15229.
138. M. Sneha, L. Lewis-Borrell, D. Shchepanovska, A. Bhattacherjee, J. Tyler and A. J. Orr-Ewing, *Z. Phys. Chem.*, 2020, **234**, 1475-1494.
139. T. J. Jacobsson, J.-P. Correa-Baena, E. Halvani Anaraki, B. Philippe, S. D. Stranks, M. E. F. Bouduban, W. Tress, K. Schenk, J. Teuscher, J.-E. Moser, H. Rensmo and A. Hagfeldt, *J. Am. Chem. Soc.*, 2016, **138**, 10331-10343.
140. C. T. Weisspfennig, D. J. Hollman, C. Menelaou, S. D. Stranks, H. J. Joyce, M. B. Johnston, H. J. Snaith and L. M. Herz, *Adv. Funct. Mater.*, 2014, **24**, 668-677.
141. J. M. Woolley, R. Losantos, D. Sampedro and V. G. Stavros, *Phys. Chem. Chem. Phys.*, 2020, **22**, 25390-25395.
142. A. Bhattacherjee, M. Sneha, L. Lewis-Borrell, G. Amoruso, T. A. A. Oliver, J. Tyler, I. P. Clark and A. J. Orr-Ewing, *J. Am. Chem. Soc.*, 2021, **143**, 3613-3627.
143. M. H. Kao, R. K. Venkatraman, M. N. R. Ashfold and A. J. Orr-Ewing, *Chem. Sci.*, 2020, **11**, 1991-2000.
144. M.-H. Kao, R. K. Venkatraman, M. Sneha, M. Wilton and A. J. Orr-Ewing, *J. Phys. Chem. A*, 2021, **125**, 636-645.

Chapter 2. Experimental and computational methods

Transient absorption spectroscopy (TAS), using laser pulses of approximately 120 fs duration as determined via cross-correlation in a laser pump and probe experiment, is a powerful method to study the ultrafast photochemical dynamics of molecules in solution. Figure 2-1 shows the layout of the laser system used for the transient electronic absorption spectroscopy (TEAS) and transient vibrational spectroscopy (TVAS) studies presented in this thesis. Chapters 3– 5 of this thesis illustrate the detailed information about photochemical kinetics that can be extracted from such experimental measurements, revealing a great deal about the ultrafast dynamics in the excited electronic states accessed by absorption of UV light, and the ways these dynamics are affected by the surrounding solvent. The interpretation of TAS experimental data benefits from quantum chemical calculations of the energies and the properties of electronically excited states of the photoexcited molecules, and the vibrational frequencies of intermediate species and photochemical products. This

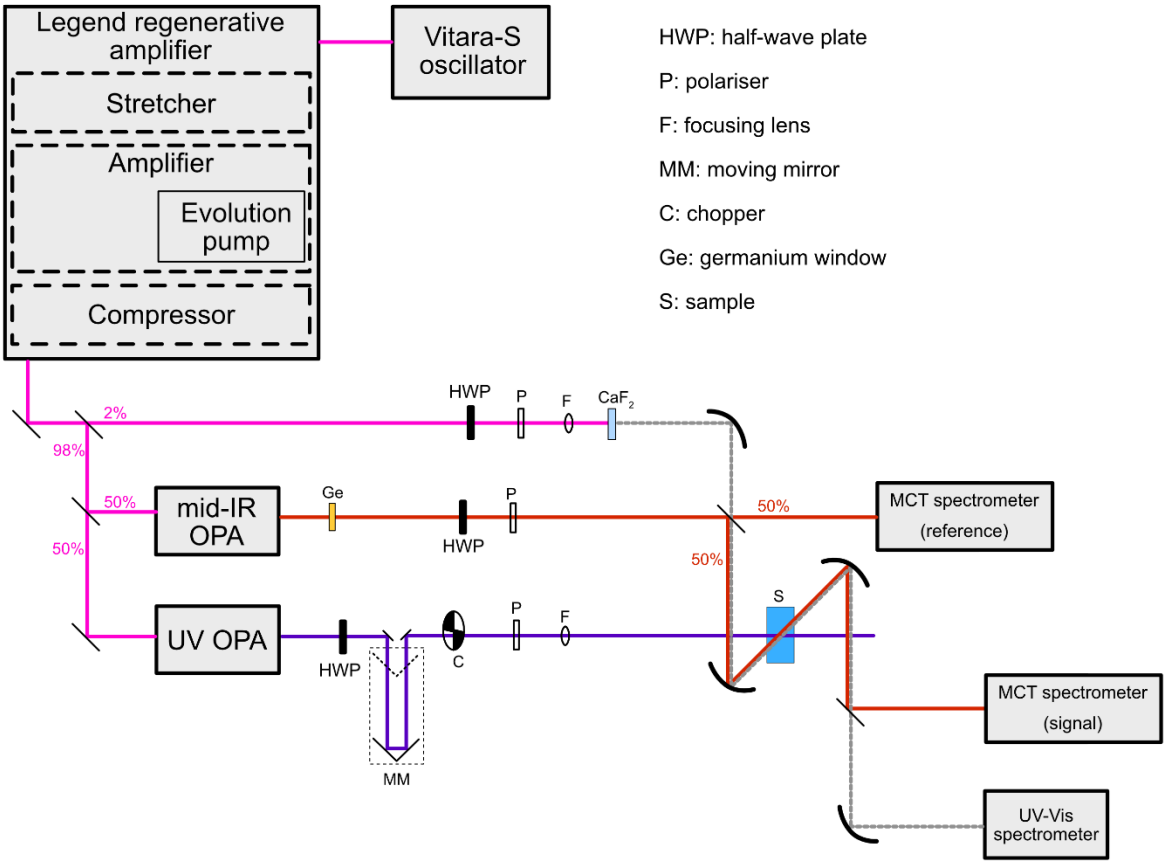

Figure 2- 1. A schematic diagram of the layout of the lasers and optics used for TEAS and TVAS experiments.

Chapter summarizes the methods used for both the laser-based experimental studies and the computational quantum chemistry calculations of molecular properties. Further details specific to the different molecular systems studied are reported in the relevant chapters.

2.1 Laser system

The photochemical dynamics reported in Chapters 3 - 5 were investigated using transient electronic and vibrational absorption spectroscopy methods with the ultrafast laser set-up at the University of Bristol shown schematically in Figure 2-1. All measurements relied on the same laser source, with ultrafast (~35 fs duration) laser pulses provided by a Coherent Vitara-S oscillator. This titanium-sapphire (Ti:sapphire) oscillator generates the femtosecond pulses by mode-locking, and the emitted pulse wavelengths are centred at 800 nm, in nearly transform-limited pulses, with a repetition rate of 80 MHz. The output pulses from the oscillator serve as a seed beam for a regenerative amplifier (Coherent Legend Elite HE+) consisting of three main parts: a stretcher, an amplifier, and a compressor illustrated in Figure 2-2. Gratings and curved mirrors used in both the stretcher and compressor stages vary the light path distances of different wavelengths contained in the ultrashort pulses, consequently changing the pulse duration by introducing temporal chirp. The duration of the pulses is stretched to ~150 ps, and thus the peak power is decreased after the stretcher to avoid the amplified pulses self-focusing and damaging the Ti:sapphire crystal in the amplifier stage. Recompression of the amplified pulses in the compressor stage produces ~35 fs duration pulses with energies of up to 5 mJ at a 1 kHz repetition rate.

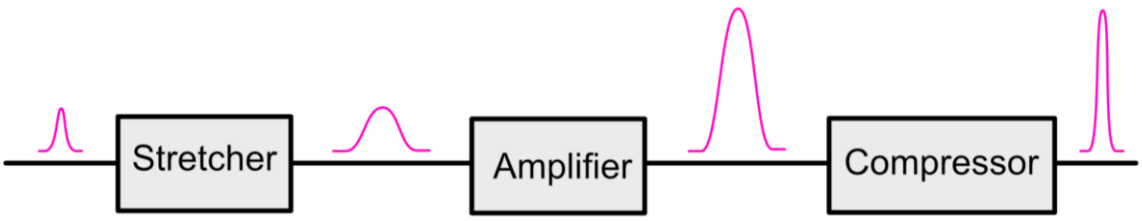

Figure 2- 2. Illustration of chirped pulse amplification. The duration of pulses is stretched before amplification, and then the duration is compressed back to restore a femtosecond pulse.

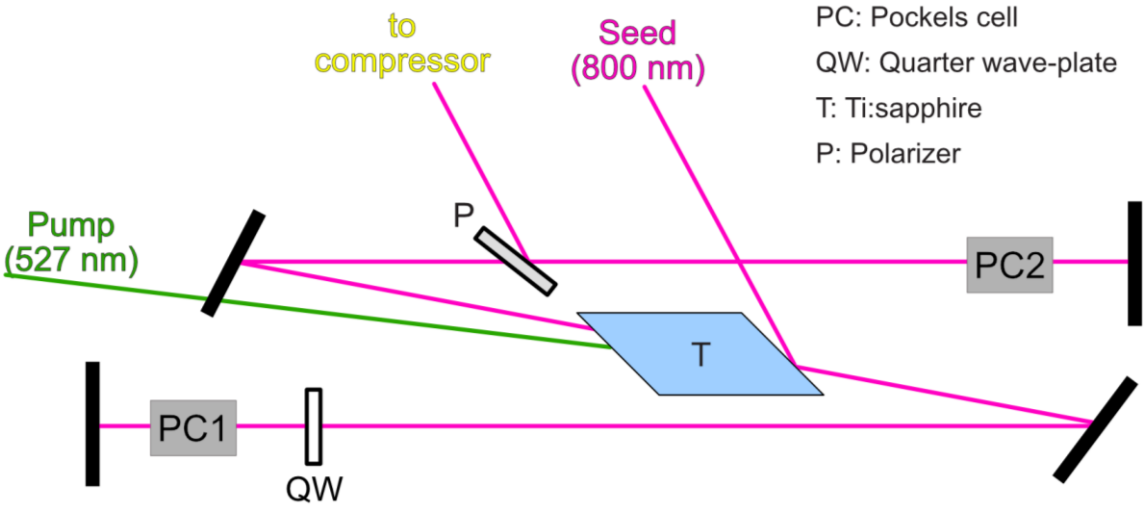

Figure 2- 3. Schematic layout of the amplifier cavity inside the Coherent Legend Elite.

Figure 2-3 shows a schematic diagram of the amplifier cavity. In the Ti:sapphire crystal, population inversion is achieved by absorption of radiation from an Evolution pump laser, which is a frequency doubled, Q-switched Nd:YLF laser emitting green light at a wavelength of 527 nm. The polarizer and Brewster windows on the Ti:sapphire crystal reflect S-polarized light but transmit the P-polarization. A Pockels cell is positioned either side of the Ti:sapphire crystal. These two components act as electro-optic shutters triggered by a synchronization and delay generator (SDG). When both Pockels cells are deactivated, the polarization of the seed beam (800 nm) is flipped from S-polarization to P-polarization after passing through a quarter wave-plate twice, and it travels through the entire amplifier cavity. However, the polarization is turned back to S-polarization in the next trip and reflected from the cavity. As a result, the seed beam will not be amplified significantly nor directed to compressor. On the contrary, activating the first Pockels cell allows a pulse from the Vitara-S oscillator every millisecond to stay in the cavity and prevents the seed beam from exiting the amplifier cavity by maintaining its P-polarization for several passages through the Ti:sapphire gain medium to build up its intensity by multiple stimulated emission events. The intensity of the seed beam is monitored by its leakage from the cavity using a photodiode. Once the intensity reaches a maximum, the second Pockels cell rotates the polarization of the amplified pulses to S-polarization, and the amplified pulses can therefore be reflected by the cavity polarizer, dumped from the amplifier cavity, and sent to the compressor. After the cavity, the repetition of the pulses is 1 kHz, and the pulses are amplified by a factor of ~10^6. A grating compressor

compresses the duration of pulses to ~40 fs. This entire process is known as chirped pulse amplification (Figure 2-2).[1]

The power of the output beam from the Coherent Legend Elite amplifier is around 5 W, and this output beam is split by a 98% beam splitter shown in Figure 2-1. The 2% of beam that passes through the beam splitter is delivered to a stage for white light continuum generation to produce the probe beam used in TEAS, and the remaining 98% of the beam reflected by the first beam splitter is further split into two by a 50% beam splitter, with the resulting laser beams directed to two Coherent OPerA-Solo optical parametric amplifiers (OPAs). These OPAs are configured to produce output pulses at wavelengths from 220 nm to around 11000 nm using nonlinear optical processes that happen in non-centrosymmetric crystals. One of the OPAs is set up to generate UV or visible pump pulses for photoexcitation of samples, and the other OPA produces mid-IR probe pulses for TVAS. Inside each OPA, the input 800-nm beam from the Ti:sapphire amplifier is split twice for frequency conversion in three different stages: a pre-amplifier stage, a power amplifier stage, and a mixer stage. A signal beam (~1010 nm – 1060 nm) is produced in the pre-amplifier stage, and it is amplified in the power amplifier stage where an idler beam (~1060 nm – 1160 nm) is also produced. The signal or idler beam is sent to the mixer stage, where mixing crystals can vary the resultant wavelength depending on their configurations (Figure 2-4). For example, fourth harmonic generation (FHG) of the signal (i.e. second harmonic generation (SHG) followed by another stage of SHG) can produce a 360-nm beam to photoexcite samples. Moreover, difference frequency generation (DFG) with the signal and idler results in a mid-IR beam used as a probe in TVAS. For TEAS or TVAS, pump wavelengths in the range from 270 nm to 245 nm are generated from SHG of the sum frequency of the signal and pump beams in the OPA. Longer wavelength UV around 280 nm to 290 nm for the pump laser is generated from SHG of the sum frequency of the idler and pump pulses in the OPA.

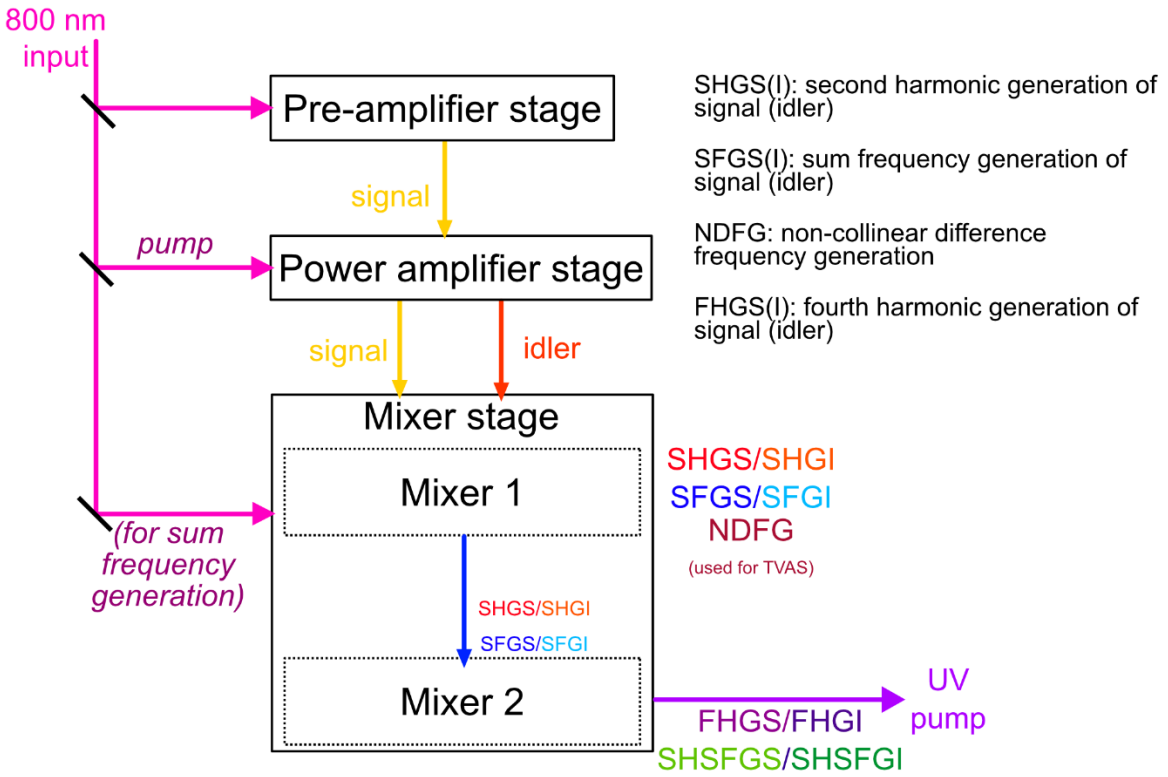

Figure 2- 4. Schematic illustration of an OPA layout showing use of nonlinear optical processes to generate the desired UV or mid-IR output beam.

The UV pump beam from the UV OPA passes through a half-wave plate that is used to tune the intensity of the pump laser pulses to control the degree of sample excitation and for power-dependent studies. The beam is then directed to a moving retroreflective mirror attached to a Thorlabs DDS220 mechanical stage which can provide a maximum time delay of 1.4 ns and minimum time steps of 3.5 fs for kinetics studies. A Thorlabs MC2000B-EC chopper wheel linked with the SDG reduces the repetition rate of the pump pulses to 500 Hz, whereas the repetition rate of the probe laser beams is kept as 1 kHz. This difference in pulse repetition rates allows comparison of sample spectra with and without the pump laser pulses so that transient absorption features can readily be identified. Before being focused into the sample using a lens, the pump beam passes through a polarizer to rotate its polarization to 54.7° from the vertical axis, the so-called magic angle, to eliminate any orientational diffusion signals from the transient absorption measurements.

10 mL of the sample solution is circulated by a peristaltic pump to reduce the chance of photodamage by the UV pump laser pulses, and it flows through a stainless-steel cell fitted

with two 1.5 mm thick CaF_2 windows separated by polytetrafluoroethylene (PTFE) spacers of a desired thickness (typically 100 – 380 μm). The flow rate of the sample solution is 0.5 – 1 mL/s. The pump beam and the probe beam are gently focused and spatially overlapped in the solution at the centre of the sample cell, and each sample solution is exposed to these pump and probe beams for 45 minutes to an hour during data acquisition. Typically, each time-delay point is averaged over 40 - 70 spectra, and after all time-delay points are collected, one cycle is completed. The transient absorption spectra are then obtained from the average of 6 - 8 such cycles. These measurements are repeated on different occasions to test the reproducibility of the transient spectra, but repeat measurements of time constants are not considered to be necessary.

2.2 Transient electronic absorption spectroscopy

For TEAS experiments, 2% of the output beam (λ = 800 nm) from the Coherent Legend Elite amplifier is used as a pump beam to generate the white-light continuum probe by self-phase modulation in a CaF_2 optic. A halfwave plate controls the intensity of the pump beam, and a polariser is used to keep the polarization vertical. The pump beam is focused on the back of a CaF_2 window rastering in a plane perpendicular to the beam propagation direction to avoid photodamaging the window. The white light continuum generated in the window typically spans wavelengths from 340 nm to near-IR, but the wavelengths above 700 nm are filtered. It is collimated by an off-axis parabolic mirror and focused onto the sample as a probe beam for visible and near-UV absorption spectroscopy. The probe beam transmitted through the sample is recollimated and directed into a spectrograph (Andor, Shamrock 163) with a 1024-element photodiode array (Entwicklungsbüro Stresing). Data are acquired with a Labview program, TApir, which also controls experimental time delays (by communication with the delay stage on the UV pump laser beam line) and data averaging. The pixel-to-wavelength calibration of the spectrometer is achieved by obtaining the spectrum of a holmium oxide crystal. Transient spectra are obtained from the difference in absorption between pump-on and pump-off measurements. Using the Beer-Lambert law, the difference in absorbance (ΔA)

$$\Delta A = A_{pump\ on} - A_{pump\ off} = -\log\frac{I_{pump\ on}}{I_0} + \log\frac{I_{pump\ off}}{I_0} = -\log\frac{I_{pump\ on}}{I_{pump\ off}}$$

Equation 2-1.

can be obtained from the light intensity transmitted through sample when the pump pulse is on ($I_{pump\ on}$) and the light intensity transmitted through sample when the pump laser pulse is blocked by the optical chopper and hence off ($I_{pump\ off}$), as shown in Equation 2-1. In this equation, I_0 is the incident light intensity, but this term is cancelled in Eq. 2-1.

2.3 Transient vibrational absorption spectroscopy

The mid-IR probe beam for TVAS is produced by the IR OPA, and similarly to the TEAS set-up, a halfwave plate and a polarizer are used to tune the power and keep the polarization vertical. A germanium window in the beam path filters the mid-IR wavelengths from those used in the NDFG process: the germanium window reflects near-IR radiation like the residual signal and idler beams from the IR OPA, and transmits the mid-IR probe beam. The mid-IR beam is split into two roughly equal portions by a germanium coated CaF_2 mirror. The reflected IR probe beam is focused into the sample and recollimated with the same optics used in the TEAS setup, and is then reflected and focused into a liquid nitrogen cooled Mercury Cadmium Telluride (MCT) 128-element array detector (Infrared Associates Inc., MCT-10-128) with fast read-out electronics (Infrared Systems Development Corp., FPAS-0144) coupled to a spectrometer (Horiba Scientific, iHR320). The portion of the mid-IR probe beam transmitted through the beam splitter is guided around the sample and focused into a second spectrometer fitted with a matching 128-element MCT array to provide a reference that is used to reduce noise from fluctuations in the IR beam intensity. TVA spectra data are also acquired using the TApir program, with wavelength calibration of spectra achieved using the bands observed in pure solvent samples such as acetonitrile. As with the analysis of TEAS measurements, the difference in absorbance is obtained from the intensity of IR light measured after the sample with the pump laser pulses on and off, but now with division by the intensity measured by the reference detector to reduce noise in the data (Equation 2-2).

$$\Delta A = -\log \frac{I_{pump\ on} / I_{ref,on}}{I_{pump\ off} / I_{ref,off}}$$

Equation 2-2.

2.4 Computational chemistry

Quantum-chemical computations of the energies, structures and spectra of stable molecules, excited states, and short-lived intermediates assist spectral assignments and data interpretation, and are conveniently performed using a range of commercial software packages. The time needed for running a calculation task depends on not only the size of the molecule but also the chosen quantum-chemical method, and the choices of functional and basis set. Typically, the more reliable the computational results are, the more computationally time-consuming the calculations are. The method used here for all the reported computations for molecules in their ground states is Density Functional Theory (DFT), and the properties of excited states are calculated with time-dependent DFT (TDDFT).[2-5] In DFT, properties such as molecular structures and energies are calculated from the probability distribution of the total electron density. A hybrid functional, B3YLP, is used for calculations for the sunscreen molecule diethylamino hydroxybenzoyl hexyl benzoate (DHHB) described in Chapter 4, and its long-range-corrected version with the Coulomb-attenuating method, CAM-B3YLP, [6, 7] is used for the study of chlorobenzene photochemistry reported in Chapter 5. Different basis sets are applied in these two projects because of molecular size differences and the focuses of the two studies. All the calculations run on a computer cluster, Grendel, at the University of Bristol, and use the Gaussian 09 package.[8]

The optimized structures and spectra of the sunscreen molecule DHHB are calculated with the basis set 6-31G (d,p).[9-15] This choice of the functional and basis set is guided by computations of other benzophenone derivatives by Corrêa *et al*.[16] In this 6-31G basis set, six Gaussian Type Orbitals (GTOs) represent the core orbitals, and three GTOs are used for the inner valence orbitals; one GTO is used for the outer valence orbitals. Polarization functions shown as (d,p) are introduced to give a d-function for heavy atoms and a p-function for hydrogen. To understand better the impact of the solvent environment on the photochemistry of DHHB, a Conductor-like Polarizable Continuum Model (CPCM) is applied to simulate solvation in polar and non-polar solvents.[17-20] The Polarizable Continuum Model (PCM) provides a continuous and uniform medium description of the solvent environment, and the medium is characterized with the dielectric constant of the solvent molecule. Consequently, specific interactions like intermolecular hydrogen bonds between solvent and solute molecules are not accounted for explicitly in the PCM treatment.[19, 20] CPCM is a derivative of PCM which imposes the dielectric constant of the medium to be infinite, like a

conductor, and to have no potential in the medium, but the polarization charges are distributed on the surface of the solvent cavity.[17, 18, 20]

The basis set chosen for the chlorobenzene project in Chapter 5 is aug-cc-pVTZ where "cc" stands for correlation consistent; that is, functions contributing similar correlation energies are included together despite the different function types. Polarization functions are added by default in cc-pVTZ.[21-25] "VTZ" denotes Valence Triple Zeta, applying three times as many functions as the minimum required. Diffuse functions are introduced, as is denoted by the "aug" label to indicate inclusion of functions with large size. The augmented basis set is suitable for systems where the electrons are relatively far from the nuclei, for example in anions and excited states.[24, 25] The choice of functional and basis set follows the methods used in computations of charge-transfer complexes of carbon tetrachloride.[26] Because the solvents used for the chlorobenzene experiments are non-polar and weakly interacting, such as cyclohexane and perfluorohexane, a solvation model is not used in order to reduce the calculational costs.

2.5 Spectral decomposition and data analysis

The transient absorption spectra measured in the Bristol ultrafast laser laboratory are processed and analysed in a custom-developed program called KOALA (Kinetics Observed After Light Absorption).[27] TAS measurements are pre-processed by subtracting a spectrum obtained at negative time (with the probe laser pulse preceding the pump laser pulse), baseline correction, and chirp correction (to account for any frequency chirp in the probe laser pulses). The subtraction of a spectrum obtained at negative time delay removes any contributions from long-live products and reduces the noise in the data. Because of the Gaussian intensity profile of the pump laser beam, a spatial gradient in molecular populations and solvent temperature is generated by UV absorption which causes refractive index gradients. Therefore, the baselines of spectra obtained at different time delays do not always stay the same, but the changes can be corrected in KOALA by aligning areas of the spectrum in which there are no transient spectral features. The areas chosen to define the baseline are selected by the program user, and typically the corrections applied are independent of, or linearly dependent on probe wavelength. In addition to this baseline dependence on the experimental time delays between the pump and probe pulses, each frequency in the broadband probe pulse arrives at the photoexcited sample region at a slightly different time

because of the wavelength dependence of the refractive indices of transmissive optics in the beam lines, the cell windows, and the solution. This frequency or spectral chirp is negligible for the TVAS data presented here, but is significant for TEAS measurements using a white-light continuum probe. As a result, the "time zero" of each frequency component in the time-resolved spectra can be shifted from those for other frequency components, giving different temporal offsets at each probe wavelength that can be hundreds of femtoseconds. KOALA allows straightforward chirp correction with a programmed formula accounting for the absolute phase, group delay dispersion and the third order dispersion.

Once the TEAS or TVAS measurements have been processed to eliminate spurious absorption of long-lived species, and to correct the spectral baselines and eliminate spectral chirp, they can be analysed to extract time-evolving spectral components from which transient intermediates are identified and their kinetics or lifetimes are deduced. To extract the photochemical kinetics, KOALA incorporates spectral decomposition using Gaussian functions and/or custom-designed spectral basis functions, and an example of spectral decomposition is shown in Figure 2-5a. KOALA also incorporates singular value decomposition (SVD) analysis to guide the choice of spectral basis functions when required. After fitting, the weights of each spectral basis function (whether Gaussian or custom-defined) are plotted against time as kinetic traces that can be fitted with exponential (or other) time-dependent functions in Origin software to obtain time constants and their associated uncertainties from regression analysis (Figure 2-5b).

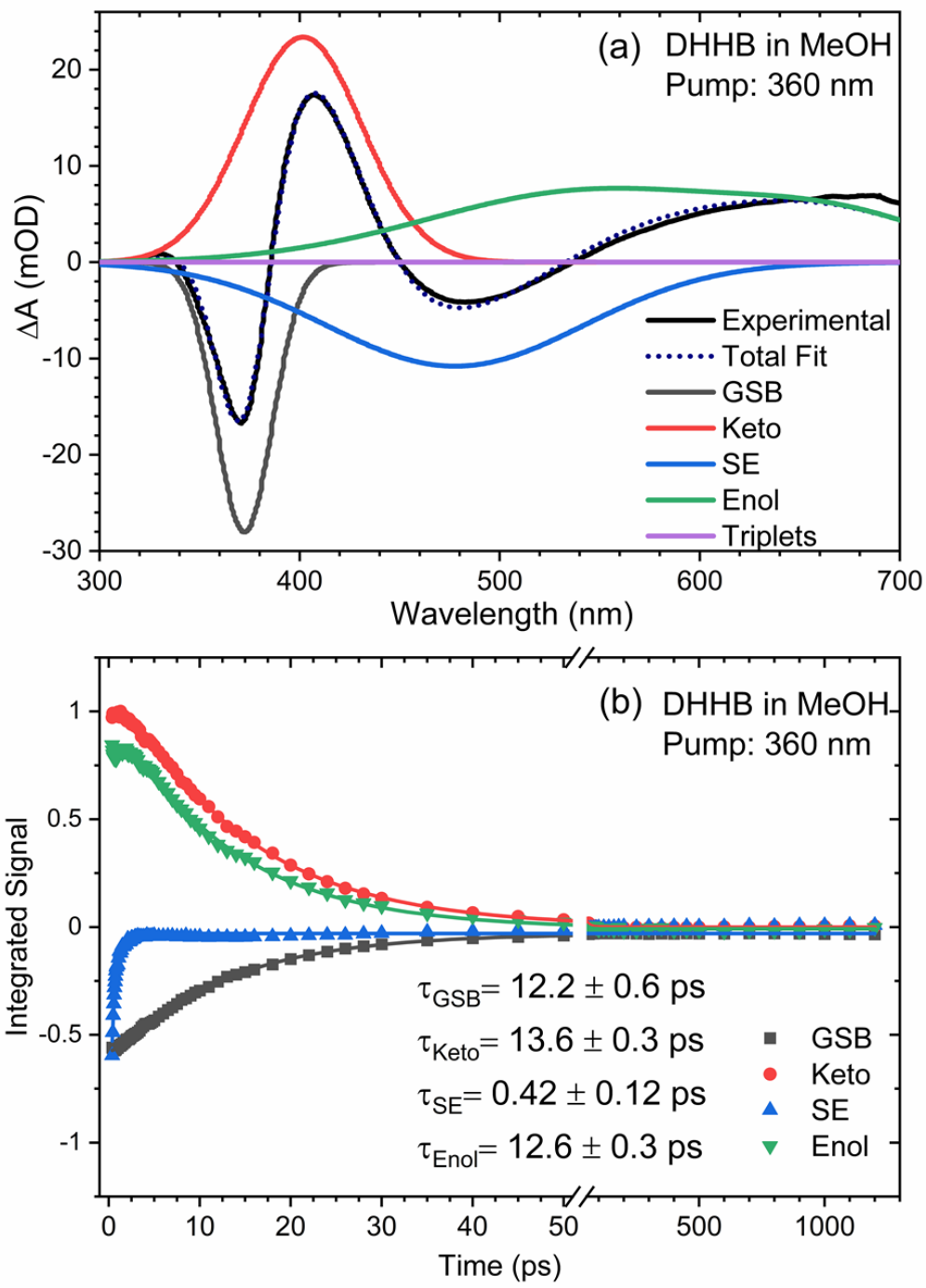

Figure 2- 5. (a) A TEA spectrum of DHHB at a given time delay (black) is spectrally decomposed into three Gaussian basis functions (grey, red, and blue) and two custom-designed basis functions (green and purple), and the total fit, which is the sum of the basis functions, is shown by the navy dotted-line. Details of the basis functions will be discussed in Chapter 4. (b) The kinetics extracted from the spectral decomposition of the experimental spectrum at every measured time delay (coloured symbols) are fitted with exponential functions (solid lines) in Origin, and the time constants and fit uncertainties are obtained.

References

1. D. Strickland and G. Mourou, *Opt. Commun.*, 1985, **56**, 219-221.
2. W. Kohn and L. J. Sham, *Phys. Rev.*, 1965, **140**, A1133-A1138.
3. M. E. Casida, C. Jamorski, K. C. Casida and D. R. Salahub, *J. Chem .Phys.*, 1998, **108**, 4439-4449.
4. R. Bauernschmitt and R. Ahlrichs, *Chem. Phys. Lett.*, 1996, **256**, 454-464.
5. A. D. Becke, *J. Chem. Phys.*, 1993, **98**, 5648-5652.
6. T. Yanai, D. P. Tew and N. C. Handy, *Chem. Phys. Lett.*, 2004, **393**, 51-57.
7. C. T. Lee, W. T. Yang and R. G. Parr, *Phys. Rev. B*, 1988, **37**, 785-789.
8. M. J. Frisch, G. W. Trucks, H. B. Schlegel, G. E. Scuseria, M. A. Robb, J. R. Cheeseman, G. Scalmani, V. Barone, B. Mennucci, G. A. Petersson, H. Nakatsuji, M. Caricato, X. Li, H. P. Hratchian, A. F. Izmaylov, J. Bloino, G. Zheng, J. L. Sonnenberg, M. Hada, M. Ehara, K. Toyota, R. Fukuda, J. Hasegawa, M. Ishida, T. Nakajima, Y. Honda, O. Kitao, H. Nakai, T. Vreven, J. A. Montgomery, J. E. Peralta, F. Ogliaro, M. J. Bearpark, J. J. Heyd, E. Brothers, K. N. Kudin, V. N. Staroverov, R. Kobayashi, J. Normand, K. Raghavachari, A. Rendell, J. C. Burant, S. S. Iyengar, J. Tomasi, M. Cossi, N. Rega, J. M. Millam, M. Klene, J. E. Knox, J. B. Cross, V. Bakken, C. Adamo, J. Jaramillo, R. Gomperts, R. E. Stratmann, O. Yazyev, A. J. Austin, R. Cammi, C. Pomelli, J. W. Ochterski, R. L. Martin, K. Morokuma, V. G. Zakrzewski, G. A. Voth, P. Salvador, J. J. Dannenberg, S. Dapprich, A. D. Daniels, O. Farkas, J. B. Foresman, J. V. Ortiz, J. Cioslowski and D. J. Fox, *Gaussian 09, Revision D.01*, 2013.
9. R. Ditchfield, W. J. Hehre and J. A. Pople, *J. Chem. Phys.*, 1971, **54**, 724-728.
10. M. M. Francl, W. J. Pietro, W. J. Hehre, J. S. Binkley, M. S. Gordon, D. J. Defrees and J. A. Pople, *J. Chem. Phys.*, 1982, **77**, 3654-3665.
11. M. S. Gordon, *Chem. Phys. Lett.*, 1980, **76**, 163-168.
12. P. C. Hariharan and J. A. Pople, *Theor. Chim. Acta.*, 1973, **28**, 213-222.
13. P. C. Hariharan and J. A. Pople, *Mol. Phys.*, 1974, **27**, 209-214.
14. W. J. Hehre, R. Ditchfield and J. A. Pople, *J. Chem. Phys.*, 1972, **56**, 2257.
15. M. J. Frisch, J. A. Pople and J. S. Binkley, *J. Chem. Phys.*, 1984, **80**, 3265-3269.
16. B. A. M. Corrêa, A. S. Gonçalves, A. M. T. De Souza, C. A. Freitas, L. M. Cabral, M. G. Albuquerque, H. C. Castro, E. P. Dos Santos and C. R. Rodrigues, *J. Phys. Chem. A*, 2012, **116**, 10927-10933.
17. V. Barone and M. Cossi, *J. Phys. Chem. A*, 1998, **102**, 1995-2001.
18. M. Cossi, N. Rega, G. Scalmani and V. Barone, *J. Comput. Chem.*, 2003, **24**, 669-681.
19. G. Scalmani and M. J. Frisch, *J. Chem. Phys.*, 2010, **132**, 114110.
20. J. Tomasi, B. Mennucci and R. Cammi, *Chem. Rev,*, 2005, **105**, 2999-3094.
21. T. H. Dunning, *J. Chem. Phys.*, 1989, **90**, 1007-1023.
22. K. A. Peterson, D. E. Woon and T. H. Dunning, *J. Chem. Phys.*, 1994, **100**, 7410-7415.
23. A. K. Wilson, T. Van Mourik and T. H. Dunning, *J. Mol. Struct. THEOCHEM*, 1996, **388**, 339-349.
24. R. A. Kendall, T. H. Dunning and R. J. Harrison, *J. Chem. Phys.*, 1992, **96**, 6796-6806.
25. D. E. Woon and T. H. Dunning, *J. Chem. Phys.*, 1993, **98**, 1358-1371.
26. F. Abou-Chahine, T. J. Preston, G. T. Dunning, A. J. Orr-Ewing, G. M. Greetham, I. P. Clark, M. Towrie and S. A. Reid, *J. Phys. Chem. A*, 2013, **117**, 13388-13398.
27. M. P. Grubb, A. J. Orr-Ewing and M. N. R. Ashfold, *Rev. Sci. Instrum.*, 2014, **85**, 064104.

Chapter 3. Effects of ring-strain on the ultrafast photochemistry of cyclic ketones

This chapter is adapted from the work published in *Min-Hsien Kao, Ravi Kumar Venkatraman, Michael N.R. Ashfold and Andrew J. Orr-Ewing, Chem. Sci., 2020,**11**, 1991-2000.* The author of this thesis contributed the design of experiments, data collection, data analysis, and interpretation.

3.1 Introduction

The Norrish Type-I ultraviolet (UV) photochemical reactions of aldehydes and ketones involve cleavage of a C–C bond adjacent to the carbonyl-group chromophore (i.e. α-cleavage), and have a long history dating back to the pioneering mechanistic investigations by Norrish and Bamford.[1] The accepted mechanism for Norrish Type-I α-cleavage is UV photoexcitation of an electron from a non-bonding orbital (*n*) on the carbonyl oxygen atom to a π^* molecular orbital of the carbonyl group (a weak $\pi^* \leftarrow n$ excitation, which is symmetry forbidden in the planar limit), followed by C–C bond cleavage in the first excited singlet (S_1) or triplet (T_1) state. The initial outcome is either two separate radical species, if the parent carbonyl compound is non-cyclic, or a biradical species if the parent is a cyclic ketone.[2] This Norrish photo-chemistry has been extensively exploited in a wide range of experiments, including photoinitiated polymerization, and chemical synthesis.[3-13] It is also significant in the photolysis of volatile carbonyl compounds such as acetone in the Earth's atmosphere.[14-18]

The biradical intermediates formed by α-cleavage of a cyclic ketone can further react in several different ways, with pathways that depend on the ring size of the ketone. UV-excited cyclobutanone, with only a four C-atom ring, has been reported to form either ethene and ketene, or CO and cyclopropane / propene photoproducts in both the gas phase and solution.[19-21] In contrast, cyclohexanone can photo-decompose to an alkene and CO, or photo-isomerize to 2-methyl-cyclopentane, 5-hexenal or 1-hexen-1-one.[22-28] Similarly, cyclopentanone isomerizes to 4-pentenal when irradiated with UV light at 313 nm or 254 nm.[29]

One way in which the ring size influences the photochemical reaction pathways of cyclic ketones is through the degree of ring strain. According to calculations using the complete basis set- atomic pair natural orbital (CBS-APNO) level of theory,[30] the ring strain energies of cyclohexanone and cyclopentanone are approximately 29 and 41 kJ mol^{-1}, respectively, whereas for cyclobutanone the corresponding value is significantly higher at ~120 kJ mol^{-1}.[31] Greater ring strain facilitates ring opening pathways in Norrish Type-I photochemistry. Xia *et al*. computed potential energies for extension of the α C–C distance for the S_1 and T_1 states of cyclobutanone, cyclopentanone and cyclohexanone using complete active space self-consistent field (CASSCF) and second-order perturbation theory (MS-CASPT2) methods.[32] Their results identified only a modest (~29 kJ mol^{-1} relative to the S_1 state minimum) energy barrier for α C–C cleavage in the S_1 state of cyclobutanone because C–C bond extension

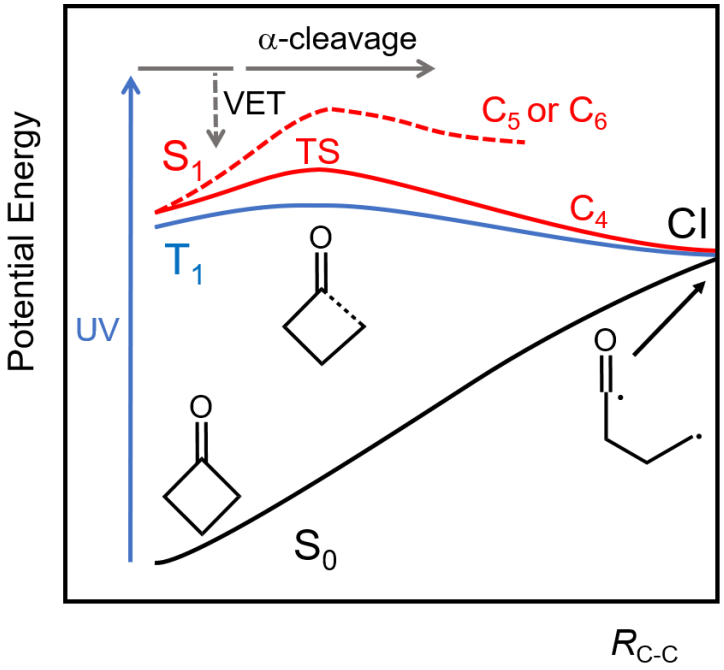

Figure 3- 1. Schematic diagram of cuts through the lowest lying potential energy surfaces for cyclobutanone (denoted by C_4) along the α C-C bond extension coordinate ($R_{C\text{-}C}$). The ground state (S_0, black curve) and first excited singlet (S_1, red) and triplet (T_1, blue) states converge to near-degenerate biradical structures at large $R_{C\text{-}C}$, with S_0 and S_1 meeting at a conical intersection (CI). An energy barrier of ~29 kJ mol^{-1} on the S_1 state corresponds to the transition state (TS) for α-cleavage. The corresponding barrier heights for cyclopentanone (C_5) and cyclohexanone (C_6) are higher, as indicated by the dashed red line. UV photoexcitation in the present experiments populates the S_1 state above the energy of the TS, and direct C-C α-cleavage competes with vibrational energy transfer (VET) to the solvent. Intersystem crossing (ISC) to T_1 accesses a pathway to α-cleavage with a lower energy barrier.

relieves the ring strain, whereas the corresponding barrier heights for cyclopentanone and cyclohexanone are ~63 kJ mol^{-1} or more. In contrast, the calculations show no significant barriers to α C–C bond cleavage on the T_1-state potential energy surfaces of these molecules, suggesting cyclopentanone and cyclohexanone can undergo facile α-cleavage in this triplet state after intersystem crossing (ISC) from S_1, as is shown schematically in Figure 3-1.[32] Nevertheless, molecular dynamics simulations done by Shemesh *et al*., using the orthogonalization-corrected method 2 / multireference configuration interaction (OM2/ MRCI) method for potentials and Surface Hopping including Arbitrary Couplings (SHARC) software for dynamics, showed most photoexcited cyclohexanone molecules (with a range of internal energies in the S_1 state) reacting on timescales shorter than 100 ps, i.e. at a rate that out-competes ISC. Thus, these calculations suggest that α-cleavage is possible for S_1 state cyclohexanone molecules with sufficient internal energy.[28]

Both the relative yields of competing photoproducts of cyclobutanone photochemistry, and the intensity of its excited state emission, vary with UV excitation wavelength.[33] In the gas phase, the ratio of the ethene + ketene channel to CO + cyclopropane / propene formation drops from 7 to 0.4 when the excitation wavelength decreases from ~340 nm to ~310 nm.[34] Furthermore, the lifetime of the cyclobutanone S_1 state reduces in the gas phase or in cyclohexane solution, and consequently the fluorescence emission intensity declines rapidly, for excitation wavelengths below 320 nm.[35] The fluorescence quantum yields (Φ_f) of cyclopentanone and cyclohexanone also decrease with shorter excitation wavelength, but to a lesser extent than for cyclobutanone.[33, 35-37] At wavelengths around 310 nm, the three cyclic ketones have Φ_f values of ~0.2%.[37]

Femtosecond time-resolved spectroscopy has also been applied to study Norrish Type-I photochemistry in the gas phase, with Zewail and coworkers observing the kinetics of α-cleavage in cyclobutanone in the gas phase. At an excitation wavelength of 307 nm (corresponding to an energy above, but close to the S_1 barrier height), a measured time constant of ~5 ps was assigned to C-C bond fission.[38] The current study extends this ultrafast time-resolved spectroscopy approach to the condensed phase, and to a range of UV excitation wavelengths, to explore the effects of S_1-state internal energy on excited state pathways. It compares the photochemistry of cyclobutanone with cyclopentanone and cyclohexanone to examine the consequences of ring strain on the Norrish Type-I pathway.

Cyclohexane was chosen as a medium for all the reported measurements to study the effects of competition between direct α-cleavage and S_1-state relaxation by vibrational energy transfer (VET) (Figure 3-1). In this weakly interacting solvent, solute-solvent interactions are not expected to modify significantly the excited state potentials and energy barriers compared to the gas phase. Transient electronic absorption spectroscopy (TEAS) reveals the timescales for decay of S_1 population in these three molecules, whereas transient vibrational absorption spectroscopy (TVAS) identifies some of the active ring-opening reaction pathways.

3.2 Experimental methods

Transient absorption spectra were measured using an ultrafast laser system at the University of Bristol which has been described in Chapter 2. Cyclobutanone (99%, Sigma-Aldrich), cyclopentanone ($\geq$ 99.0%, Sigma-Aldrich ReagentPlus) and cyclohexanone ($\geq$ 99.0%, Sigma-Aldrich, ACS reagent) were used without further purification to prepare 1 M solutions in cyclohexane (Supelco, Spectroscopy grade). These solutions were circulated by a peristaltic pump through a stainless-steel sample cell fitted with two 1.5-mm thick CaF_2 windows separated by a 380-μm Teflon spacer for transient absorption spectroscopy. Steady-state UV/vis absorption spectra of the samples in a 2-mm-pathlength cuvette and a 380-μm-pathlength stainless-steel sample cell were obtained using a GENESYS™ 10S UV-Vis Spectrophotometer (Thermo Scientific). The absence of aggregation of cyclic ketones was checked by comparing the normalised steady-state UV/vis absorption spectra of 100 mM solutions in a 2-mm-pathlength cuvette and 1 M solutions in a 380-μm-pathlength sample cell, for which no band shifting was observed. Corresponding IR absorption spectra were measured by a Spectrum Two FTIR Spectrometer (Perkin Elmer), with samples held in cells of the type used for transient absorption spectroscopy but with CaF_2 windows separated by 100-μm Teflon spacers.

3.3 Results and discussion

3.3.1 Transient electronic absorption spectra

The weak $\pi^* \leftarrow n$, $S_1 - S_0$ absorption band of cyclobutanone is typical of a carbonyl compound,[36, 39] and spans UV wavelengths from 240 - 330 nm, with a maximum absorbance close to 280 nm in cyclohexane solution. Cyclopentanone and cyclohexanone have similar $\pi^* \leftarrow n$ absorption bands, with respective maxima at ~300 and 290 nm. Example UV/visible spectra are shown in Figure 3-2. The UV excitation wavelengths selected for TEAS measurements were λ_{exc} = 255, 281, 290 and 312 nm to span much of the range of these weak absorption features, and based on theoretical predictions longer wavelengths are expected to access regions of the S_1 state only just above the energy of the barriers for excited-state α C-C bond fission.

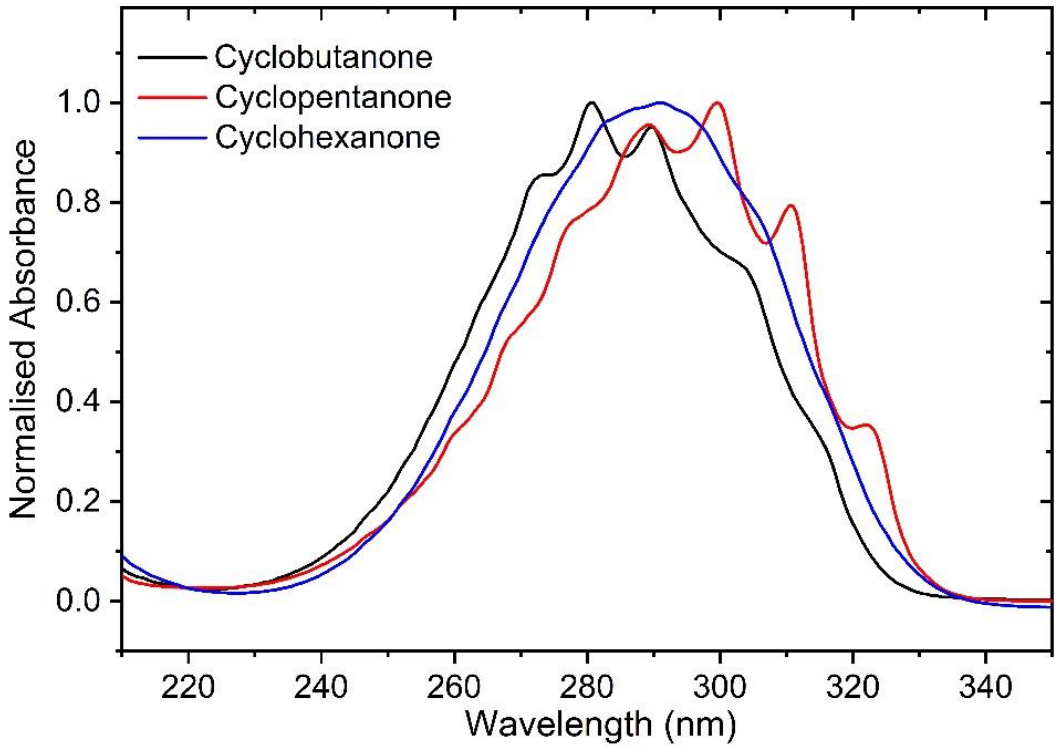

Figure 3- 2. Normalised UV/Vis absorption spectra of cyclobutanone (black), cyclopentanone (red) and cyclohexanone (blue) in cyclohexane. The concentrations of the solutions used for the measurements were 0.25 M, and the cuvette pathlength was 2 mm.

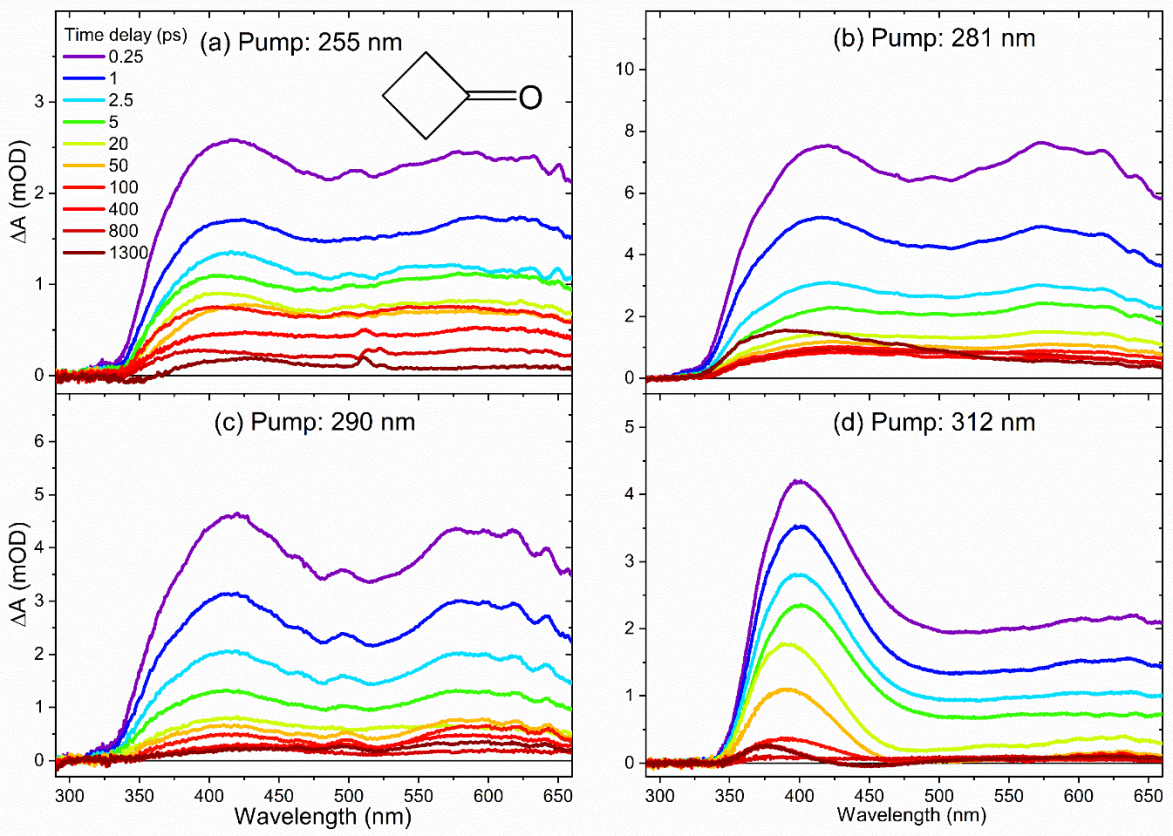

Figure 3- 3. TEA spectra of cyclobutanone in cyclohexane, obtained with excitation wavelengths of (a) 255 nm, (b) 281 nm, (c) 290 nm and (d) 312 nm. The spectra were recorded at different pump-probe time delays, as indicated by the inset colour key in the top panel.

Figure 3-3 shows representative TEA spectra of cyclobutanone in cyclohexane at the four different excitation wavelengths. In these and other such spectra, the intensity of the white light continuum probe weakens and then cuts off at wavelengths below 350 nm, so the spectra are not correctly captured in this region. Different colour traces correspond to spectra obtained at various time delays shown by the inset key. At the shortest chosen pump wavelength of 255 nm, two broad peaks are observed in the excited state absorption (ESA) bands, located at around 420 nm and 600 nm. Similar structures are evident in the transient spectra obtained at λ_{exc} = 281 nm and 290 nm. However, the 600-nm ESA feature is no longer as distinct when a cyclobutanone solution is excited with 312-nm UV light. The intensities of the transient absorption bands decay almost to zero over the timescale of the measurements (with maximum time delays of 1300 ps). Any stimulated emission contribution to the TEA spectra is expected at wavelengths around 350 - 500 nm, but will be weak in comparison to

transition- dipole allowed $S_m \leftarrow S_1$ (m>1) ESA bands because the $S_1 \rightarrow S_0$ $\pi^* \rightarrow n$ transition involved is forbidden in the planar limit.

The transient absorption spectra reflect the degree of internal (vibrational) energy of the photoexcited S_1 state molecules, and perhaps some T_1-state contributions after ISC, because other electronically excited states are not accessible at the pump photon energies. At the shortest time delay of Δt = 0.25 ps, the vibrational excitation of the S_1-state molecules will not have had time to relax by coupling to the degrees of freedom of the solvent bath for a weakly interacting solvent such as cyclohexane. [40, 41] Hence, for each excitation wavelength

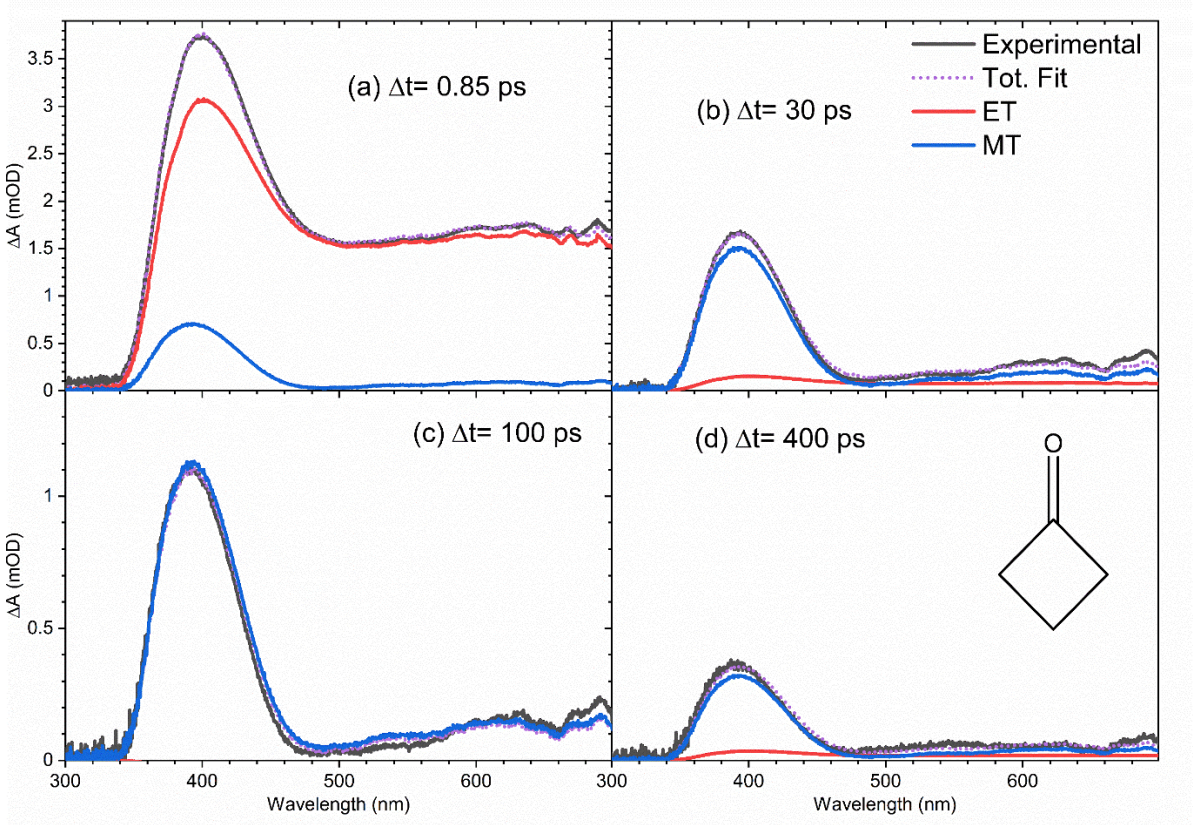

Figure 3- 4. Example of the decomposition of TEA spectra of a cyclobutanone solution in cyclohexane using early and medium time (ET and MT) basis spectra corresponding to the experimental spectra measured at Δt = 0.2 and 50 ps, respectively. The TEA spectra were obtained at an excitation wavelength of 312 nm, and the decomposition was performed in the KOALA program. The sample spectra plotted were taken at three different time delays: (a) 0.85 ps, (b) 30 ps, (c) 100 ps and (d) 400 ps. In each case, the black solid line is the experimental spectrum, and the purple dashed line is the best fit. ET and MT basis functions are shown as red and blue solid lines, respectively. Decomposition of cyclobutanone spectra obtained at shorter excitation wavelengths (λ_{exc} = 255, 281 and 290 nm) required use of only a single (ET) basis function.

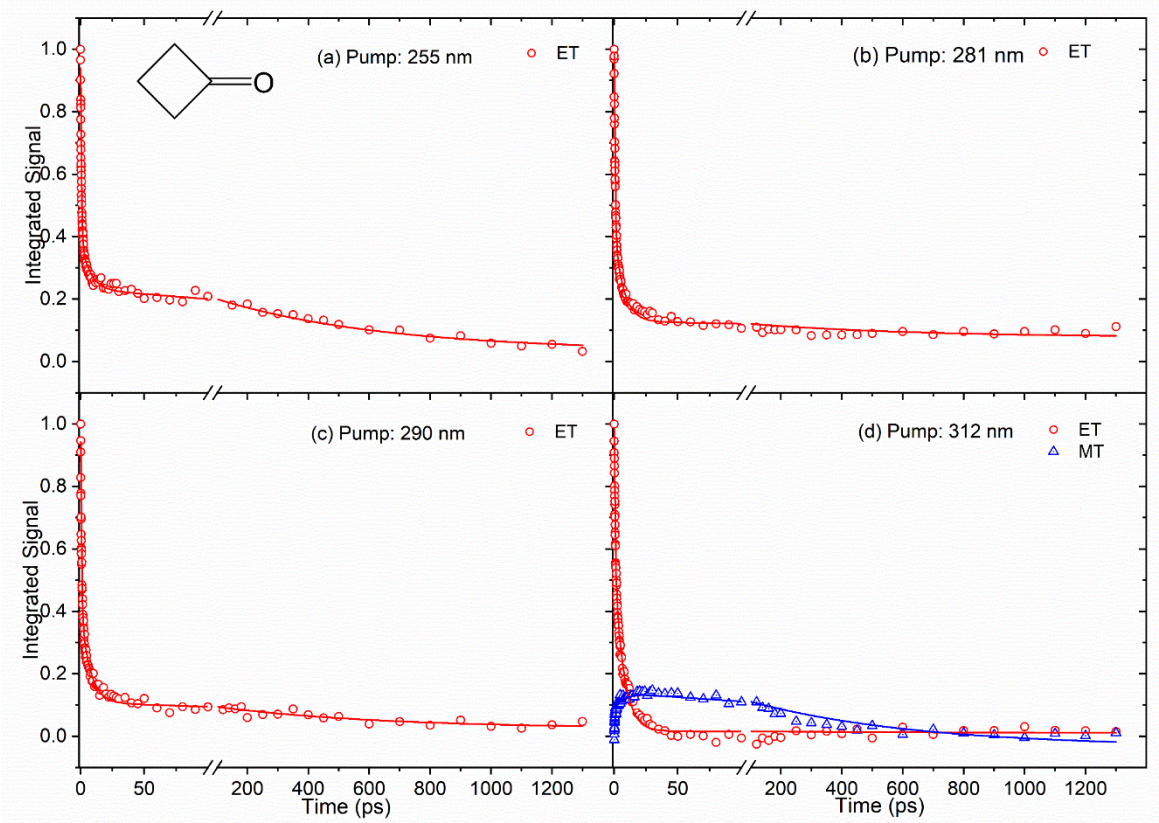

Figure 3- 5. Kinetics of cyclobutanone (S_1) relaxation obtained by analysis of TEA spectra (Figure 3-3) measured at four UV excitation wavelengths. Red and blue symbols are intensities obtained from the fits to ET and MT basis functions (see main text). The solid lines are a global fit of all the data sets to tri-exponential decay functions with constant offsets, yielding decay components with common time constants of 0.65 ± 0.12, 7.0 ± 0.2 and 550 ± 45 ps.

data set, the corresponding early time (ET) spectrum (Δt = 0.25 ps) was used as a basis function to model the contribution from vibrationally hot S_1-state molecules to the TEA spectra. This single basis spectrum, with steadily decreasing amplitude, was sufficient to describe well the temporal evolution of the broadband, time-resolved TEA spectra of cyclobutanone in cyclohexane for pump wavelengths of 255 nm, 281 nm and 290 nm. However, at λ_{exc} = 312 nm, the spectral decomposition analysis required inclusion of a second basis function, which was chosen to be the TEA spectrum obtained at Δt = 50 ps, denoted here as a medium-time (MT) spectrum. Figure 3-4 illustrates this spectral fitting to ET and MT basis functions for the 312-nm excitation of cyclobutanone, giving the data plotted in Figure 3-5(d). The MT spectrum is interpreted as representing the absorption by S_1-state cyclobutanone molecules which have undergone vibrational cooling to internal energies below the S_1 α-cleavage barrier.

On the basis of the analysis presented below, this vibrational cooling is determined to be essentially complete on a timescale shorter than 50 ps. The interpretation of the MT basis spectrum is supported by evidence from steady-state fluorimetry measurements of weak fluorescence at blue and green wavelengths corresponding to emission from a fraction of the photoexcited S_1 molecules which avoid photochemical pathways and instead relax to the lowest S_1 vibrational level. [34, 35, 42] This fraction (as judged from the relative fluorescence intensities) is greatest at the longest excitation wavelengths used in the current time-resolved studies.

Cyclobutanone						
Pump wavelength (nm)	τ_1		τ_2		τ_1/τ_2	
	Amplitude	error	Amplitude	error	Amplitude	error
255	0.57	0.01	0.16	0.01	3.56	0.18
281	0.69	0.01	0.30	0.01	2.30	0.07
290	0.68	0.02	0.31	0.01	2.19	0.08
312	0.56	0.01	0.57	0.01	0.98	0.02

Table 3- 1. Amplitudes of the fastest (τ_1= 0.65 ± 0.02 ps) and intermediate (τ_2= 7.0 ± 0.2 ps) time components of the tri-exponential decays of intensity of ET basis function observed by decomposition of TEA spectra of photoexcited cyclobutanone. Data are shown for four different UV excitation wavelengths. τ_1/τ_2 ratios show that the contribution of the fastest time constant decreases with longer excitation wavelengths.

Fitting of the time-dependent spectra of Figure 3-3 to the chosen basis spectra was performed in KOALA,[43] and gave the decays of ESA band intensities plotted in Figure 3-5. The kinetics of the decays can be extracted by global fitting (in Origin) of all the data for multiple excitation wavelengths using tri-exponential functions with a constant offset, yielding time constants of τ_1 = 0.65 ± 0.12 ps, τ_2 = 7.0 ± 0.2 ps and τ_3 = 550 ± 45 ps. The corresponding amplitudes of the separate time components extracted from the ET basis function fits are reported in Table 3-1, and the ratios of amplitudes for the τ_1 and τ_2 components are plotted in Figure 3-6. Such amplitude ratios quantify the relative importance of each mechanistic contribution to the S_1-state decay. As the UV pump wavelength increases (and photon excitation energy decreases), the relative contribution of the fastest (0.65 ps) time component becomes less significant. Because of the timescale, this component is attributed to direct α C-C bond cleavage in the S_1 state. The wavelength-dependent trend suggests that with decreasing initial internal energy, a smaller fraction of the UV-excited molecules directly traverses the barrier to α C-C bond fission on the S_1 potential energy surface. Surmounting this energy barrier will require

internal vibrational energy redistribution (IVR) if the initial photoexcitation does not place sufficient initial energy in motion along, or strongly coupled to, the reaction coordinate. The observed 7.0 ps timescale may therefore be associated in part with this IVR,[38] consistent with its increasingly prominent role as the total internal energy decreases (λ_{ex} increases).

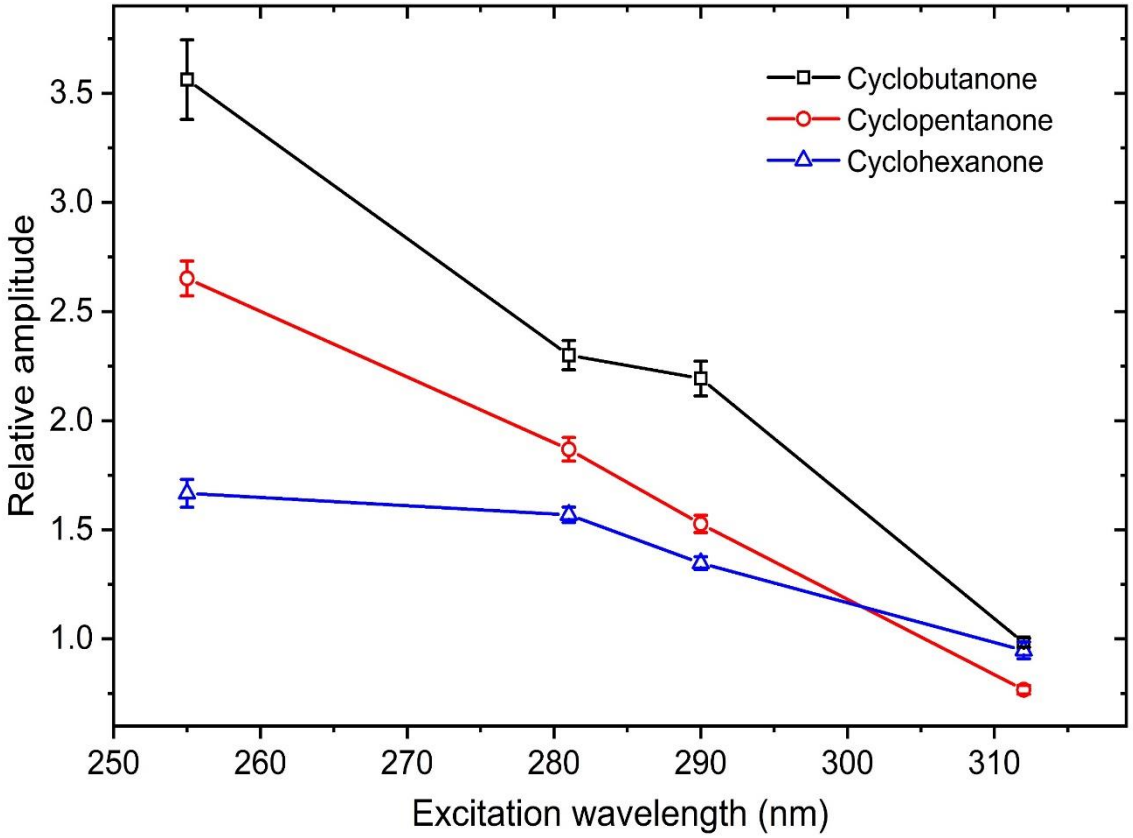

Figure 3- 6. Relative amplitudes of the shortest (τ_1) and intermediate (τ_2) time components of the tri-exponential decays of intensity in TEA spectra of photoexcited cyclobutanone, cyclopentanone and cyclohexanone. Data are shown for four different UV excitation wavelengths. The amplitudes of the τ_1 (<1 ps) components are divided by the amplitudes of the corresponding τ_2 (7-9 ps) components to compare the influence of different excitation wavelengths.

Any remaining absorption apparent in the late-time cyclobutanone TEA spectra, interpreted as arising from vibrationally cooled S_1 molecules, should be treated with some caution because of the weakness of the features. Moreover, band shapes are not fully resolved because the WLC probe does not extend to wavelengths below ~350 nm.

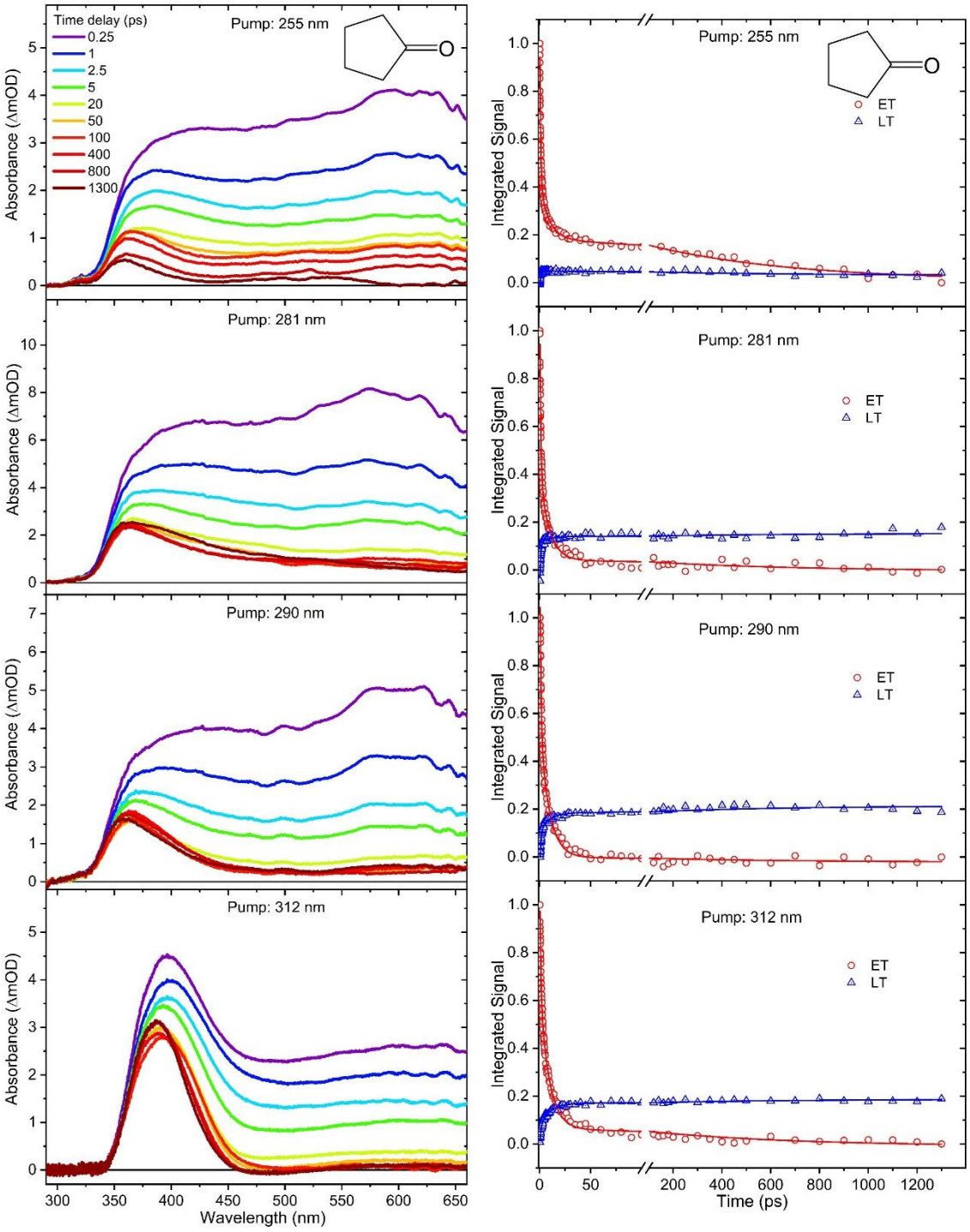

Figure 3- 7. Left-hand column: TEA spectra of cyclopentanone in cyclohexane, obtained with excitation wavelengths of 255 nm, 281 nm, 290 nm and 312 nm (from top to bottom). The spectra were obtained at different pump-probe time delays, as indicated by the inset colour key. Right-hand column: kinetics of excited state cyclopentanone relaxation obtained by analysis of TEA spectra. Red and blue symbols are intensities obtained from the fits to ET and LT basis functions. The solid lines are a global fit to tri-exponential functions with constant offsets, yielding components with common time constants of τ_1 = 0.95 ± 0.12 ps, τ_2 = 8.5 ± 0.3 ps and τ_3 = 600 ± 100 ps.

Figure 3-7 shows the corresponding TEA spectra of cyclopentanone at the same excitation wavelengths with cutoffs for wavelengths below 350 nm. These transient spectra have similar characteristics to those exhibited by cyclobutanone. The TEA spectra are again broad and mostly featureless, but with maxima at wavelengths around 400 nm and 600 nm for λ_{exc} = 255 nm, 281 nm and 290 nm. For λ_{exc} = 312 nm, the 400-nm transient absorption band is the most prominent, and in all cases a feature peaking at wavelengths between 350 and 400 nm remains clearly visible in spectra obtained at Δt = 1300 ps, in contrast to the almost complete decay of ESA for cyclobutanone.

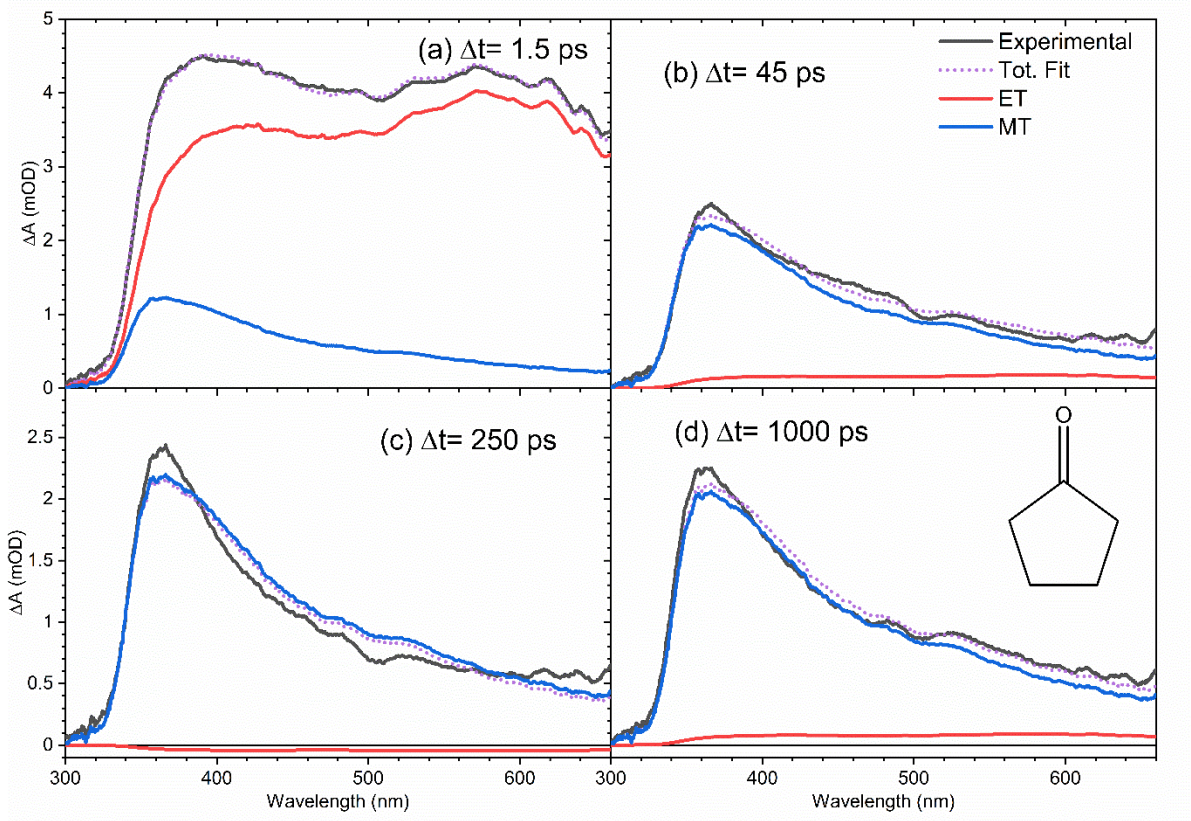

Figure 3- 8. Example of the decomposition of TEA spectra of a cyclopentanone solution in cyclohexane using early and late time (ET and LT) basis spectra corresponding to experimental spectra measured at Δt = 0.2 and 1300 ps, respectively. The TEA spectra were obtained at an excitation wavelength of 281 nm, and the decomposition was performed in the KOALA program. The sample spectra plotted were taken at three different time delays: (a) 1.5 ps, (b) 45 ps, (c) 250 ps and (d) 1000 ps. In each case, the black solid line is the experimental spectrum, and the purple dashed line is the best fit. ET and LT basis functions are shown as red and blue solid lines respectively.

Spectral decomposition in KOALA followed a similar approach to that described above for the cyclobutanone TEAS studies: data were fitted to an ET basis function obtained at Δt = 0.25 ps, but in this case it was also necessary to include a second basis function denoted as late-

time (LT) to account for the full time-evolution of the spectra. The LT basis function was chosen to be the spectrum obtained at Δt = 1300 ps for each of the different λ_{exc} data sets. An example spectral decomposition is shown in Figure 3-8. This analysis reveals continual decay of the ET contribution and corresponding growth of the LT feature. Figure 3-7 shows the corresponding kinetics and fitting for cyclopentanone excited at four UV wavelengths. A global kinetic fit with tri-exponential functions yields common time constants of τ_1 = 0.95 ± 0.12 ps, τ_2 = 8.5 ± 0.3 ps and τ_3 = 600 ± 100 ps for excited-state cyclopentanone, and the relative amplitudes are reported in Table 3-2. The fastest (τ_1) component dominates at λ_{exc} = 255 nm but, as Figure 3-6 shows, its relative amplitude decreases as the excitation wavelength increases.

Cyclopentanone						
Pump wavelength (nm)	τ_1		τ_2		τ_1/τ_2	
	Amplitude	error	Amplitude	error	Amplitude	error
255	0.61	0.01	0.23	0.01	2.65	0.08
281	0.71	0.01	0.38	0.01	1.87	0.05
290	0.87	0.02	0.57	0.01	1.53	0.04
312	0.46	0.01	0.60	0.01	0.77	0.02

Table 3- 2. Amplitudes of the fastest (τ_1 = 0.95 ± 0.03 ps) and intermediate (τ_2 = 8.5 ± 0.3 ps) time components of the tri-exponential decays of ET basis function intensity observed by decomposition of TEA spectra of photoexcited cyclopentanone. Data are shown for four different UV excitation wavelengths. τ_1/τ_2 ratios show that the contribution of the fastest time constant decreases with longer excitation wavelengths.

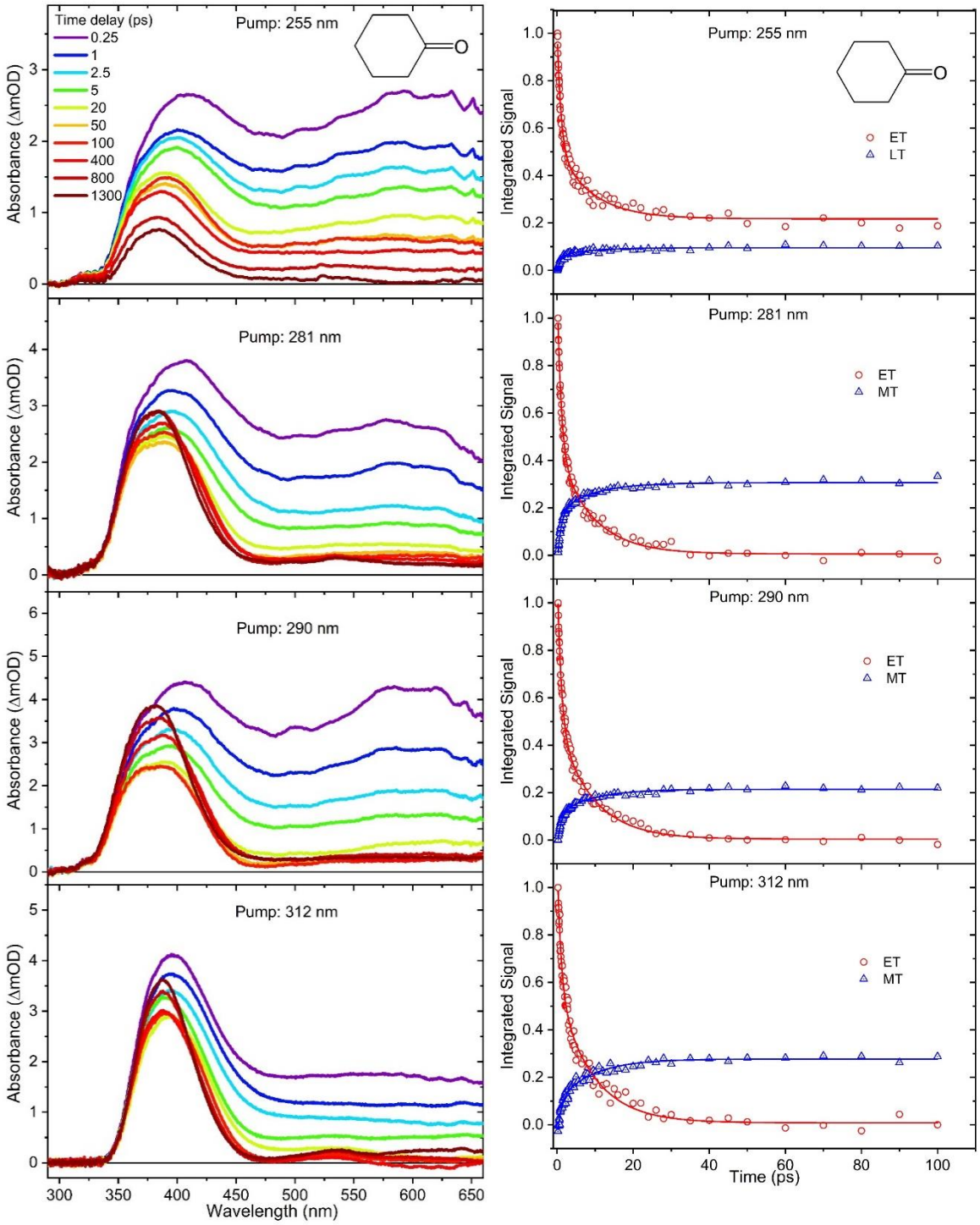

Figure 3- 9. Left-hand column: TEA spectra of cyclohexanone in cyclohexane, obtained with excitation wavelengths of 255 nm, 281 nm, 290 nm and 312 nm. The spectra were obtained at different pump-probe time delays, as indicated by the inset colour key. Right-hand column: kinetics of excited state cyclohexanone relaxation obtained by analysis of TEA spectra measured at time delays up to 100 ps. Red and blue symbols are intensities obtained from the fits to ET and MT basis functions. The solid lines are a global fit to bi-exponential functions, yielding components with common time constants of τ_1 = 1.02 ± 0.03 ps and τ_2 = 8.9 ± 0.3ps.

TEA spectra obtained for solutions of cyclohexanone in cyclohexane are shown in Figure 3-9 with cutoffs for wavelengths below 350 nm. The transient spectra for cyclohexanone bear superficial resemblance to the data obtained for cyclopentanone. At an excitation wavelength of 255 nm, the ESA bands decay in a similar fashion to cyclopentanone, leaving a residual absorption band centred just below 400 nm. However, close inspection of the spectra obtained at λ_{exc} = 281 nm, 290 nm and 312 nm reveals a rapid decline in the broad absorption band for time delays up to Δt = 50 ps, and the growth and narrowing of a band centred near 370 nm at time delays longer than 140 ps. Spectral decomposition therefore required use of three basis functions: ET and LT functions were represented by Δt = 0.25 ps and 1300 ps TEA spectra, respectively, and a middle-time (MT) function was added using the spectrum obtained at Δt = 100 ps. This time delay was chosen because the ESA signals above 475 nm are weak and did not change after 50 ps, so the ET basis function no longer contributes to the overall TEA spectra after this time. Moreover, the narrower band located around 370 nm does not evolve in shape and intensity over time delays from 50 to 140 ps, at which point there is an onset of growth and a change to the band shape in this spectral region. Hence, the kinetics can be cleanly divided into a short-time ($\Delta t \leq$ 100 ps) and a long-time ($\Delta t \geq$ 100 ps) component. The short time data were analyzed by spectral decomposition using the ET and MT basis functions (Figure 3-10), to give time-dependent band intensities of the type shown in Figure 3-9. For time delays in excess of 100 ps, the MT and LT basis functions were used instead. However, the time constants from the fits are significantly over the experimental time window, and therefore, the time constants and spectral decompositions are not reported in this chapter.

As Figure 3-9 shows, the decay and growth kinetics of ESA features for cyclohexanone in cyclohexane at time delays up to 100 ps can be globally fitted for all excitation wavelengths with bi-exponential functions with shared time constants. The common time constants emerging from these fits are τ_1 = 1.0 ± 0.1 ps and τ_2 = 8.9 ± 0.3 ps. Fit amplitudes are reported in Table 3-3. The ratio of the amplitudes for the τ_1 and τ_2 components decreases from 1.67 ± 0.06 to 0.95 ± 0.04 with increasing pump wavelength (Figure 3-6). The relative amplitude of the spectral component with shortest time constant is smaller for cyclohexanone than for cyclobutanone, suggesting a lesser contribution from the direct S_1-

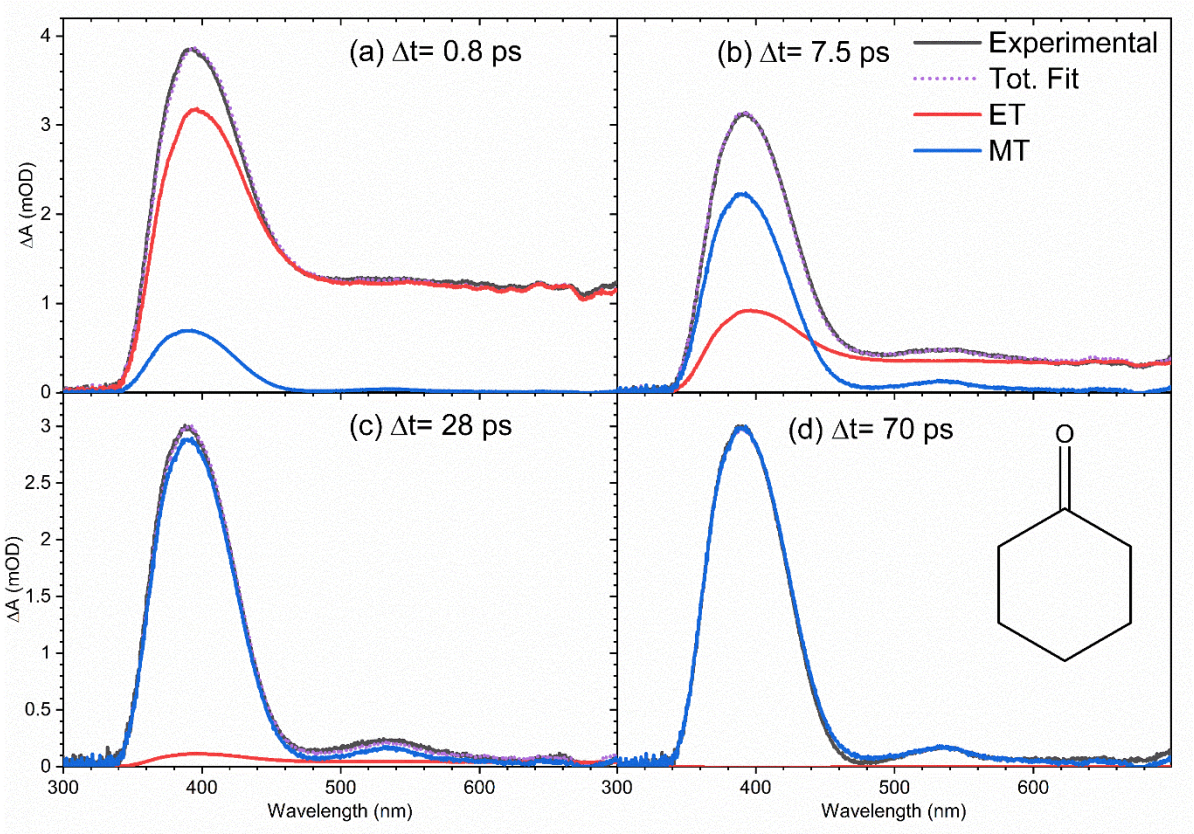

Figure 3- 10. Example of the decomposition of TEA spectra of a cyclohexanone solution in cyclohexane using early and medium time (ET and MT) basis spectra which correspond to experimentally measured spectra at Δt = 0.3 and 100 ps, respectively. The TEA spectra were obtained at an excitation wavelength of 312 nm, and the decomposition was performed in the KOALA program. The sample spectra plotted were taken at three different time delays: (a) 0.8 ps (top), (b) 7.5 ps, (c) 28 ps and (d) 70 ps. In each case, the black solid line is the experimental spectrum, and the purple dashed line is the best fit. ET and MT basis functions are shown as red and blue solid lines respectively.

Cyclohexanone						
Pump wavelength (nm)	τ_1		τ_2		τ_1/τ_2	
	Amplitude	error	Amplitude	error	Amplitude	error
255	0.50	0.01	0.3	0.01	1.67	0.06
281	0.69	0.01	0.44	0.01	1.57	0.04
290	0.66	0.01	0.49	0.01	1.35	0.03
312	0.54	0.02	0.57	0.01	0.95	0.04

Table 3- 3. Amplitudes of the fastest (τ_1 = 1.0 ± 0.1 ps) and intermediate (τ_2 = 8.9 ± 0.3 ps) time components of the tri-exponential decays of ET basis function intensity observed by decomposition of TEA spectra of photoexcited cyclohexanone. Data are shown for four different UV excitation wavelengths. τ_1/τ_2 ratios show that the contribution of the fastest time constant decreases with longer excitation wavelengths.

state α-cleavage mechanism proposed to be responsible for the ≤ 1 ps ESA loss. The growth kinetics of the long-time component are well-described by a mono-exponential function with a common time constant τ_3 > 1200 ps for all excitation wavelengths. Consequently, a new species is concluded to form on timescales longer than the 1.3 ns time window for transient spectroscopy measurements.

3.3.2 Transient vibrational absorption spectra

The TEA spectra presented in the preceding section reveal the decay of excited S_1-state populations in the three cyclic ketones after UV excitation, but further valuable photochemical insights derive from TVA measurements. In particular, TVAS provides information about the photoproducts, and their formation timescales. Cyclobutanone and cyclohexanone have previously been reported to form ring-opened compounds containing a ketene functional group,[19, 21, 26, 27, 44] so TVA spectra were measured for all three cyclic ketones in the mid-IR region around 2100 cm^{-1}, using a UV pump wavelength of λ_{exc} = 281 nm.[26, 45-47] At this excitation wavelength, only the TVA spectra of cyclobutanone solutions showed a ketene band signal on timescales up to the maximum experimental delay. Figure 3-11 shows illustrative TVA spectra for cyclobutanone: a broad feature evident at early time delays is

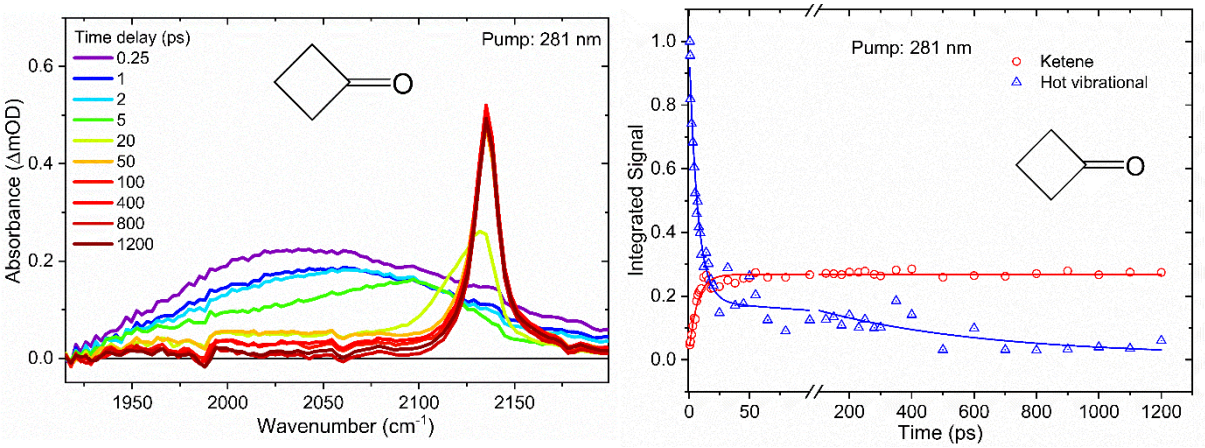

Figure 3- 11. Transient vibrational absorption spectra and kinetics obtained for a solution of cyclobutanone in cyclohexane photoexcited at λ_{exc} = 281 nm. (a) TVA spectra obtained at time delays from 0.2 – 1200 ps, as indicated by the inset colour key. (b) Decay of the hot vibrational band and the growth of ketene fundamental absorption extracted from the TVA spectra as described in the main text, and biexponential fits to the data (solid lines) with shared time constants of 7 and 550 ps.

assigned to vibrationally excited ketene photoproducts of the ring-opening pathway. Similar vibrational hot bands and spectral shifts during vibrational relaxation were observed for the ketene photoproducts of photoinduced ring opening of α-pyrone, thiophenone and furanone .[48, 49] The broad feature narrows and shifts to higher wavenumber on a timescale of ≤ 50 ps, which is a signature of vibrational cooling by loss of excess internal energy to the solvent bath. A sharp feature which develops at 2135 cm^{-1} is the fundamental band of the thermalized ketene photoproduct. The presence of the hot ketene band, even at the earliest time delays of 0.25 ps, clearly indicates an ultrafast ring-opening pathway for the S_1-state cyclobutanone molecules, which is absent in cyclopentanone and cyclohexanone at the same excitation wavelength. The subsequent relaxation kinetics of the nascent, vibrationally hot

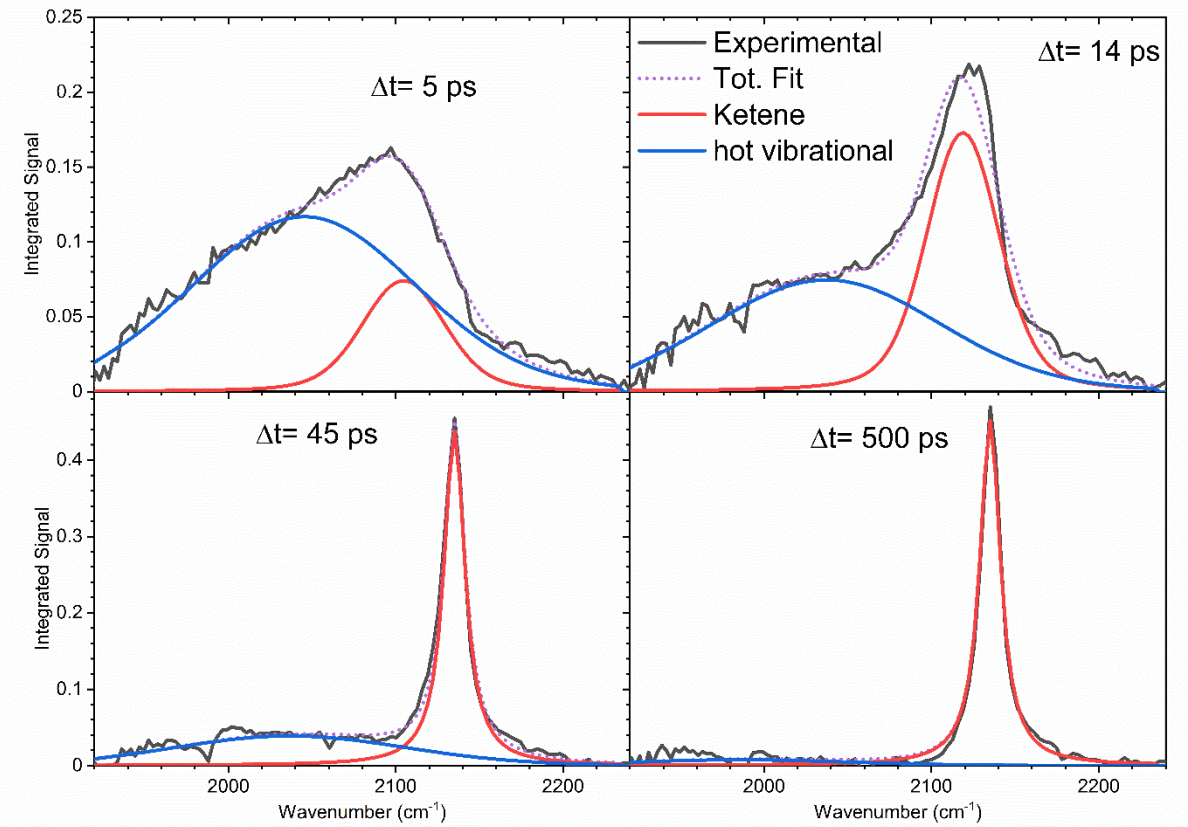

Figure 3- 12. Example of the decomposition of TVA spectra obtained in the ketene region for a UV-excited cyclobutanone solution in cyclohexane. The decomposition used a Gaussian function and a Lorentzian function with centres that shift with time. The TVA spectra were obtained at an excitation wavelength of 281 nm, and the decomposition was performed in the KOALA program. The sample spectra plotted were taken at three different time delays: (a) 5 ps, (b) 14 ps, (c) 45 ps and (d) 250 ps. In each case, the black solid line is the experimental spectrum, and the purple dashed line is the best fit. The Gaussian function (representing a broad absorption by vibrationally hot ketene molecules) and the Lorentzian function (for the vibrationally thermalized ketene peak) are shown as blue and red solid lines respectively.

photoproducts and the growth of the ketene fundamental band (obtained by the spectral decomposition method shown in Figure 3-12) can be globally fitted to biexponential functions with shared time constants of 7 ps and 550 ps. The former component dominates and is attributed to vibrational cooling of the promptly (sub-ps) formed ketene molecules. The likely mechanism for sub-ps formation of the ketene photoproducts is rapid crossing of the low S_1 barrier to access an S_1/S_0 conical intersection (see Figure 3-1), which was previously suggested as a pathway for ketene formation from non-cyclic ketones,[50] and further isomerization or fragmentation of the internally excited S_0-state molecules on timescales much faster than vibrational energy transfer to the solvent.

Figure 3-13 shows that the ketene can also be formed by photoexcitation at λ_{exc} = 255 nm and 312 nm. However, the observed ketene signals are too weak to allow a full kinetic analysis, suggesting other pathways out-compete ketene formation. The inability to observe ketene photoproduct bands following photoexcitation of either cyclopentanone or cyclohexanone under otherwise identical conditions at λ_{exc} = 255 nm, 281 nm or 312nm

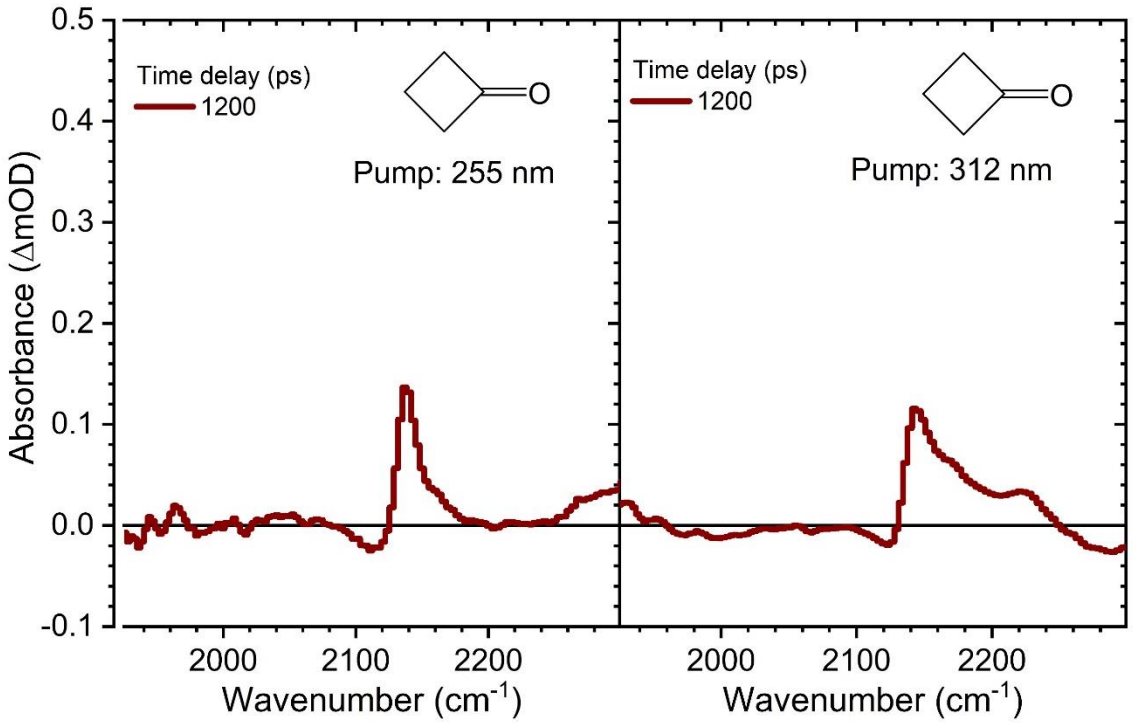

Figure 3- 13. Transient vibrational absorption spectra obtained in the ketene region for solutions of cyclobutanone in cyclohexane photoexcited at λ_{exc} = 255 nm (left panel) and λ_{exc} = 312 nm (right panel). The TVA spectra shown correspond to a pump-probe time delay of 1200 ps. The peak at ~2140 cm^{-1} is indicative of ketene photoproduct formation, but the weak bands suggest low quantum yields for this pathway at these excitation wavelengths.

suggests low quantum yields for the ketene forming channels. Instead, rival photochemical pathways must dominate following Norrish Type I α-cleavage on the S_1 state potential energy surface or, at later times, after ISC to the T_1 state. There is no evidence in any of these spectra for photochemical release of CO (with an IR band expected near 2140 cm^{-1}),[51] which was suggested to be a reaction path competing with the ketene path,[34] on the timescale of the current measurements.

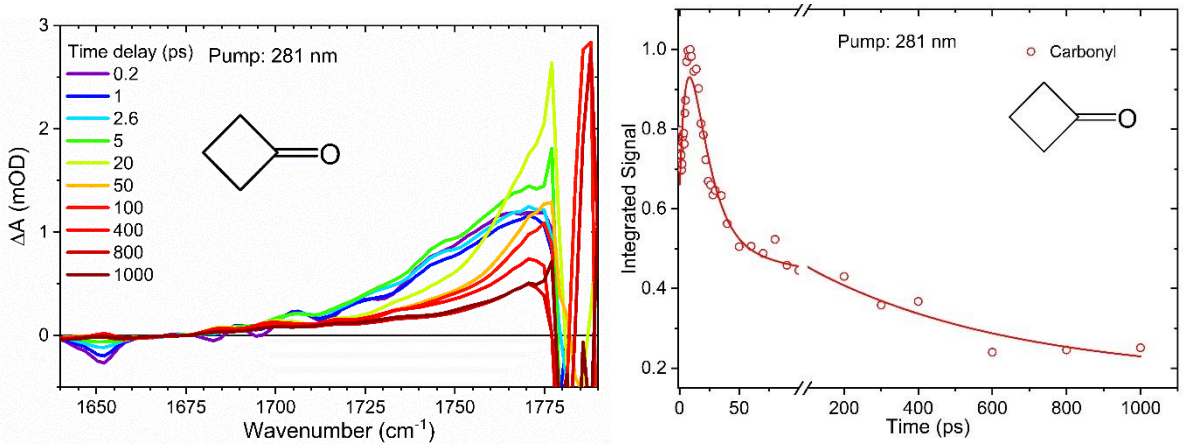

Figure 3- 14. Transient vibrational absorption spectra and decay kinetics of cyclobutanone in cyclohexane photoexcited at λ_{exc} = 281 nm. Left panel: TVA spectra obtained at time delays from 0.2 – 1200 ps, as indicated by the inset colour key. The parent molecule has a strong absorption centred at ~1780 cm^{-1}. Right panel: Time-dependence of the integrated intensity of the transient absorption by cyclobutanone, extracted from the TVA spectra by integrating spectral absorbance from 1760-1770 cm^{-1} (red circles), and a tri-exponential fit to the data (solid line).

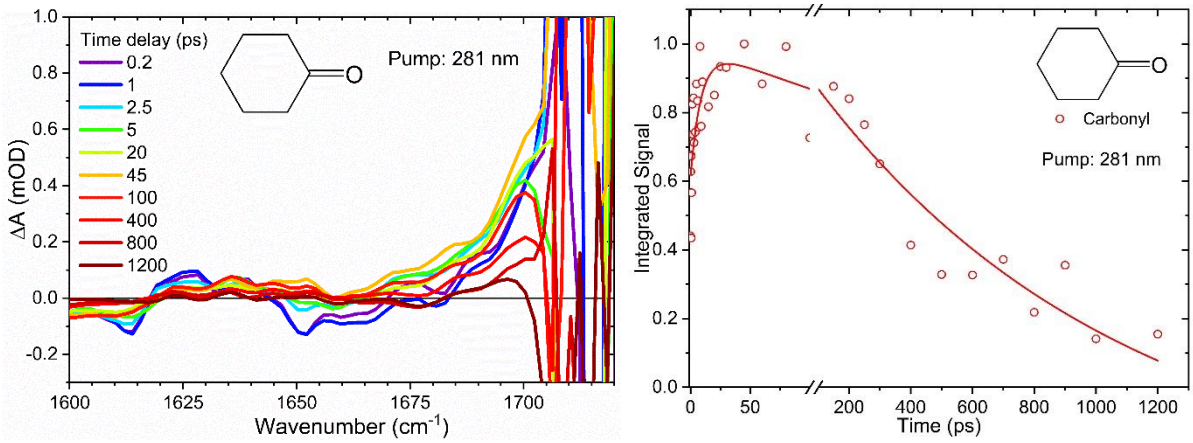

Figure 3- 15. Transient vibrational absorption spectra and decay kinetics of cyclohexanone in cyclohexane photoexcited at λ_{exc} = 281 nm. Left panel: TVA spectra obtained at time delays from 0.2 – 1200 ps, as indicated by the inset colour key. The parent molecule has a strong absorption centred at ~1710 cm^{-1}. Right panel: Time-dependence of the integrated intensity of the transient absorption by cyclohexanone, extracted from the TVA spectra by integrating spectral absorbance from 1690-1700 cm^{-1} (red circles), and a tri-exponential fit to the data (solid line).

The observation of further photoproducts of the Norrish Type-I photochemistry is hindered by the strength of the parent IR absorption bands in the carbonyl stretching region. Figures 3-14 and 3-15 show examples of TVAS data for cyclobutanone and cyclohexanone measured in this region. Tentative analysis of transient features, which are heavily overlapped by the strong ground-state parent bands, suggests relaxation times of 7 ps and 9 ps for the respective cyclic ketones. These observations are indicative of vibrational cooling but provide no additional insights.

More information was derived from TVAS measurements in the 1200 – 1400 cm^{-1} region, which showed transient IR bands corresponding to ring vibrational motions. TVA spectra of cyclobutanone in this mid-IR region are shown in Figure 3-16 and are dominated by a negative-going feature which becomes deeper with increasing time delay. Negative-going bands in TVAS indicate stimulated emission or depletion of parent ground-state population (i.e. a ground-state bleach (GSB)). Both these contributions are expected to be greatest at early time delays. The apparent growth of the negative-going feature, which is attributed to GSB on the basis of steady-state FTIR spectra of cyclobutanone in cyclohexane solutions, indicates decay of an overlapping ESA band. Decomposition of these two components, by fitting to Gaussian functions in Origin, extracted the decaying ESA contribution shown in the right panel of Figure 3-16. This decay is well described by a bi-exponential function with time constants of τ_1 = 0.6 ps and τ_2 = 7 ps taken from analysis of TEAS data (Figures 3-3 and 3-4).

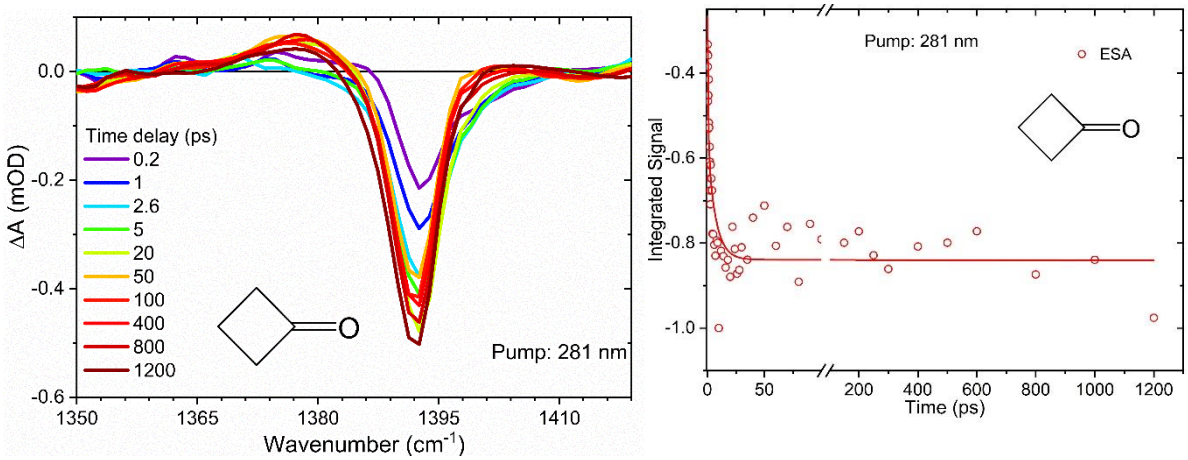

Figure 3- 16. Transient vibrational absorption spectra and decay kinetics of cyclobutanone in cyclohexane photoexcited at λ_{exc} = 281 nm. Left panel: TVA spectra obtained at time delays from 0.2 – 1200 ps, as indicated by the inset colour key. Right panel: decay of the cyclobutanone ESA, extracted from the TVA spectra as described in the main text (red circles) and a biexponential fit to the data (solid line) with time constants of 0.7 and 7 ps.

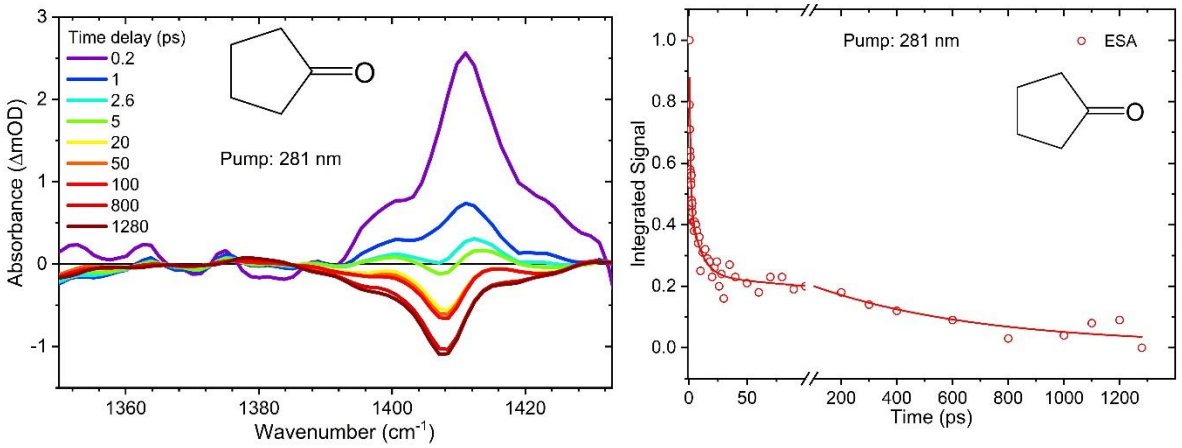

Figure 3- 17. Transient vibrational absorption spectra and decay kinetics of cyclopentanone in cyclohexane photoexcited at λ_{exc} = 281 nm. Left panel: TVA spectra obtained at time delays from 0.2 – 1280 ps, as indicated by the inset colour key. Right panel: decay of the cyclopentanone ESA, extracted from the TVA spectra as described in the main text (red circles) and a tri-exponential fit to the data (solid line) with time constants of 0.9, 9 and 600 ps.

Figure 3-17 shows example TVAS data obtained for cyclopentanone in the same spectral region. Here, the evidence for overlapping ESA and GSB contributions is more clear-cut. The GSB assignments were confirmed by comparison to steady-state FTIR measurements of cyclopentanone solutions in cyclohexane. The ESA decay kinetics can now be isolated by subtracting the GSB spectrum observed at the longest time delay from all other transient spectra (on the assumption that there is no significant population relaxation to the ring-closed and ground-state parent on the timescale of the measurements). Integrated ESA band intensities decay with increasing time delay as shown in the right panel of Figure 3-17 and are successfully modelled by a tri-exponential function with the three time constants fixed to the values τ_1 = 0.9 ps, τ_2 = 9 ps and τ_3 = 600 ps obtained from analysis of the TEA spectra. A similar analysis of TVA spectra of cyclohexanone shown in Figure 3-18 confirms ESA decay with time constants of τ_1 = 1 ps, τ_2 = 9 ps and τ_3 = 1300 ps derived from the corresponding TEAS measurements.

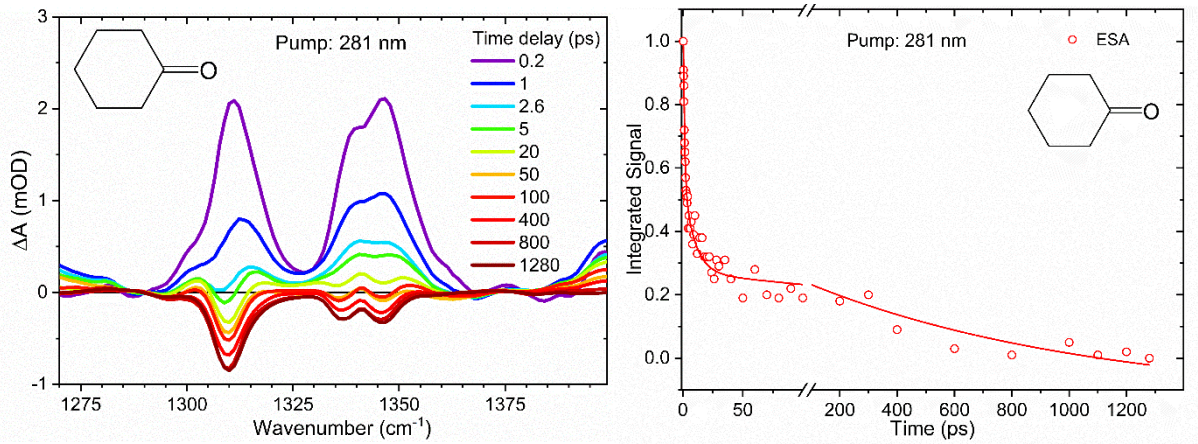

Figure 3- 18. Transient vibrational absorption spectra and decay kinetics of cyclohexanone in cyclohexane photoexcited at λ_{exc} = 281 nm. Left panel: TVA spectra obtained at time delays from 0.2 – 1200 ps, as indicated by the inset colour key. Right panel: decay of the cyclohexanone ESA, extracted from the TVA spectra as described in the main text (red circles) and a tri-exponential fit to the data (solid line) with time constants of 1, 9 and 1300 ps.

Butylketene was previously reported as a major photoproduct when gas phase cyclohexanone was exposed to 311-nm radiation for an hour,[26] but the present TVAS studies show no sign of ketene absorption following excitation at wavelengths of 281 nm or 255 nm and time delays up to 1300 ps. These shorter wavelength UV photons populate the S_1 state further above the energy barrier to C-C bond fission than at λ_{exc} = 311 nm. Hence, a greater relative yield of ring-opened photoproducts might be expected in the present experiments if dynamics on the S_1 state dominate. The TVAS observations also show no detectable ketene photoproduct bands within 1300 ps for excitation at λ_{exc} = 312 nm. When contrasted with the outcomes from the steady-state 311-nm irradiation studies, the results presented here point to butylketene formation after ISC to the parent T_1 state or isomerization of hot S_0 molecules. The former pathway is apparently too slow for the TVAS experimental measurements to observe, and the latter will be quenched in solution by vibrational energy transfer to the solvent.

3.3.3 Mechanistic interpretation of TEAS and TVAS measurements

The consistency of outcomes of the analysis of TEAS and TVAS measurements supports the following interpretation of the photochemical dynamics of the three cyclic ketones studied. In each compound, the fastest time constant ($\tau_1 \leq 1$ ps) is assigned to unimolecular reaction of the S_1-state ketone formed with excess vibrational energy by UV-photon absorption from

the ground state. The internal energies of these hot S_1 molecules lie above the barrier for α C-C bond fission on the respective S_1 state potential energy surfaces, so Norrish Type-I α-cleavage can occur promptly. The relative amplitudes of these fastest time components of the excited-state decay decline with increasing wavelength (lower photon energy), consistent with a reduction in the excess internal energy above the bond-fission barrier. These direct C-C bond breaking dynamics are most pronounced for UV-excited cyclobutanone because the C-C bond extension alleviates the C_4 ring strain as the transition state is approached, giving a smaller S_1 barrier height (~29 kJ mol^{-1} compared to ≥ 63 kJ mol^{-1} for cyclopentanone and cyclohexanone). The rapid S_1-state bond dissociation dynamics are reflected in the sub-picosecond growth of TVAS bands associated with photoproducts. In the case of cyclobutanone, one product of this photochemistry is a ketene-containing compound most likely formed via internal conversion to S_0 through an S_1/S_0 conical intersection (Figure 1),[50] but other direct photoproducts of this and the other cyclic ketones were not identified.

In competition with the ultrafast passage over the bond-fission barrier, hot S_1 molecules experience interactions with solvent molecules which deplete their excess internal energy. This pathway is not operative in photochemical studies of the isolated molecules in the gas phase at low pressure, but it plays a significant role in solution even for a weakly interacting solvent such as cyclohexane. The time constant for this vibrational cooling is 7 – 9 ps, and it is reflected in the decay of ESA signatures in TEAS measurements both by evolution of the ESA absorption band shapes, and because, as the hot S_1 molecules relax towards the minimum on the S_1 potential energy surface, their unimolecular bond-fission rates decrease. A similar time constant for vibrational cooling is observed in the relaxation of the nascent, highly internally excited ketene products of the ring-opening photochemical dynamics of cyclobutanone. IVR of internally excited S_1 molecules, placing enough energy along the reaction coordinate for passage over the S_1 C-C α-cleavage barrier, may also contribute to the 7 – 9 ps changes in the transient absorption spectra.

A third component of ESA decay occurs on timescales of 500 ps or more and is attributed to reaction of photoexcited molecules which have relaxed to energies below the S_1-state barrier for bond fission. This pathway is more evident for cyclohexanone and cyclopentanone than for cyclobutanone because of the reduction in the S_1 energy barrier height associated with release of ring strain for the latter cyclic ketone. Reaction might be through thermal activation of S_1 molecules in the room-temperature solvent, or by intersystem crossing to the

T_1 state which, for the three molecules studied, is computed to have a lower barrier to bond-breaking.[32] Build-up of T_1-state population will be limited by the rate at which it decays to S_0 by a second ISC in a region of near-degeneracy of the two potential energy surfaces at extended C-C bond distance (Figure 1). Nevertheless, the evolution of the ESA bands in cyclohexanone at longer time delays may be indicative of population of the T_1-state by ISC from S_1 because the distinct late-time spectral components grow in intensity. The likelihood of occurrence of this slower photochemical pathway increases as the photon energy decreases, consistent with the idea of competition between direct over-the-barrier reaction of internally hot molecules, and solvent induced relaxation to energies below the S_1 barrier, with only the latter route leading to T_1. Direct S_1 to S_0 internal conversion or radiative decay in the vicinity of the minimum on the S_1-state PES is likely to be slower (with ~3 ns radiative lifetime)[37] and therefore not to compete.

3.4 Conclusions

Norrish Type-I α-cleavage of cyclic ketones in cyclohexane solution is observed to occur on sub-picosecond time scales, with a propensity that depends on the UV photon energy absorbed. Competition is observed between direct bond fission over a barrier on the S_1 state potential energy surface, and slower indirect photochemical pathways favored by solvent-quenching of the excess internal energy of molecules photo-excited above the minimum energy of the S_1 state. These indirect pathways occur on timescales in excess of 500 ps for cyclobutanone, cyclopentanone and cyclohexanone, and may involve thermal reactivation above the S_1 barrier or intersystem crossing to the T_1 state and subsequent dynamics. The ring-strain in the cyclobutanone has a pronounced effect on the photochemistry, with a resulting lower barrier to C-C bond fission in the S_1 state compared to cyclopentanone or cyclohexanone which promotes direct ring-opening pathways. Observed products of the cyclobutanone photochemistry include compounds containing ketene functional groups.

References

1. R. G. W. Norrish and C. H. Bamford, *Nature*, 1936, **138**, 1016-1016.
2. N. J. Turro, N. Schore, R. Hautala, G. Farrington, M. Niemczyk, D. Morton, J. C. Dalton and K. Dawes, *Acc. Chem. Res.*, 1972, **5**, 92-101.

3. B. M. El-Zaatari, S. M. Cole, D. J. Bischoff and C. J. Kloxin, *Polym. Chem.*, 2018, **9**, 4772-4780.
4. J. Kossanyi, B. Furth and J. P. Morizur, *Tetrahedron Lett.*, 1973, 3459-3462.
5. J. C. Scaiano, P. Billone, C. M. Gonzalez, L. Maretti, M. L. Marin, K. L. McGilvray and N. Yuan, *Pure Appl. Chem.*, 2009, **81**, 635-647.
6. J. C. Scaiano, K. G. Stamplecoskie and G. L. Hallett-Tapley, *ChemComm.*, 2012, **48**, 4798-4808.
7. P. Liu, W. B. Liu and C. J. Li, *J. Am. Chem. Soc.*, 2017, **139**, 14315-14321.
8. K. Arangdad, A. Detwiler, C. D. Cleven, C. Burk, R. Shamey, M. A. Pasquinelli, H. Freeman and A. El-Shafei, *J. Appl. Polym. Sci.*, 2019, **136**, 47148.
9. S. Arumugam, D. R. Vutukuri, S. Thayumanavan and V. Ramamurthy, *J. Am. Chem. Soc.*, 2005, **127**, 13200-13206.
10. R. W. Guo, P. B. Mei, Q. Zhong, Y. Yao, Q. Su and J. H. Zhang, *RSC Adv.*, 2015, **5**, 31365-31374.
11. A. C. Jacobs, M. J. E. Resendiz and M. M. Greenberg, *J. Am. Chem. Soc.*, 2011, **133**, 5152-5159.
12. J. Jakubiak, M. Nowakowska and X. Coqueret, *Bull. Pol. Acad. Sci.*, 1997, **45**, 71-77.
13. O. Muraoka, M. Okumura, T. Maeda, L. C. Wang and G. Tanabe, *Chem. Pharm. Bull.*, 1995, **43**, 517-519.
14. H. B. Singh, D. Ohara, D. Herlth, W. Sachse, D. R. Blake, J. D. Bradshaw, M. Kanakidou and P. J. Crutzen, *J. Geophys. Res. Atmos.*, 1994, **99**, 1805-1819.
15. A. Chattopadhyay, K. Mondal, M. Samanta and T. Chakraborty, *Atmos. Environ.*, 2017, **157**, 125-134.
16. F. Domine and P. B. Shepson, *Science*, 2002, **297**, 1506-1510.
17. J. E. Scott, *Analyst*, 1977, **102**, 614-618.
18. H. B. Singh, M. Kanakidou, P. J. Crutzen and D. J. Jacob, *Nature*, 1995, **378**, 50-54.
19. H. O. Denschlag and E. K. C. Lee, *J. Am. Chem. Soc.*, 1967, **89**, 4795-4797.
20. N. E. Lee and E. K. C. Lee, *J. Chem. Phys.*, 1969, **50**, 2094-2107.
21. N. J. Turro and R. M. Southam, *Tetrahedron Lett.*, 1967, **8**, 545-551.
22. S. W. Benson and G. B. Kistiakowsky, *J. Am. Chem. Soc.*, 1942, **64**, 80-86.
23. C. H. Bamford and R. G. W. Norrish, *J. Chem. Soc.*, 1938, 1521- 1531.
24. R. G. Shortridge and E. K. C. Lee, *J. Am. Chem. Soc.*, 1970, **92**, 2228-2236.
25. R. Srinivasan and S. E. Cremer, *J. Am. Chem. Soc.*, 1965, **87**, 1647-1651.
26. A. Chattopadhyay, K. Mondal, M. Samanta and T. Chakraborty, *Chem. Phys. Lett.*, 2017, **675**, 104-110.
27. M. D. Hoops and B. S. Ault, *J. Mol. Struct.*, 2009, **929**, 22-31.
28. D. Shemesh, S. A. Nizkorodov and R. B. Gerber, *J. Phys. Chem. A.*, 2016, **120**, 7112-7120.
29. P. Dunion and C. N. Turmbore, *J. Am. Chem. Soc.*, 1965, **87**, 4211-4212.
30. J. W. Ochterski, G. A. Petersson and J. A. Montgomery, *J. Chem. Phys.*, 1996, **104**, 2598-2619.
31. R. D. Bach and O. Dmitrenko, *J. Am. Chem. Soc.*, 2006, **128**, 4598-4611.
32. S. H. Xia, X. Y. Liu, Q. Fang and G. L. Cui, *J. Phys. Chem. A*, 2015, **119**, 3569-3576.
33. J. C. Hemminger and E. K. C. Lee, *J. Chem. Phys.*, 1972, **56**, 5284-5295.
34. K. Y. Tang and E. K. C. Lee, *J. Phys. Chem.*, 1976, **80**, 1833-1836.
35. J. C. Hemminger, C. F. Rusbult and E. K. C. Lee, *J. Am. Chem. Soc.*, 1971, **93**, 1867-1871.
36. M. O'Sullivan and A. C. Testa, *J. Chem. Phys.*, 1973, **77**, 1830-1833.

37. R. G. Shortridge, C. F. Rusbult and E. K. C. Lee, *J. Am. Chem. Soc.*, 1971, **93**, 1863-1867.
38. E. W. G. Diau, C. Kotting and A. H. Zewail, *Chemphyschem*, 2001, **2**, 294-309.
39. D. A. Hansen and E. K. C. Lee, *J. Chem. Phys.*, 1975, **62**, 183-189.
40. S. A. Kovalenko, R. Schanz, H. Hennig and N. P. Ernsting, *J. Chem. Phys.*, 2001, **115**, 3256-3273.
41. T. Elsaesser and W. Kaiser, *Annu. Rev. Phys. Chem.*, 1991, **42**, 83-107.
42. M. Baba and I. Hanazaki, *J. Chem. Phys.*, 1984, **81**, 5426-5433.
43. M. P. Grubb, A. J. Orr-Ewing and M. N. R. Ashfold, *Rev. Sci. Instrum.*, 2014, **85**, 064104.
44. F. E. Blacet and A. Miller, *J. Am. Chem. Soc.*, 1957, **79**, 4327-4329.
45. N. Y. Dugarte, M. F. Erben, R. M. Romano, R. Boese, M. F. Ge, Y. Li and C. O. Della Vedova, *J. Phys. Chem. A*, 2009, **113**, 3662-3672.
46. N. Y. Dugarte, M. F. Erben, R. M. Romano, M. F. Ge, Y. Li and C. O. Della Vedova, *J. Phys. Chem. A*, 2010, **114**, 9462-9470.
47. C. D. Hatten, K. R. Kaskey, B. J. Warner, E. M. Wright and L. R. McCunn, *J. Chem. Phys.*, 2013, **139**, 214303.
48. D. Murdock, R. A. Ingle, I. V. Sazanovich, I. P. Clark, Y. Harabuchi, T. Taketsugu, S. Maeda, A. J. Orr-Ewing and M. N. R. Ashfold, *Phys. Chem. Chem. Phys.*, 2016, **18**, 2629-2638.
49. D. Murdock, S. J. Harris, J. Luke, M. P. Grubb, A. J. Orr-Ewing and M. N. R. Ashfold, *Phys. Chem. Chem. Phys.*, 2014, **16**, 21271-21279.
50. B. Marchetti, T. N. V. Karsili and M. N. R. Ashfold, *Phys. Chem. Chem. Phys.*, 2019, **21**, 14418-14428.
51. G. E. Ewing, *J. Chem .Phys.*, 1962, **37**, 2250-2256.

Chapter 4. Influence of the solvent environment on the ultrafast relaxation pathways of a sunscreen molecule, diethylamino hydroxybenzoyl hexyl benzoate

This chapter is adapted from the work published in *Min-Hsien Kao, Ravi Kumar Venkatraman, Mahima Sneha, Matthew Wilton, and Andrew J. Orr-Ewing, J. Phys. Chem. A 2021,* ***125****, 2, 636–645.* The author of this thesis contributed the design of experiments, data collection, data analysis, and interpretation.

4.1 Introduction

UV light from the sun is commonly divided into three wavelength regions: UVA (400-320 nm), UVB (320-280 nm) and UVC (280-100 nm), of which UVA accounts for more than 90% of UV radiation reaching the surface of the Earth.[1] This UVA can penetrate human skin to the dermis layer.[2] Although DNA mainly absorbs UVB radiation, UVA absorption encourages formation of reactive oxygen species that can cause DNA damage and increase the occurrence of skin cancers.[3-6] The application of UVA absorbers to the skin inhibits the generation of these reactive oxygen species and reduces oxidative stress in cultured human dermal fibroblasts exposed to UVA.[3, 7]

Diethylamino hydroxybenzoyl hexyl benzoate (DHHB), with the structure shown in Figure 4-1, is a UVA absorber widely approved for use in sunscreens in Japan, Europe, Australia and South Africa with commercial name Uvinul A .[8, 9] Previous studies of DHHB focused on its photostability in formulations with other sunscreen molecules such as tert-butyl-methoxydibenzoylmethane and avobenzone.[10-12] DHHB has a similar core structure to oxybenzone (see Figure 4-1c), which is an efficient UVB absorber but toxic to coral and now a banned ingredient of sunscreen products in Hawaii.[13, 14] Prior ultrafast spectroscopy studies have established that the relaxation mechanism of photoexcited oxybenzone is via enol $\rightarrow$ keto tautomerization.[15] After UV excitation of the ground-state enol form to the S_2 state, oxybenzone undergoes excited state hydrogen transfer (ESHT) to reach the S_1-keto form on a time scale estimated to be ~100 fs.[15, 16]

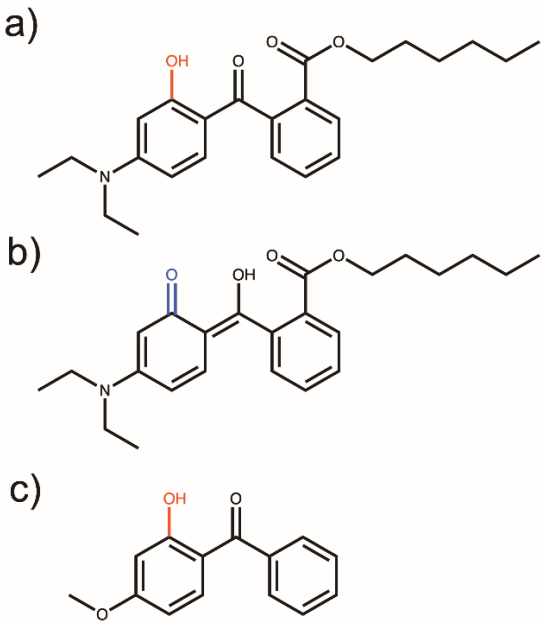

Figure 4- 1. Molecular structures of: (a) DHHB in its enol form; (b) DHHB in its keto form; (c) oxybenzone.

Following ESHT, the keto form of oxybenzone experiences a central C-C bond torsion with a time constant of around 400 fs. The twisted keto S_1 state molecules access a conical intersection (CI) which provides an efficient relaxation pathway to the ground electronic state. In oxybenzone, this ground-state recovery takes ~8 ps and there is a small yield of an isomer, the trans-keto form, which relaxes back more slowly to the lowest-energy form.[15-17] In addition, after photoexcitation to the singlet excited state, a minor pathway involving formation of the phenoxy radical of oxybenzone by homolytic H-O bond cleavage was reported on longer timescales.[18]

DHHB differs from oxybenzone by the presence of an auxochrome amino group meta to the -OH group on one phenyl ring. The amino group shifts the main $\pi^* \leftarrow \pi$ absorption band by 15 nm to longer wavelength than for oxybenzone in cyclohexane solution. This $\pi^* \leftarrow \pi$ absorption band of DHHB is sensitive to the solvent polarity, undergoing a bathochromic shift as can be seen in Figure 4-2 in Section 4.3. The presence of an additional auxochrome, the ester group of DHHB connected to the other aromatic ring, facilitates charge separation in the first excited singlet state, and thereby modifies the photochemistry in ways that are explored here. A simpler molecular analogue of both DHHB and oxybenzone, 2-hydroxy-benzophenone, has been reported to have different photophysical properties in ethanol and hexane, and a long-lived absorption signal in ethanol was assigned to triplet state photoproducts.[19] The

photochemical properties of DHHB have also been shown to depend on the solvent. In ethanol, DHHB is phosphorescent at 77 K, but in non-polar solvents it does not phosphoresce, suggesting that the intramolecular hydrogen bond between the OH and carbonyl groups, which is expected to be sensitive to the solvent environment, plays an important role in the relaxation of photoexcited DHHB.[20]

Formation of triplet species is undesirable for sunscreen molecule since they can be quenched by O_2 to form singlet oxygen which is a reactive oxygen species.[21, 22] In addition, triplet-triplet energy transfer between UVA and UVB absorbers has been reported to reduce the efficiency of sunscreen products.[23, 24] DHHB has a similar triplet state energy to both octocrylene and octyl methoxycinnamate sunscreen additives, so triplet DHHB may be quenched by these compounds,[20, 25] but with potential consequences for the effectiveness of these UVB filters.

The ultrafast transient electronic and vibrational absorption spectroscopy (TEAS and TVAS) studies reported here compare the photochemical properties of DHHB and its primary relaxation pathways in four solvents, cyclohexane (CYCH), methanol (MeOH), acetonitrile (ACN), and dimethyl sulfoxide (DMSO). Competition is identified in the UV-excited S_1 state between torsional motion in the enol form towards an $S_1 – S_0$ conical intersection, ESHT from the enol to keto forms, and intersystem crossing to the triplet manifold of states, with solvent-dependent outcomes. Relaxation mechanisms of photoexcited DHHB are proposed, the associated time constants are reported, and the outcomes are contrasted with the relaxation pathway for the structurally similar oxybenzone. Evidence is presented for a minor photochemical role for triplet-state DHHB.

4.2 Experimental and computational methods

Acetonitrile (Fisher, HPLC grade, ≥ 99.9%), cyclohexane (Acros, for spectroscopy, > 99%), dimethyl sulfoxide (Merck, Uvasol for spectroscopy) and methanol (Sigma-Aldrich, HPLC grade, ≥ 99.9%) were used to prepare 25 mM stock solutions of diethylamino hydroxybenzoyl hexyl benzoate (BASF Uvinul A Plus, 99.7%). Octocrylene (Supelco, Pharmaceutical Secondary Standard) or trans-β-methyl styrene (Sigma-Aldrich, 99%) were added to some of the prepared DHHB solution samples to test triplet-triplet energy transfer pathways. All the chemicals were used without further purification.

Samples used for steady state and transient absorption spectroscopy studies were prepared from the stock DHHB solutions, by dilution if required. Absorption spectroscopy measurements were performed using a stainless-steel Harrick cell fitted with two 1.5-mm thick CaF_2 windows separated by 100-μm polytetrafluoroethylene (PTFE) spacers. Steady state UV-visible spectra of 2.5 mM solutions were measured by a GENESYS 10S UV-Vis Spectrophotometer (Thermo Scientific). The IR absorption spectra of 25 mM DHHB solutions were obtained using a Spectrum Two FTIR Spectrometer (PerkinElmer). Fluorescence emission spectroscopy of 25 μM DHHB solutions instead used a 1 cm-pathlength quartz cuvette placed into a fluorimeter (PerkinElmer LS 45) with slits set at 10 nm wavelength resolution.

The ultrafast laser system and associated spectrometers and optical paths used for TEAS and TVAS measurements have been described in detail in previous publications and Chapter 2.[26, 27] 2.5 mM DHHB solutions were continuously circulated from a reservoir to a stainless steel Harrick cell fitted with CaF_2 windows separated by 100 μm. The reservoir and cell were connected by PTFE tubing, and circulation was maintained by a peristaltic pump. The near-UV excitation wavelength was set at λ_{ex} = 360 nm for DHHB solutions in polar solvents, and at λ_{ex} = 345 nm for solutions in CYCH, corresponding to wavelengths close to the absorption maxima of the long-wavelength bands of DHHB in these solvents. The excitation was increased to 375 nm for studies of triplet quenching with octocrylene to minimize overlap with the red edge of the octocrylene absorption band. The wavelength region covered by the white-light continuum TEAS probe beam was from 330 nm to 700 nm, and the mid-IR TVAS probe spanned 1550 - 1800 cm^{-1} to monitor the carbonyl stretching region. Instrument responses were ~120 fs for TEAS and 150 fs for TVAS as determined by cross-correlation.[26] The possible degradation of the DHHB sample, and hence accumulation of photoproducts during measurements, was monitored by recording the UV-visible absorption spectrum of the solution before and after the time-resolved experiments. Any loss of DHHB absorption was always observed to be less than 2%.

The functionals and basis sets chosen for all the calculations of vibrational frequencies, excited state energies and structures reported here were described in Chapter2.

4.3 Results and discussion

4.3.1 DHHB structures in the ground and excited electronic states

Figure 4-1 shows the two tautomeric forms of DHHB. According to the calculations here, the enol form is significantly more stable than the keto form in the ground (S_0) electronic state, and the calculations suggest a barrierless process to go from the keto to the enol form (Figure 4-2). Therefore, for all the experiments conducted here, excitation is assumed to be from DHHB (S_0) in its enol form.

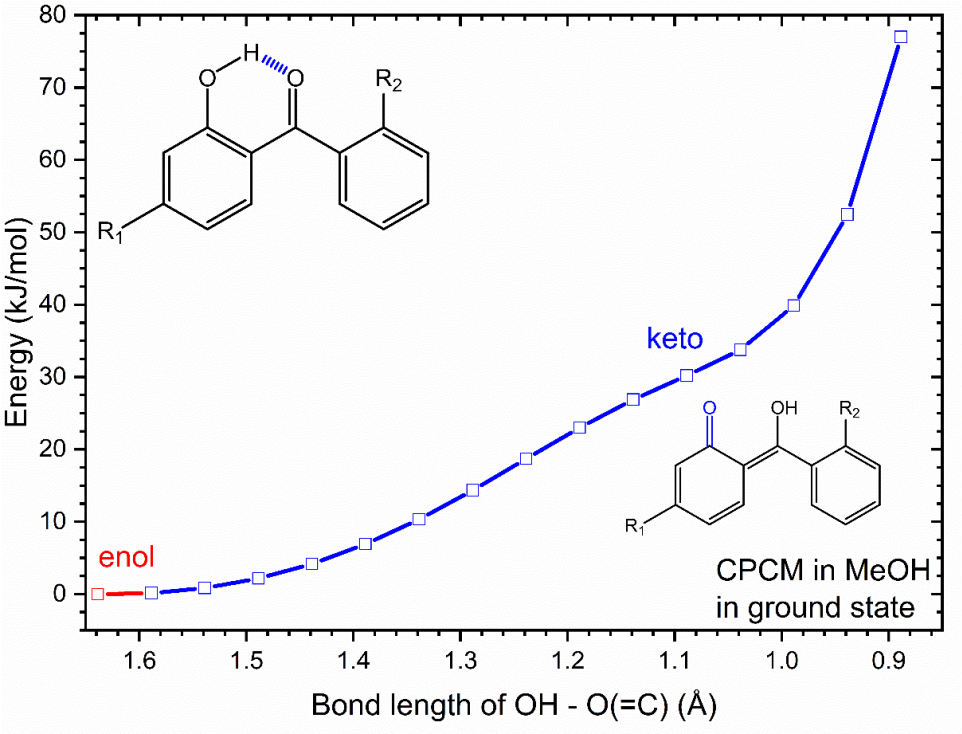

Figure 4- 2. Calculated relaxed scan for DHHB along the distance between the hydrogen of the hydroxyl group and the oxygen of the carbonyl group, shown as a blue-hashed bond. On the left is the optimized enol form in the ground state (S_0), and to the right is the S_0 keto form. Calculations were performed for a MeOH solution. There is no energy barrier to pass from the keto to the enol tautomer in the S_0 state.

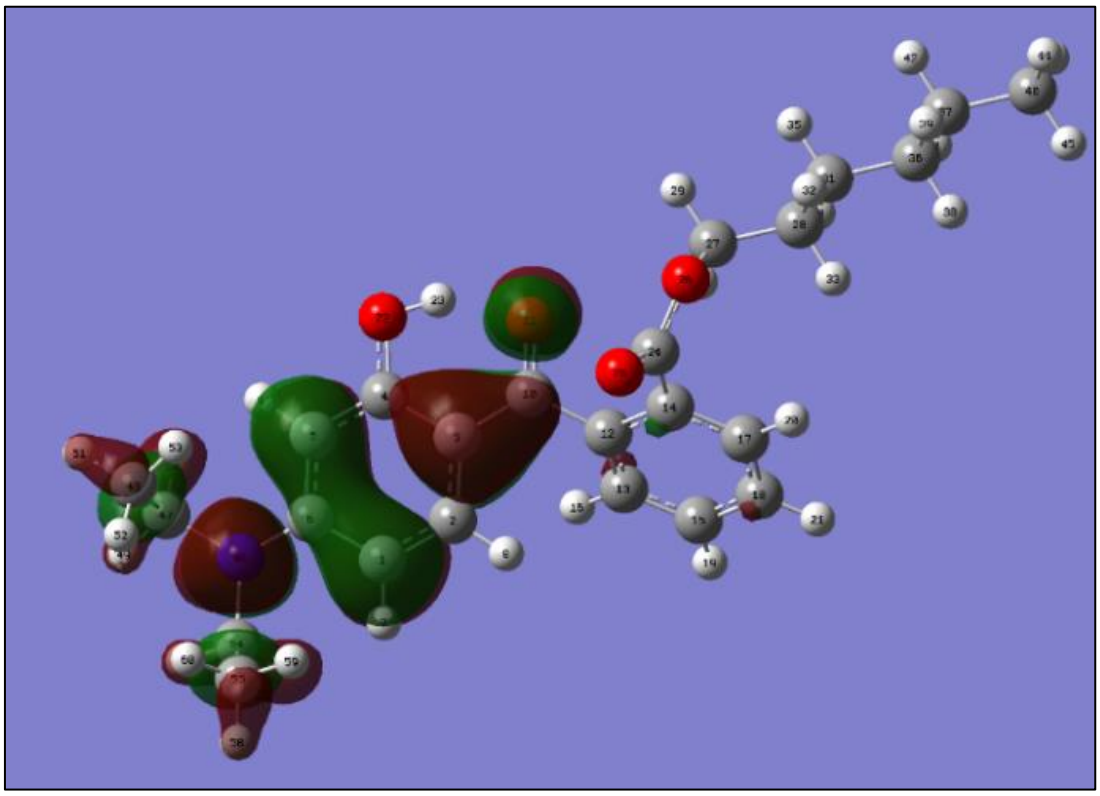

Figure 4- 3. DHHB in the ground electronic (S_0) state. The HOMO is shown by red/green shading. Note the near-planarity of the carbonyl and phenyl groups, and the out-of-plane twist of the second aromatic ring (by ~47°). The dihedral angle for (HO)C-C-C=O is 7.2°. The calculations used the DFT/TD-DFT B3LYP 6-31G** method with CPCM treatment of the methanol solvent.

The optimized S_0 structure from the calculations is shown in Figure 4-3 of, and is close to planar in the region of the central carbonyl group and the phenolic ring, but with an out-of-plane twist (by ~47°) of the second aromatic ring to reduce steric repulsions. The experimental and computational UV-Vis absorption spectra of DHHB are shown in Figure 4-4. UV excitation of DHHB near the maximum of the first absorption band, with λ_{ex} = 360 nm (or 345 nm in CYCH) corresponds to an $S_0 \rightarrow S_1$ transition, and the transient spectroscopy studies reported here therefore do not involve dynamics in higher lying electronically excited states. This first electronic transition consists of a HOMO to LUMO $\pi^* \leftarrow \pi$ electronic excitation as determined by the molecular orbital calculations reported here, and the shift to longer wavelength in more polar solvents is typical for this type of transition.[28-30]

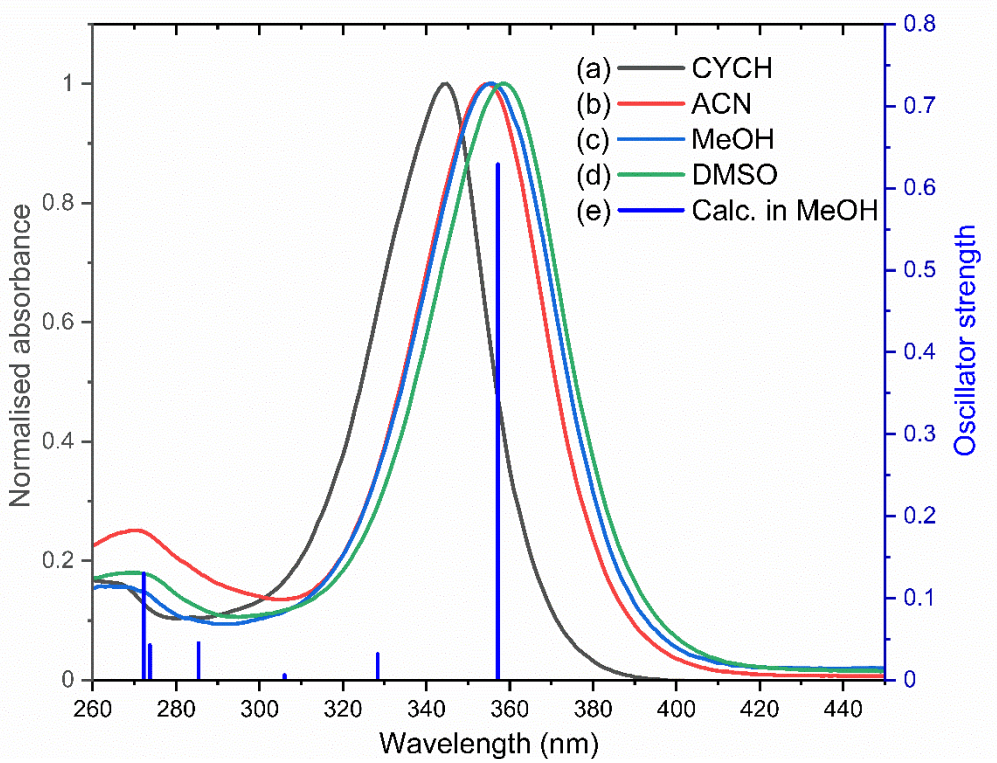

Figure 4- 4. Steady state UV-Vis absorption spectra of DHHB in (a) cyclohexane (CYCH) (b) acetonitrile (ACN), (c) methanol (MeOH), (d) dimethyl sulfoxide (DMSO). The calculated UV-Vis absorption of DHHB in methanol is shown by blue vertical bars (e). The strong absorption at 357 nm is a $\pi^* \leftarrow \pi$ orbital excitation, with the weaker band at 328 nm corresponding to another $\pi^* \leftarrow \pi$ excitation. In cyclohexane, the $\pi^* \leftarrow \pi$ excitation is computed to arise at 351 nm and is a HOMO $\rightarrow$ LUMO transition, with the excitation at 328 nm being of HOMO-1 $\rightarrow$ LUMO character. At the chosen laser excitation wavelengths, the HOMO $\rightarrow$ LUMO $\pi^* \leftarrow \pi$ orbital excitations dominate in all the chosen solvents.

Vertical excitation initially populates the S_1 state in an enol geometry (henceforth S_1-enol) in the Franck-Condon (FC) region with coplanar central carbonyl and hydroxyl groups. As Figure 4-5 shows, the optimized geometry of the S_1 enol is computed to have a twisted structure in which rotation about a central C-C bond brings the two phenyl rings to an almost perpendicular orientation. In this structure, the C(OH)-C-C=O dihedral angle is 67°. The excited MO in the optimized S_1 enol geometry is located mostly on the phenyl ring with the pendent ester group, corresponding to charge transfer (CT) character for this region of the S_1-enol PES (Figure 4-5). This CT-character in the twisted S_1 enol will be stabilized by polar solvents.

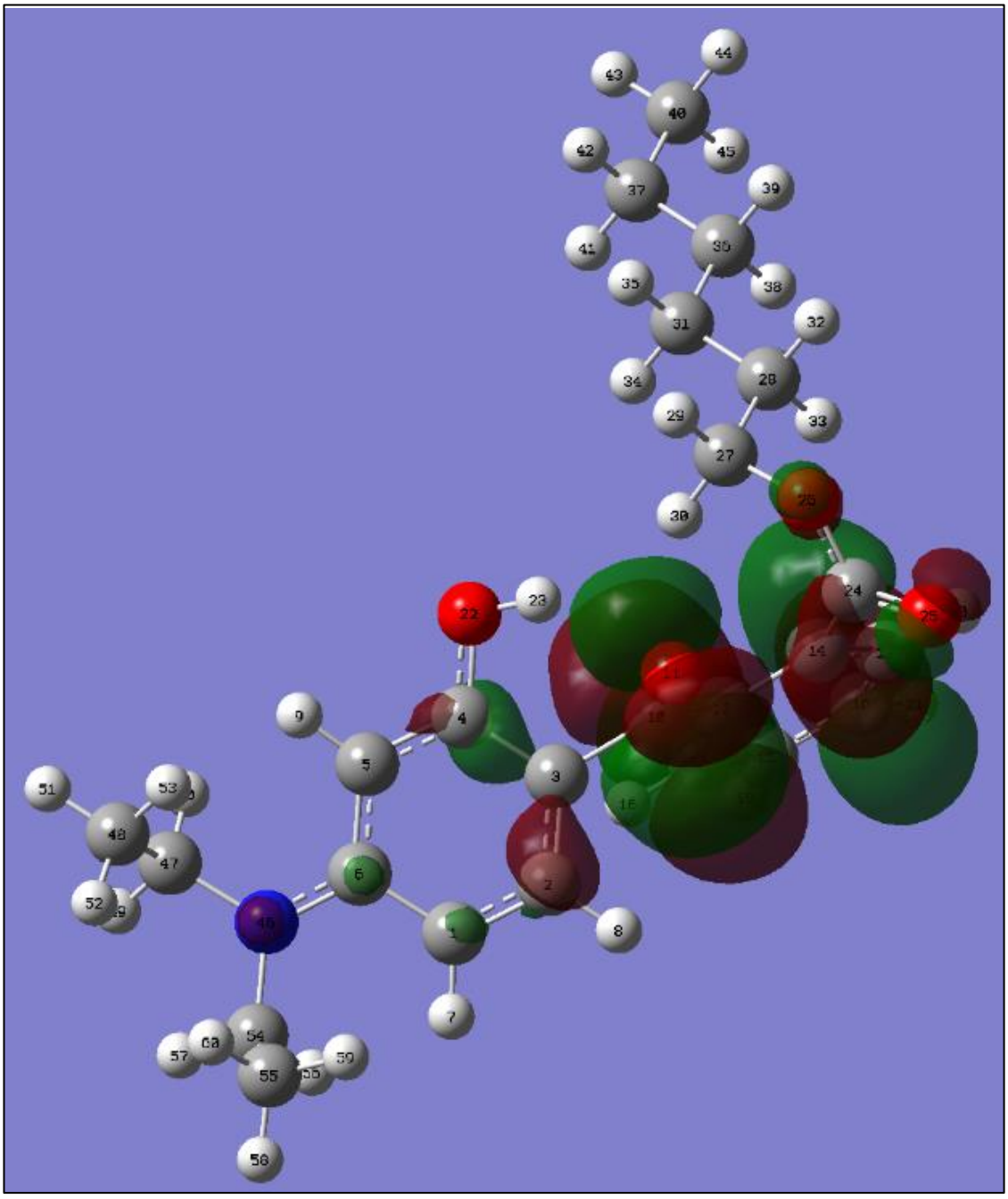

Figure 4- 5. The DHHB enol form in the S_1 state. The excited MO is shown by red/green shading. The carbonyl group located between the two benzene rings is no longer in the same plane as the hydroxyl group, with a dihedral angle for (HO)C-C-C=O of 67°, and the two phenyl rings are oriented almost perpendicular to one-another. The central carbonyl group is in the plane of the aromatic ring with an ester group. The MO shows charge transfer character compared with the ground state HOMO in Figure 4-3. The calculations used the TD-DFT B3LYP 6-31G** method with CPCM treatment of the methanol solvent.

In the vertical excitation region (for the heavy atoms), the S_1-keto form of DHHB, resulting from excited state hydrogen transfer (ESHT), is computed here to lie lower in energy in

methanol than the corresponding S_1-enol structure, and the optimized geometry is shown in Figure 4-6.

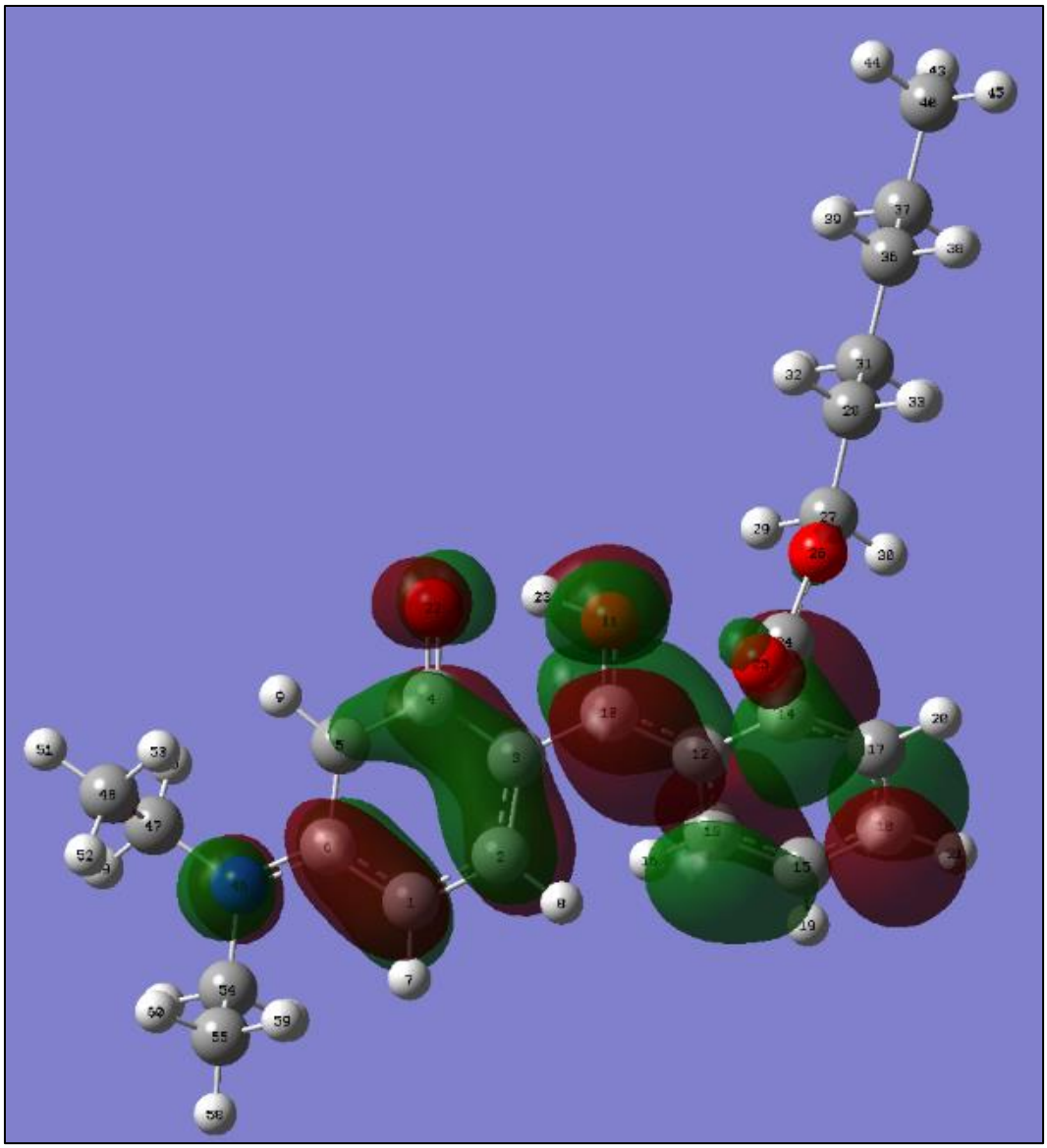

Figure 4- 6. The DHHB keto form in its S_1 state. The excited MO is shown by red/green shading. The carbonyl group is nearly in the same plane as the central hydroxyl group with a dihedral angle for (O=)C-C-C-OH of 18°. The out-of-plane twist of the second aromatic ring is ~40°. The calculations used the TD-DFT B3LYP 6-31G** method with CPCM treatment of the methanol solvent.

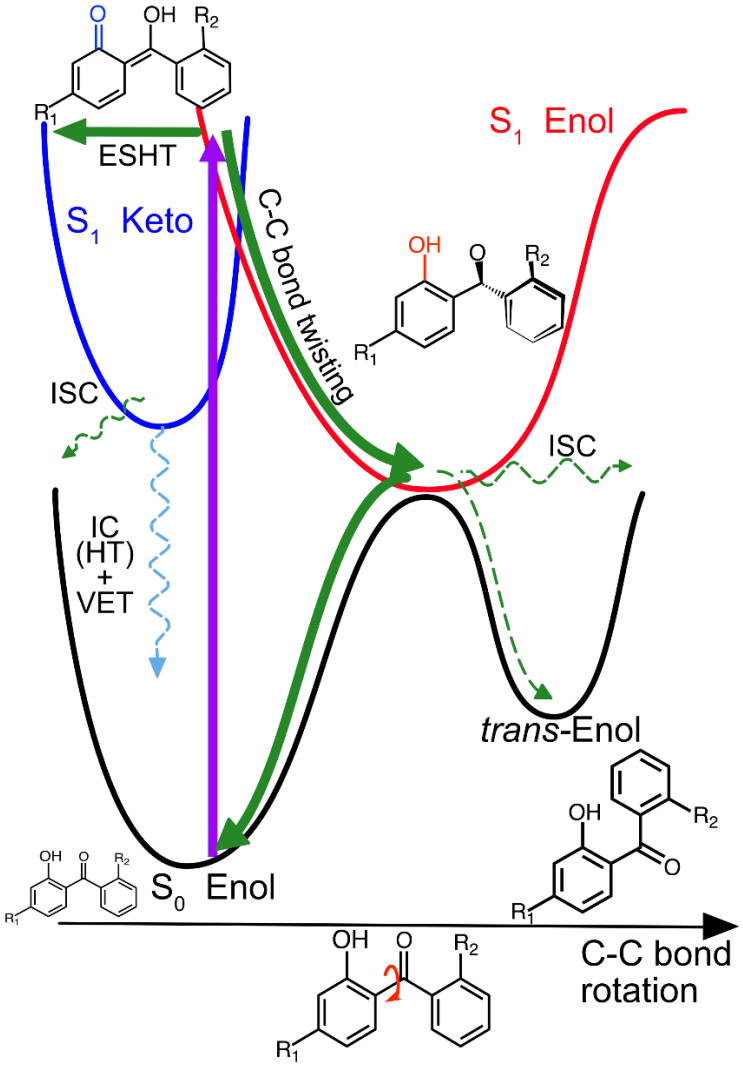

Figure 4- 7. Illustrative PESs along the C-C bond rotation coordinate and significant photochemical pathways of DHHB. After vertical excitation from the S_0-enol state to the S_1-enol state, there is competition between ESHT to the S_1-keto form and relaxation on the S_1 PES to the lower energy twisted S_1-enol structure. The majority of photoexcited molecules relax to the ground state, and only a small fraction undergoes intersystem crossing (ISC) to populate triplet states, or forms an isomeric photoproduct denoted as *trans*-enol in the S_0 state. The S_1-keto tautomer may relax to the ground state via direct internal conversion (IC) and vibrational energy transfer (VET), or via reverse ESHT to the S_1-enol form.

The dynamics from the FC region of the initially excited S_1-enol molecules are therefore expected to be either ESHT to the keto form or torsion about a central C-C bond to reach the lower energy region of the twisted S_1-enol form. This model for evolution of the excited state structures is summarized schematically in Figure 4-7 and forms the basis for the interpretation of transient absorption spectroscopy data reported here. These measurements provide evidence for competing ESHT and torsional dynamical pathways in the S_1 excited state,

quantify time constants for the pathways, and show how the competition is affected by different types of interactions with the surrounding solvent.

4.3.2 Transient electronic absorption spectroscopy of DHHB

Solvent-Dependent Photodynamics: Figure 4-8 shows TEA spectra of DHHB in four different solvents. In spectra obtained at delays of up to a few picoseconds, strong negative signals at wavelengths around 500 nm for solutions in polar solvents are assigned as stimulated emissions (SE), but the corresponding SE for DHHB in CYCH is weak. These observations are consistent with the steady state fluorescence spectra shown in Figure 4-9; these spectra show no discernable fluorescence from DHHB in CYCH under conditions in which weak fluorescence emission is detected from solutions in methanol, acetonitrile and, most prominently, DMSO.

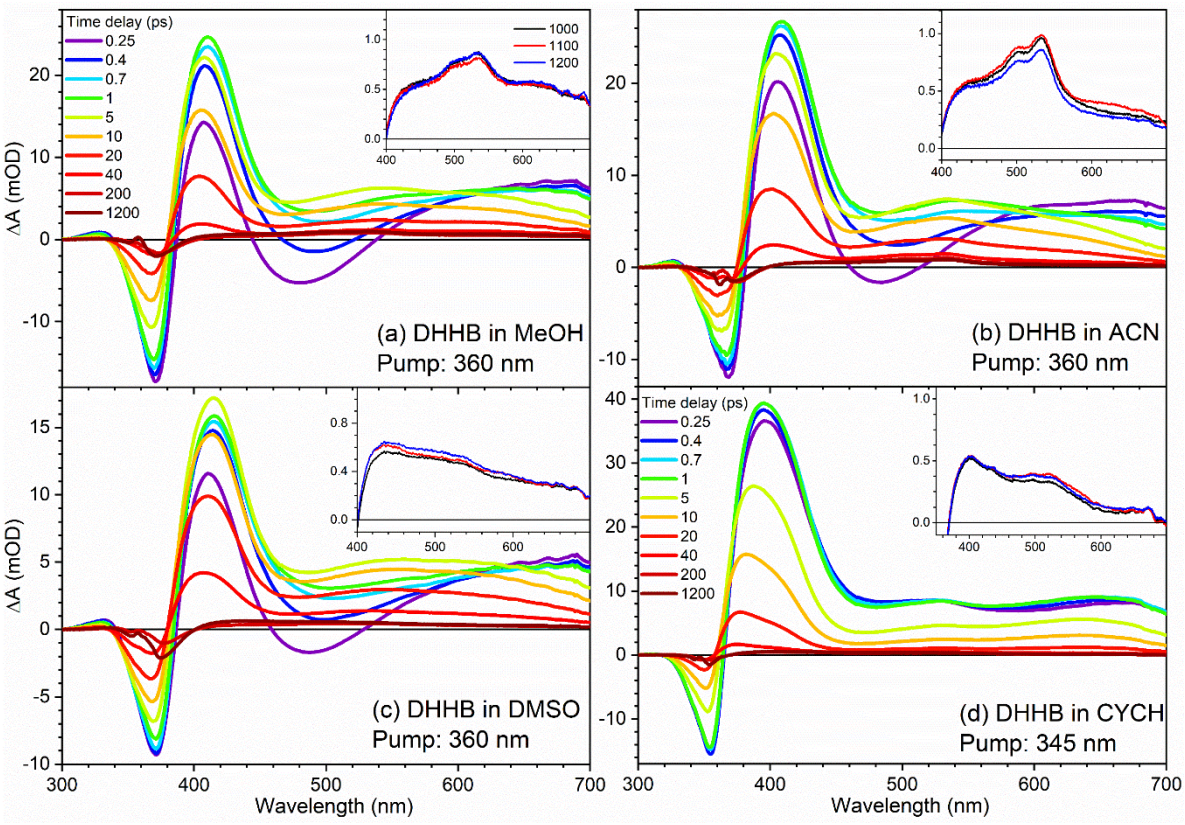

Figure 4- 8. Transient electronic absorption spectra of DHHB in (a) methanol, (b) acetonitrile, (c) dimethyl sulfoxide and (d) cyclohexane. A colour key for the time delays corresponding to different spectra is shown in panel (a). The late time spectra are shown on an expanded scale as insets in each panel.

The late-time TEA spectra, the long-wavelength regions of which are shown as insets in each panel, indicate further differences between DHHB photochemistry in the non-polar solvent and polar solvents, and will be discussed later. SE at sub-ps to few-ps delay times is likely to

derive from the photoexcited DHHB in the S_1-state FC region, and its decay is a measure of the onset of excited state dynamics. These dynamics might involve either S_1 keto formation by ESHT or structural relaxation to the twisted S_1 enol (Figures 4-7) with loss of excess vibrational energy to the solvent. Both pathways change the geometry of the excited-state DHHB and its electronic character, and hence are expected to quench the SE, but the surrounding solvent environment affects their time scales and changes the balance of competition.

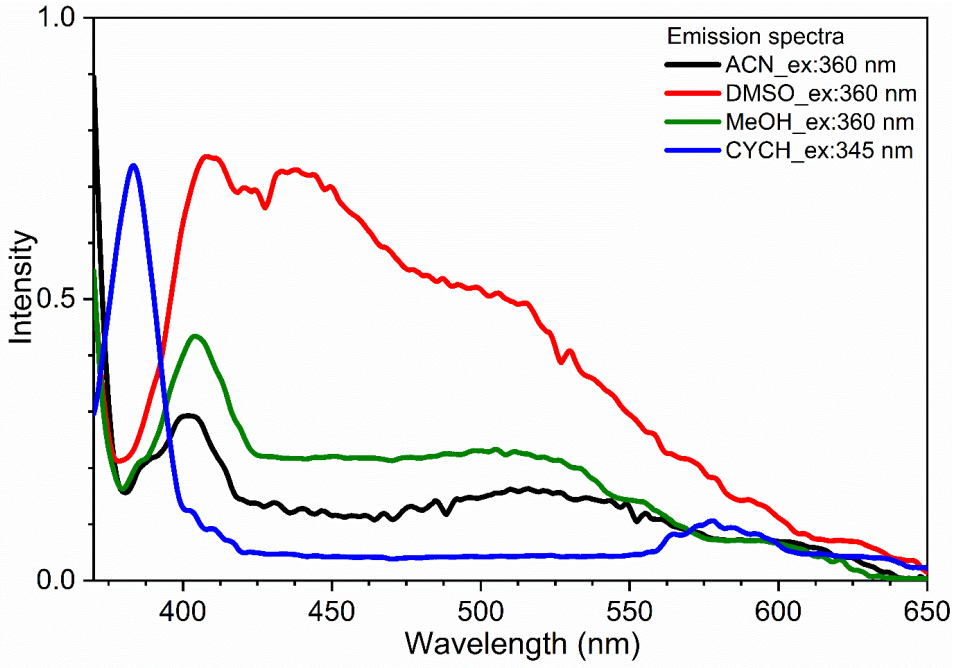

Figure 4- 9. Steady state fluorescence emission spectra of DHHB in acetonitrile (black line), dimethyl sulfoxide (red line), methanol (green line) and cyclohexane (blue line). The excitation wavelength in the polar solvents is set at 360 nm, and in cyclohexane at 345 nm. The bands at ~405 nm in the polar solvents and at ~390 nm in cyclohexane are attributed to Raman scattering associated with C-H stretching vibrations.[31, 32]

The intensity of the observed SE bands appears to relate to the hydrogen bonding ability of the chosen solvent. The strongest DHHB SE feature is seen in solution in MeOH, which can act as both a hydrogen bond donor and acceptor, whereas ACN and DMSO, in which the SE bands are somewhat less pronounced, are poorer hydrogen bond acceptors.[33] In CYCH, which does not form conventional hydrogen bonds, signatures of SE are barely evident. The prominence of the SE feature is therefore proposed to be evidence for disruption by H-bonding solvents of the ESHT mechanism for S_1 enol to S_1 keto conversion in the initially excited FC region. In CYCH solution, the solvent does not interfere with this pathway, and we propose that the SE from the photoexcited S_1-enol form (as well as steady state fluorescence) is rapidly quenched by ESHT. Figure 4-10 shows relaxed scans of the computed potential energy changes from the optimized S_1-keto to the FC region S_1-enol form, performed using CPCM treatments of MeOH

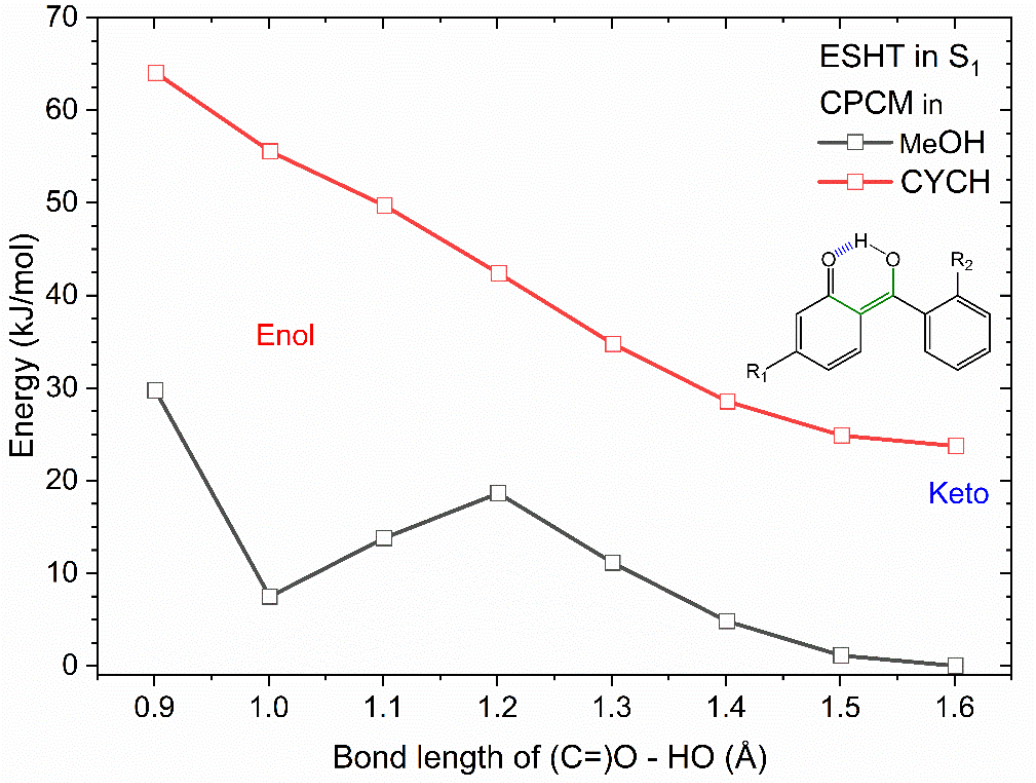

Figure 4- 10. Calculated relaxed scans along the distance between the hydrogen of the hydroxyl group and the oxygen of the carbonyl group, shown as a blue-hashed bond, with CPCM treatment of the solvent in methanol (black) and cyclohexane (red). On the right is the optimized keto form in S_1, and to the left is the S_1-enol form in the Frank Condon (FC) region. The dihedral angle involving the central C-C bond is fixed to force the enol forms to stay in the FC region and to avoid C-C bond twisting to the relaxed S_1 enol. There is no energy barrier to pass from the FC region enol to the keto tautomer in the DHHB S_1 state in cyclohexane, but there is a barrier of about 10 kJ mol^{-1} from the FC region S_1 enol in methanol solution.

and CYCH. Although the CPCM method does not treat explicit solvent-solute interactions, the calculations indicate that ESHT is a barrierless process in CYCH, whereas in MeOH there is a barrier estimated to be ~10 kJ mol^{-1}. Therefore, the rate of ESHT is expected to be dependent on the polarity of the solvent environment.

The excited state absorption (ESA) band peaking near 410 nm, and extending to longer wavelength, rises at early time delays as the partially overlapping SE feature decays in amplitude. Its maximum intensity is greater in CYCH than in MeOH, ACN and DMSO solutions, and it closely resembles a prominent ESA band observed in TEAS studies of oxybenzone that was assigned to an S_1-keto form.[15] On the basis of this evidence, and electronic structure calculations of the absorptions from the S_1 enol and keto forms (see Figure 4-11), the 410-nm ESA band seen for DHHB solutions is assigned to the S_1-keto product of ESHT. A broader ESA band extending to longer wavelength is instead attributed to the S_1-enol form. Hence, ESHT is not the only observed pathway after photoexcitation, and both S_1 keto and enol forms contribute to the TEA spectra.

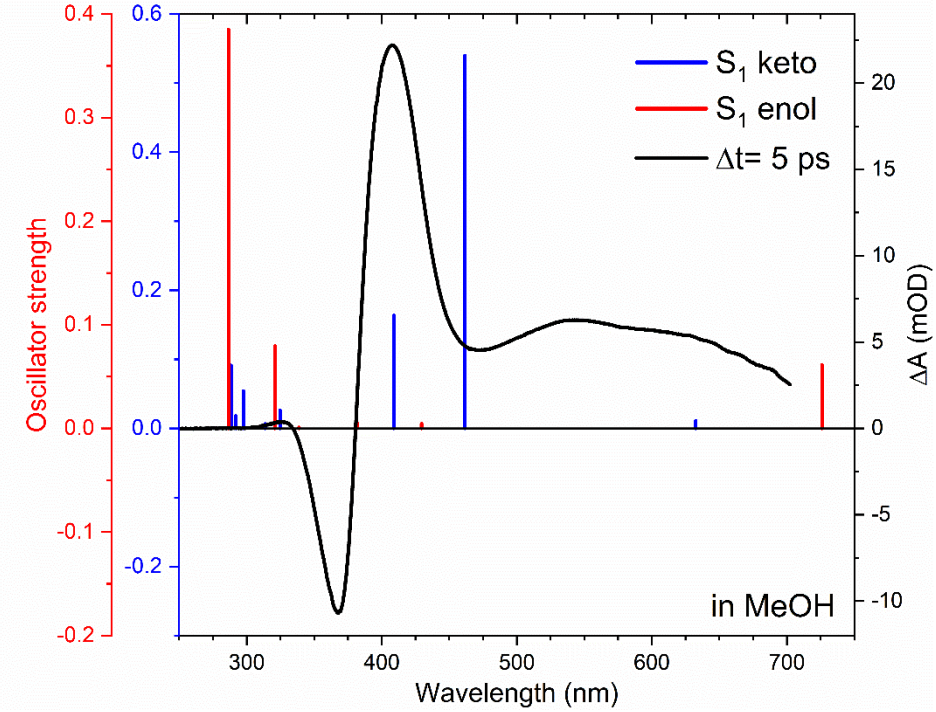

Figure 4- 11. Simulated UV-Vis absorption spectra of the optimized S_1-keto and S_1-enol tautomers are shown by blue and red bars, respectively. An experimental TEA spectrum of DHHB in methanol obtained at a time delay of 5 ps is shown by the black solid line.

Spectral Decomposition and Kinetic Analysis of TEAS data: The decomposition of DHHB TEA spectra obtained in the polar solvents into constituent absorption bands is achieved using five spectral basis functions. One of these functions models the time-evolution of the SE, and another one accounts for the changing intensity of the 410-nm ESA band of the S_1-keto DHHB. The third basis function describes changes to the ground-state bleach (GSB) feature evident at wavelengths around 360 nm. The fourth accounts for long wavelength spectral features, and it thus includes the long-wavelength ESA feature assigned to the S_1 enol (see above) at early time delays. Finally, the fifth basis function is used fit the late time spectra and grows with a fixed time constant chosen to be close to the S_1-enol lifetime. It is interpreted as representing ESA from triplet states (see below). For the decomposition of DHHB TEA spectra obtained in CYCH, a SE basis function was not required. None of the spectra shown in Figure 4-8 show any evidence of SE from the S_1 keto state in the probe wavelength window. Any such SE bands would be expected to decay on the same timescale as the loss of the S_1 keto ESA. Further details of the basis functions used are provided in the caption of Figure 4-12, and examples of the decomposition of TEA spectra in methanol and CYCH are illustrated in Figure 4-12.

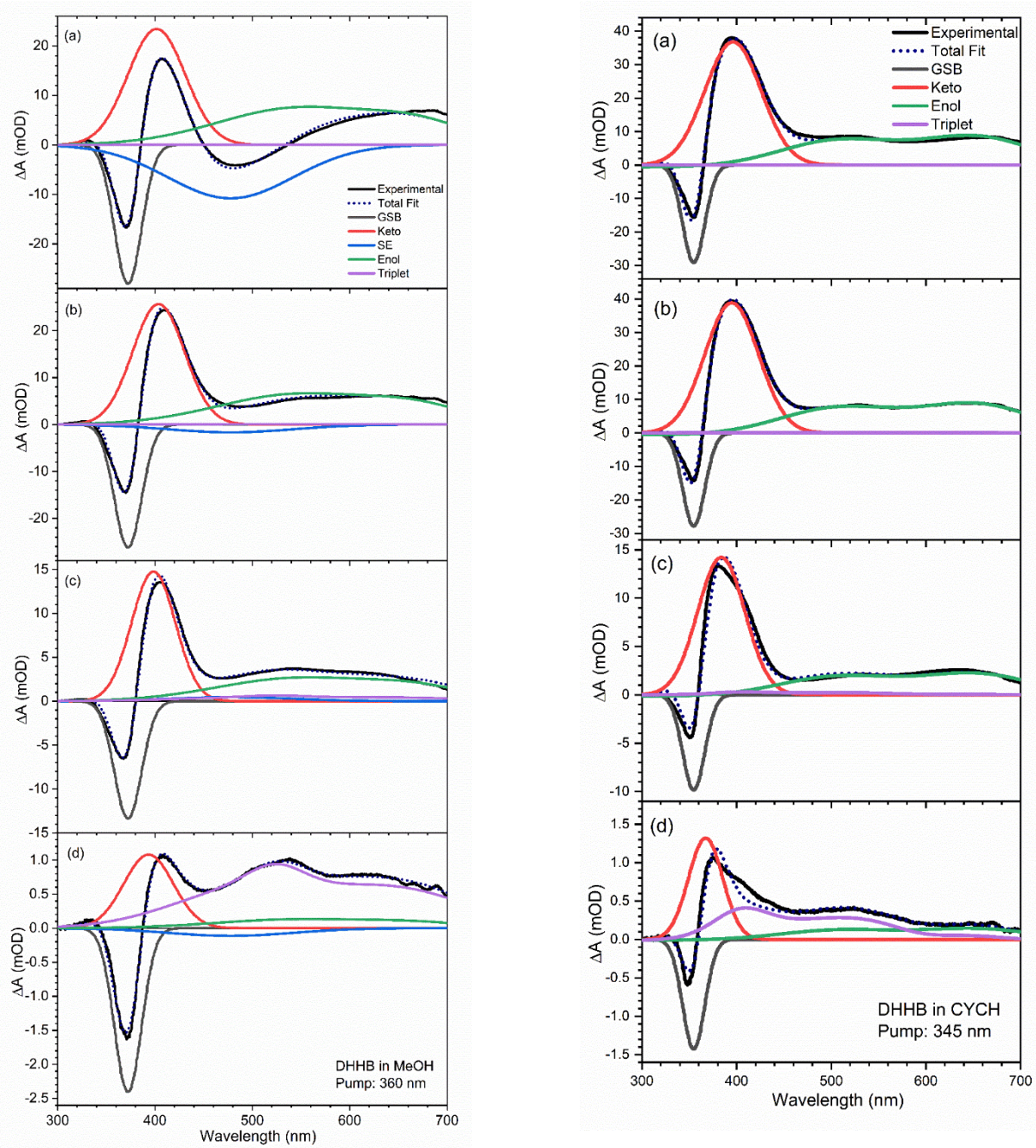

Figure 4- 12. Examples of decomposition of TEA spectra of DHHB in methanol (left) and cyclohexane (right) at time delays of Δt= (a) 0.3 ps, (b) 1.1 ps, (c) 12 ps and (d) 50 ps. The spectral decompositions used the KOALA program. The solid black line is the experimental spectrum, and the dotted navy line is the total fit from a combination of five basis functions (shown in grey, red, blue, green and purple). The grey basis function is used to simulate the kinetics of the GSB. The red basis function tracks the kinetics of ESA around 410 nm assigned to the S_1-keto tautomer. The blue basis function accounts for the kinetics of SE, and the green basis function fits the features in TEA spectra assigned to the S_1 enol. Finally, the purple basis function is extracted from the late-time spectra where triplet signals dominate.

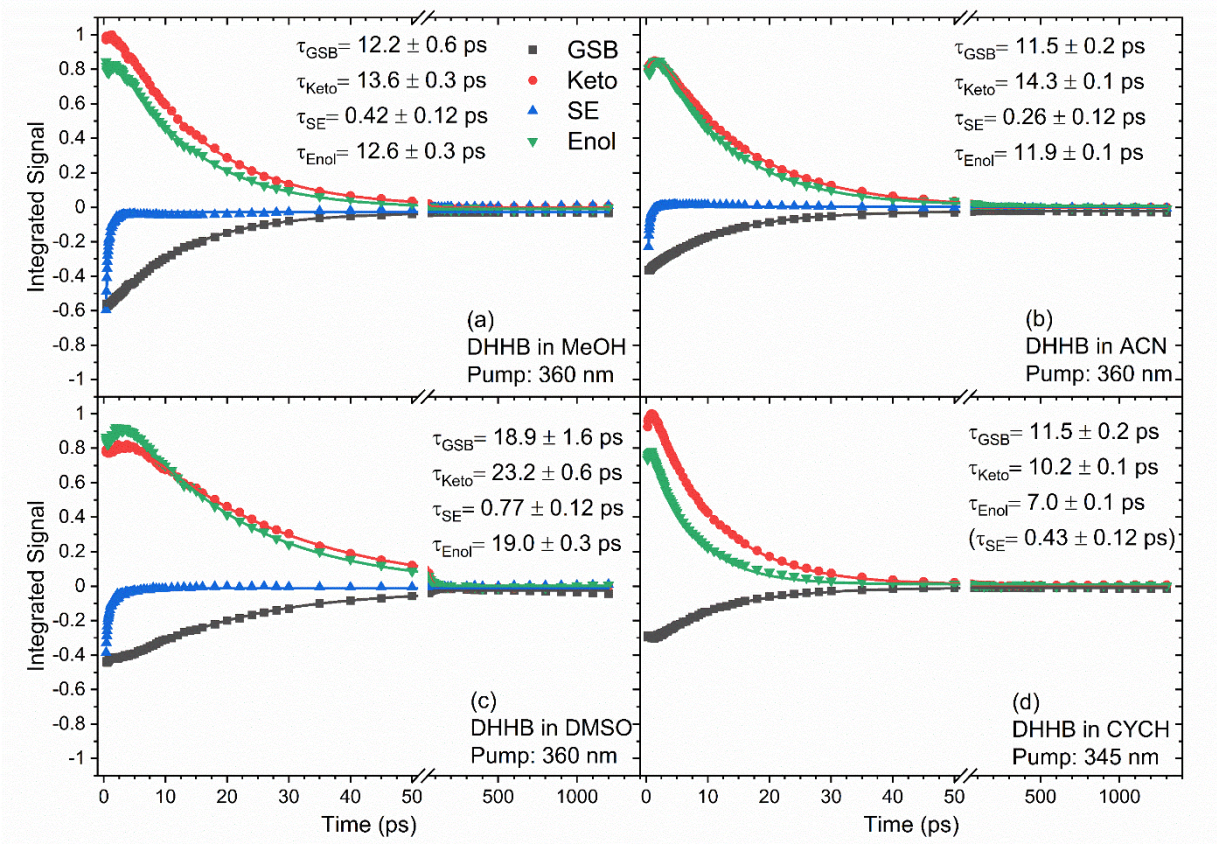

Figure 4- 13. Time dependence of the wavelength-integrated intensities of GSB (black), ESA of keto (red), SE (blue) and ESA of enol (green) features for UV-photoexcited DHHB in: (a) methanol, (b) acetonitrile, (c) dimethyl sulfoxide and (d) cyclohexane. The time constants obtained from exponential fits are shown in each panel. The integrated intensities are derived from spectral decomposition of TEA spectra shown in Figure 4-4 using methods described in the main text.

Figure 4-13 shows how the wavelength-integrated intensities of the basis functions fitted to the evolving TEA spectra change with time. The first three data points (Δt= 0.25, 0.3, 0.35 ps) in polar solvents showed unreasonably sharp decay or growth, which is attributed to fitting artefacts from the overlap of the basis functions. These first three time points were therefore excluded in subsequent kinetic fitting. The kinetics of the GSB, S_1-keto and S_1-enol components were globally fitted to extract exponential time constants reported in Figure 4-13 and Table 4-1. The kinetics of SE decay are mono-exponential in MeOH, DMSO and ACN. Although an SE basis function was not used to fit TEA spectra in CYCH, an early time rise in the intensities of the S_1 ESA features evident in Figure 4-13(d) is suspected to derive from decay of a weak, overlapping SE contribution. Therefore, the time constant for DHHB S_1 SE

decay in CYCH is estimated from global fitting of a shared time constant to the early time changes in S_1-keto, S_1-enol and GSB band intensities.

From this kinetic analysis, the time constants obtained for DHHB S_1 SE decay (τ_{SE}) range from ≤400 fs (in MeOH and ACN) to almost 800 fs (in DMSO), and the time constants for the ESA decays (τ_{Keto} and τ_{Enol}, corresponding to the S_1 keto and enol contributions) are in the range of 7 to 23 ps, also with dependence on the solvent. The time constants extracted from TEAS analysis are summarized in Table 4-1.

	MeOH	**ACN**	**DMSO**	**CYCH**
τ_{GSB} **(from TEAS)**	12.2 ± 0.6	11.5 ± 0.2	18.9 ± 1.6	11.5 ± 0.2
τ_{Keto}	13.6 ± 0.3	14.3 ± 0.1	23.2 ± 0.6	10.2 ± 0.1
τ_{SE}	0.42 ± 0.12	0.26 ± 0.12	0.77 ± 0.12	0.43 ± 0.12
τ_{Enol}	12.6 ± 0.3	11.9 ± 0.1	19.0 ± 0.3	7.0 ± 0.1
τ_{GSB} **(from TVAS)**	14.7 ± 0.4	14.8 ± 0.3	25.0 ± 0.8	12.5 ± 0.2

Table 4- 1. Relaxation time constants (ps) obtained from TEAS and TVAS in four solvents. τ_{SE}, τ_{Keto}, τ_{Enol} and τ_{GSB} are time constants for SE decay, ESA of the S_1 keto decay, ESA of the S_1 enol decay, and S_0 enol GSB recovery respectively. In CYCH, SE is not clearly observed, but an early time rise in the ESA intensity is attributed to loss of overlapping SE signal.

In prior oxybenzone studies, a time constant of ~400 fs was attributed to torsional motion in the S_1-keto form as it relaxed to its minimum energy twisted geometry.[15-17] However, in the case of DHHB our calculations show a preferred S_1-keto structure that maintains the near planarity of the OH and carbonyl groups, with the relaxed S_1 enol instead showing the corresponding twisted structure (Figure 4-5 and 4-6). The τ_{SE} = 300 fs – 800 fs time constants reported here are therefore assigned to the torsional motion of the S_1-enol tautomer, as is illustrated in Figure 4-7, while it undergoes relaxation to the S_1-enol minimum energy structure. Any excess energy in the initially photoexcited S_1 DHHB will evolve into vibrational excitation and then be dissipated to the solvent bath. The time constants for decay of SE features apparently relate to solvent viscosity: in the more viscous DMSO, τ_{SE} = 770 fs is consistent with greater resistance from the solvent to the incipient C-C bond twisting.

The time constant for excited-state hydrogen atom transfer (τ_{ESHT}) is expected to be 100 - 200 fs on the basis of observations in similar compounds.[34, 35] For example, ESHT dynamics in other common sunscreen molecules like homosalate, oxybenzone and methyl salicylate are

reported to occur within 200 fs.[16, 36, 37] ESHT in DHHB on such timescales is not directly observed in the current measurements, but is compatible with quenching of most of the SE from DHHB (S_1 enol) in CYCH within the ~150 fs TEAS instrument response.

The ESHT is suggested to be inhibited in polar solvents because of disruption of the intramolecular hydrogen bond in DHHB. The calculated PESs along the ESHT coordinate (Figure 4-10), obtained using the CPCM solvation model, predict an ESHT barrier in methanol, but no such barrier in CYCH. In the latter solvent, the majority of photoexcited DHHB molecules therefore undergo ESHT, converting to the S_1-keto form within 200 fs. A minor fraction of photoexcited DHHB remains in the S_1-enol form to undergo structural relaxation via C-C bond torsion In contrast, in the polar solvents, ESHT dynamics are proposed to occur more slowly (i.e. >200 fs). The more prominent SE from the S_1-enol form of DHHB observed in the spectra in Figures 4-8(a)-(c) is consistent with competition between this slower ESHT and the aforementioned torsional dynamics about the C-C bond that drive the S_1 enol towards its lowest energy. As is noted above, evidence for this competition comes from the ESA bands assigned to both S_1-keto and S_1-enol tautomers. As the S_1-enol form twists from its initially excited form in the Franck-Condon region, it drops in energy and the energy of the corresponding S_1-keto form increases (see Figure 4-7). Hence the torsional motion rapidly switches off the ESHT pathway, leaving populations of the S_1 enol (in a twisted geometry) and the S_1 keto to evolve separately thereafter.

The later time TEA spectra of DHHB in DMSO shown in Figure 4-7(c) differ from those obtained in MeOH and ACN, and they are instead more similar to those obtained for solutions in CYCH. The weak, long-wavelength features observed are discussed below. These similarities are consistent with slower C-C bond torsion in the more viscous DMSO providing a more extended window of opportunity for ESHT than for DHHB solutions in MeOH and ACN. The τ_{Enol} = 7 – 20 ps time constants for decay of S_1-enol ESA, with values depending on the solvent, are attributed to electronic relaxation of the excited DHHB from its S_1-enol to the S_0 electronic ground state. The relaxation pathway is likely to involve a conical intersection between the S_1 and S_0 states with a twisted central C-C bond (Figure 4-7), and the time constants of GSB recovery, τ_{GSB}, in TEAS are consistent with the τ_{Enol} values (Table 4-1), except perhaps in CYCH where S_1-keto relaxation is argued to be more significant. The τ_{Keto}= 10 - 23 ps time constants for S_1 keto decay are consistently slightly longer than the corresponding τ_{Enol} values in the

same solvent. The differences may result from an alternative decay pathway mediated by a separate CI in the keto form, or delayed reverse ESHT to repopulate the S_1-enol form before $S_1 \rightarrow S_0$ relaxation.

4.3.3 Transient vibrational absorption spectroscopy of DHHB

Ground-State DHHB Recovery: The electronically non-adiabatic dynamics of $S_1 \rightarrow S_0$ relaxation were studied further with the aid of TVA spectra, examples of which are shown in Figure 4-14 for DHHB in various solvents. On the basis of bands observed in steady state FTIR spectra (Figure 4-15), the negative-going transient absorption bands around 1633 cm^{-1} and 1725 cm^{-1} are assigned as ground state bleaches arising from photoexcitation of DHHB (S_0). The GSB in CYCH recovers nearly to baseline within the limiting 1200 ps time delay of the measurements, indicating that most of the photoexcited DHHB relaxes back to the ground state. In contrast, noticeable GSB features remain at the later time delays in all the polar solvents. In addition to these remaining GSB features, there are positive bands in the TVA spectra round 1600 cm^{-1} at these later times for DHHB dissolved in the polar solvents.

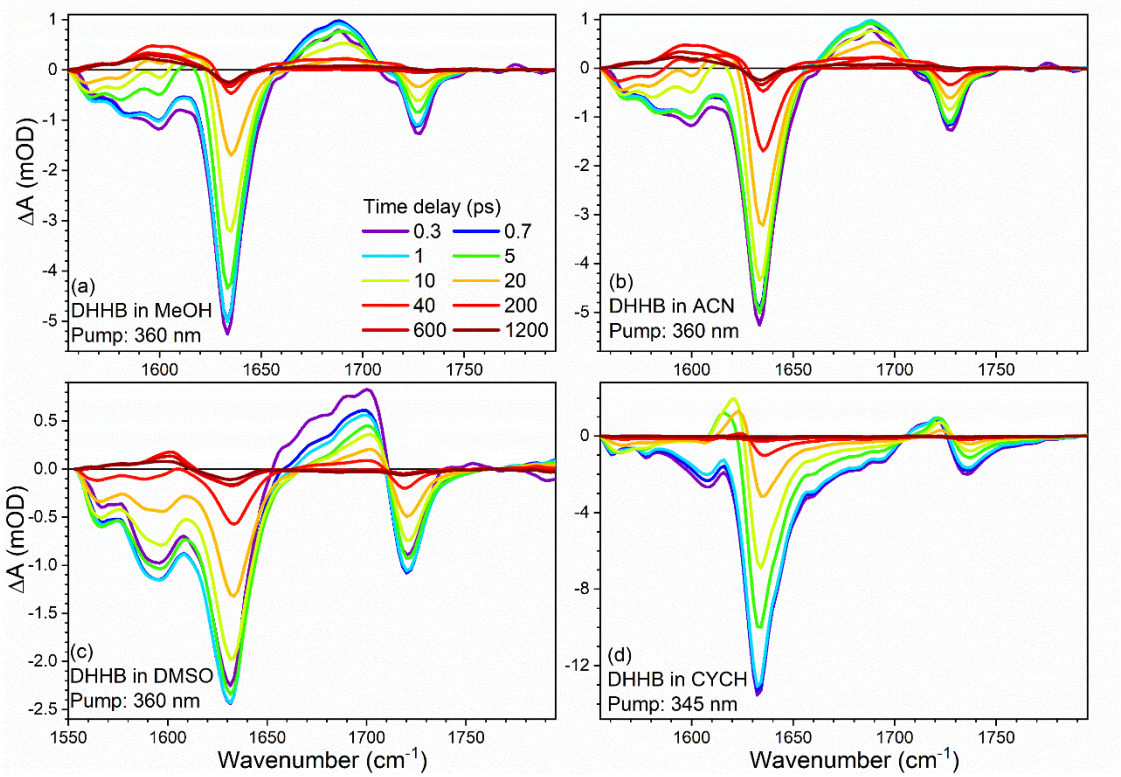

Figure 4- 14. TVA spectra of DHHB in: (a) methanol; (b) acetonitrile; (c) dimethyl sulfoxide; and (d) cyclohexane. The colour key in panel (a) shows the time delays corresponding to different spectra. The near-UV excitation (pump) wavelengths used are specified in the panels.

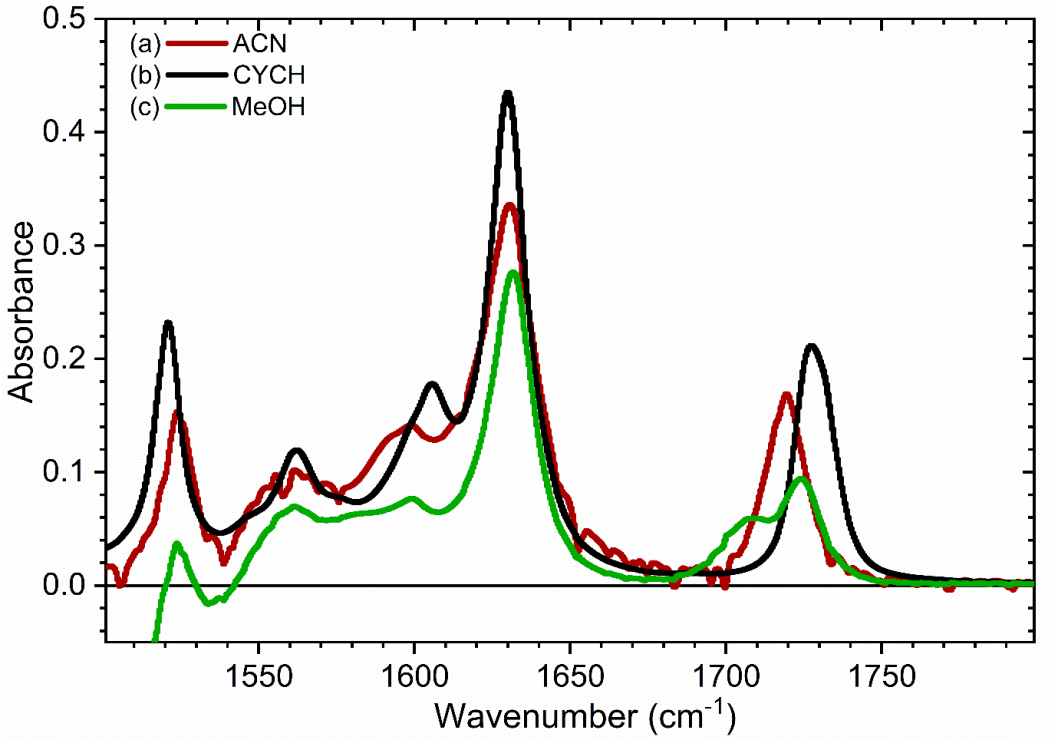

Figure 4- 15. FTIR spectra of DHHB in (a) acetonitrile (ACN), (b) cyclohexane (CYCH) and (c) methanol (MeOH), focusing on the carbonyl stretching region. The peaks at 1700 - 1750 cm^{-1} are assigned to the carbonyl group of the ester substituent and their positions are sensitive to the solvent polarity. Splitting of the band in MeOH may reflect environments with and without H-bonding of MeOH to the carbonyl group. The peaks at about 1630 cm^{-1} are assigned to the central carbonyl group and are less affected by solvent choice because of intramolecular hydrogen bonding.

The kinetics of the GSB recoveries obtained by integrating the intensities of the features centred at ~1633 cm^{-1} are shown in Figure 4-16, together with single-exponential fits with offsets. Values of the resulting time constants (τ_{GSB} from TVAS) are reported in Table 4-1; these values are in the 12 - 25 ps range, and are slightly longer than those extracted from the analysis of TEA spectra. Hence, they are assigned to $S_1 \rightarrow S_0$ relaxation via one or more conical intersections. The GSB recovery in TVAS is obtained from repopulation of S_0 molecules in their lowest vibrational level, so the recovery time constants will be affected by vibrational cooling in the S_0 state, as well as reflecting the kinetics of $S_1 \rightarrow S_0$ electronic relaxation which are derived from the TEAS analysis.

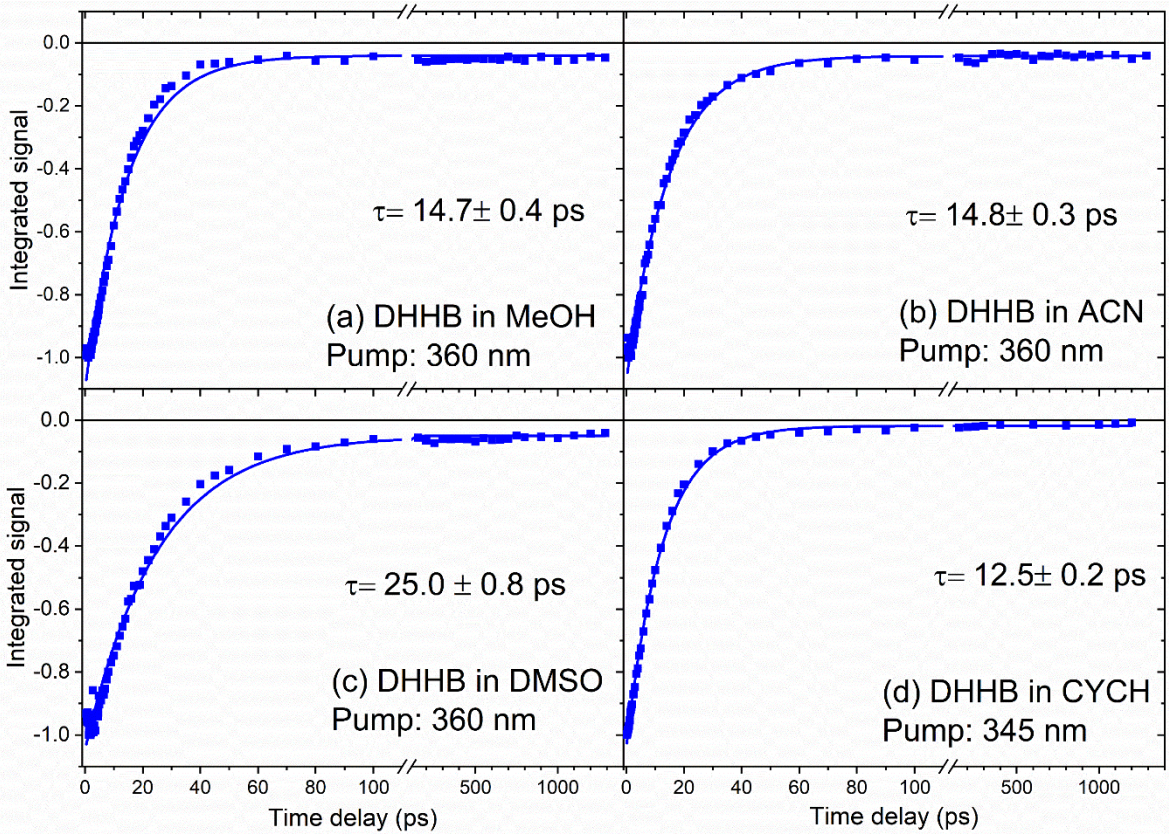

Figure 4- 16. Kinetics of DHHB ground-state bleach recovery for the band with centre at ~1633 cm^{-1} in: (a) methanol, (b) acetonitrile, (c) dimethyl sulfoxide and (d) cyclohexane. Single exponential time constants from fits shown as solid lines are reported in each panel.

Minor Photoproduct Formation: The electronic structure calculations show the optimized S_1-enol structure is twisted, and S_1 to S_0 internal conversion via a conical intersection is proposed to occur in this region. Hence, as the molecules relax through the CI to repopulate the S_0 state, the C-C bond could keep twisting to form a *trans*-enol S_0 isomer instead of reverting to the

minimum energy S_0 geometry. Figure 4-17 compares calculated IR spectra of the *trans*-enol and *trans*-keto forms of DHHB (S_0) with the late time TVA spectra of DHHB in methanol. The positive peaks at ~1600 cm^{-1} observed at later times in polar solvents are better assigned to *trans*-enol DHHB (S_0) photoproducts, thereby accounting for the incomplete recovery of the GSB features. A computational relaxed-geometry energy scan along the dihedral angle of the C(OH)–C–C=O portion of a DHHB molecule in the ground electronic state shows that the *trans*-enol is a metastable photoproduct because it must overcome a barrier to revert to the minimum energy structure (Figure 4-18). In contrast to DHHB, similar dynamics in photoexcited oxybenzone drive passage through an S_1 / S_0 conical intersection corresponding to a twisted S_1-keto structure, and further torsional dynamics on the S_0 potential energy surface lead to a minor *trans*-keto photoproduct.[15, 17] These differences between oxybenzone and DHHB relaxation pathways arise because in oxybenzone it is the S_1-keto form that has a twisted minimum energy structure, whereas in DHHB it is the S_1-enol form. The geometries of the conical intersections connecting these S_1 minima to the S_0 state influence the minor photoproduct isomers that form.

The absence of a band at 1600 cm^{-1} in TVA spectra for DHHB in CYCH is consistent with a greater propensity for ultrafast ESHT in the S_1 state. Decay from the resulting S_1-keto form is therefore proposed to be via an alternative pathway to the S_1 / S_0 conical intersection discussed above, which is argued to be located towards the twisted S_1-enol minimum energy structure. The GSB recovery approaches 98% in CYCH, and there is no obvious signature of *trans*-enol photoproduct formation. The remaining 2% is thus most likely to be a consequence of minor branching to triplet states of DHHB, and we suggest below that the outcome is population of the keto form of the T_1 state. In polar solvents, the GSB recoveries are about 95%, with the remaining 5% attributed in part to the *trans*-enol photoproducts seen by TVAS. The remainder is suggested to be a consequence of population of photoexcited triplet states, direct evidence for which comes from the TEAS measurements.

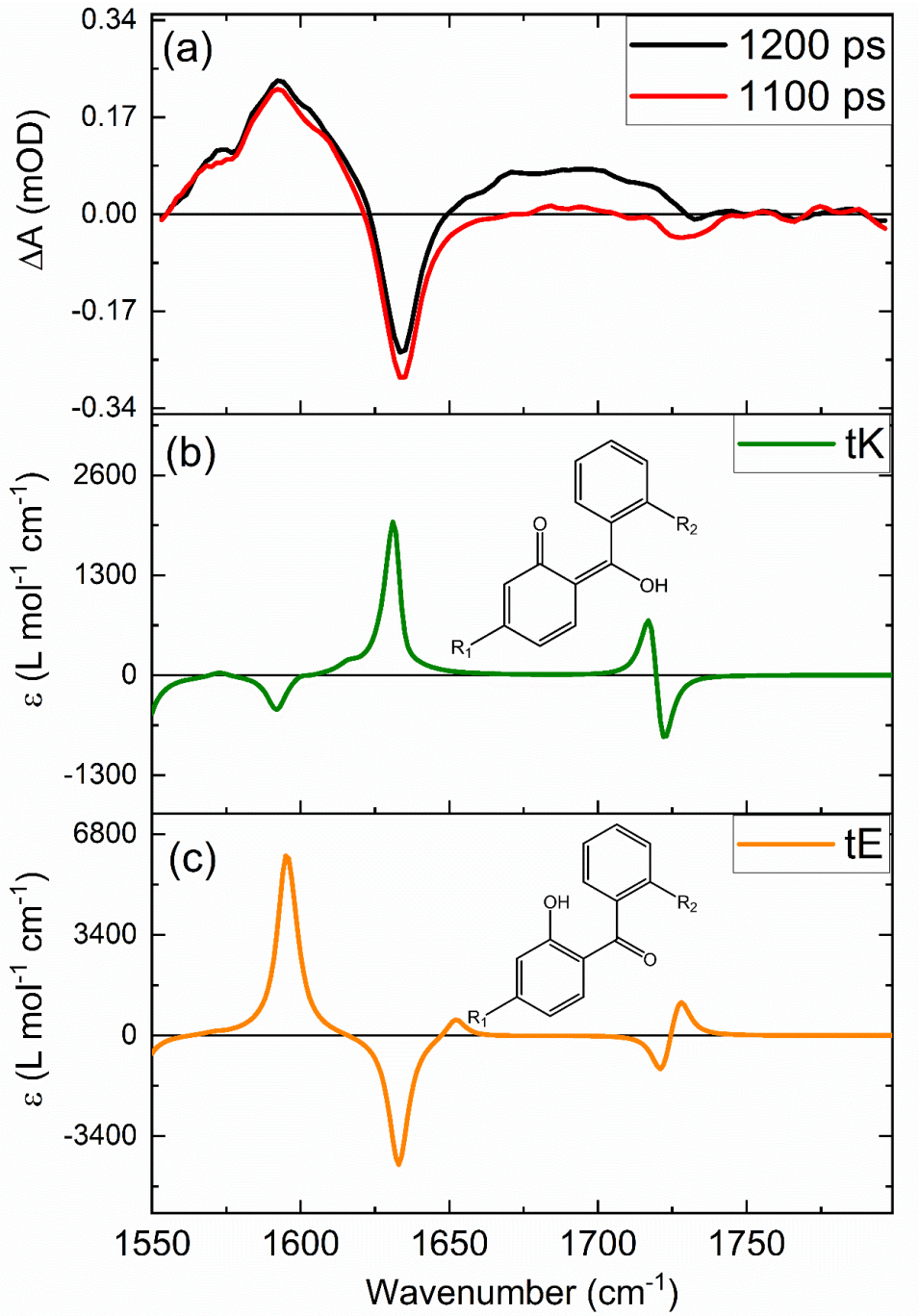

Figure 4- 17. (a) Late time TVA spectra of DHHB in methanol. A positive signal near 1600 cm^{-1} indicates a photoproduct, and the negative signal near 1630 cm^{-1} results from depletion of parent molecules (i.e. a ground state bleach). (b) A simulated late time TVA spectrum for the possible *trans*-keto (tK) photoproduct is obtained from the calculated and scaled tK vibrational spectrum by subtracting the calculated IR spectrum of ground-state DHHB. (c) A similar procedure generates the simulated late time TVA spectrum of the possible *trans*-enol (tE) photoproduct.

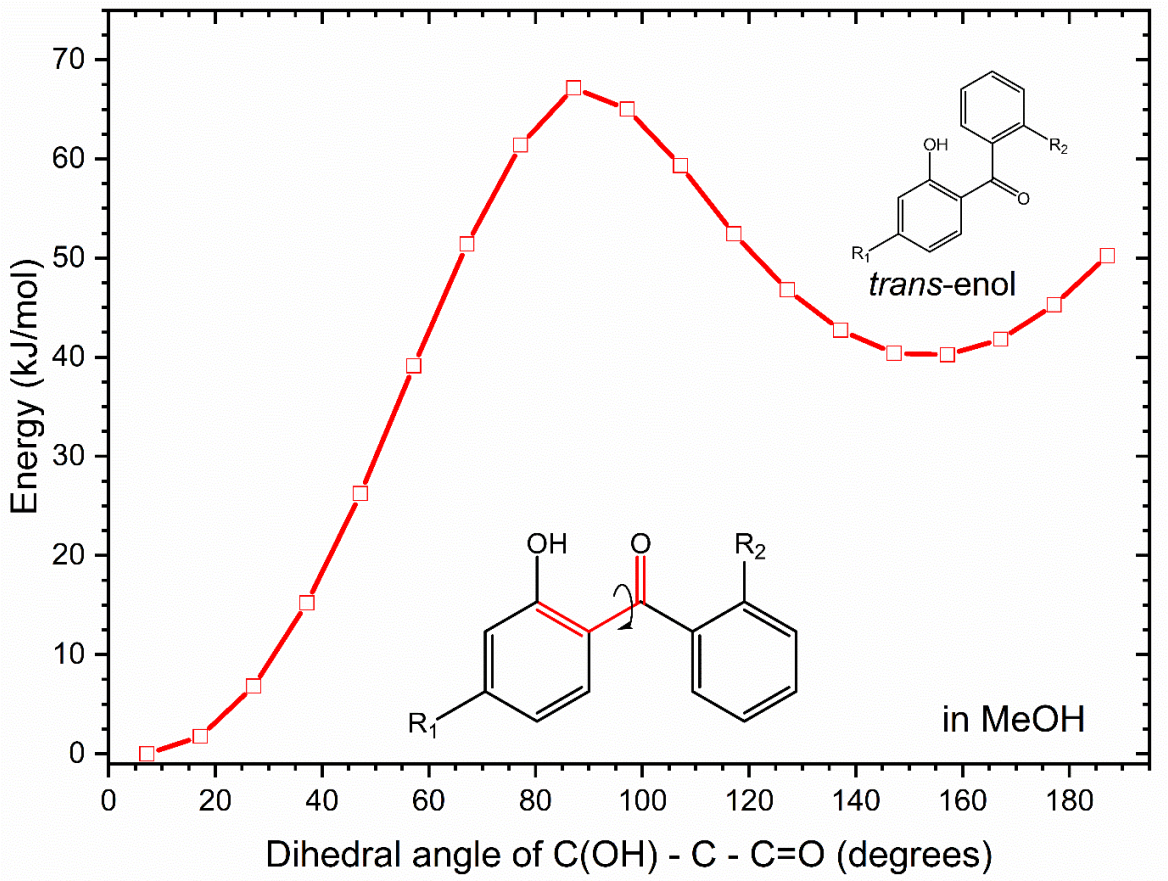

Figure 4- 18. Relaxed scan along the dihedral angle of the C(OH)-C–C=O moiety from the optimized S_0-enol DHHB, for which the dihedral angle is 7°. Calculations used a CPCM for the solvent methanol. The proposed minor photoproduct, the *trans*-enol isomer occupies a local energy minimum when the dihedral angle is around 150°. The barrier to recovery of the minimum energy isomer of DHHB (S_0) suggests that the trans-enol isomer has a lifetime beyond the range of our experimental delay times of up to 1300 ps.

4.3.4 Triplet state population and quenching

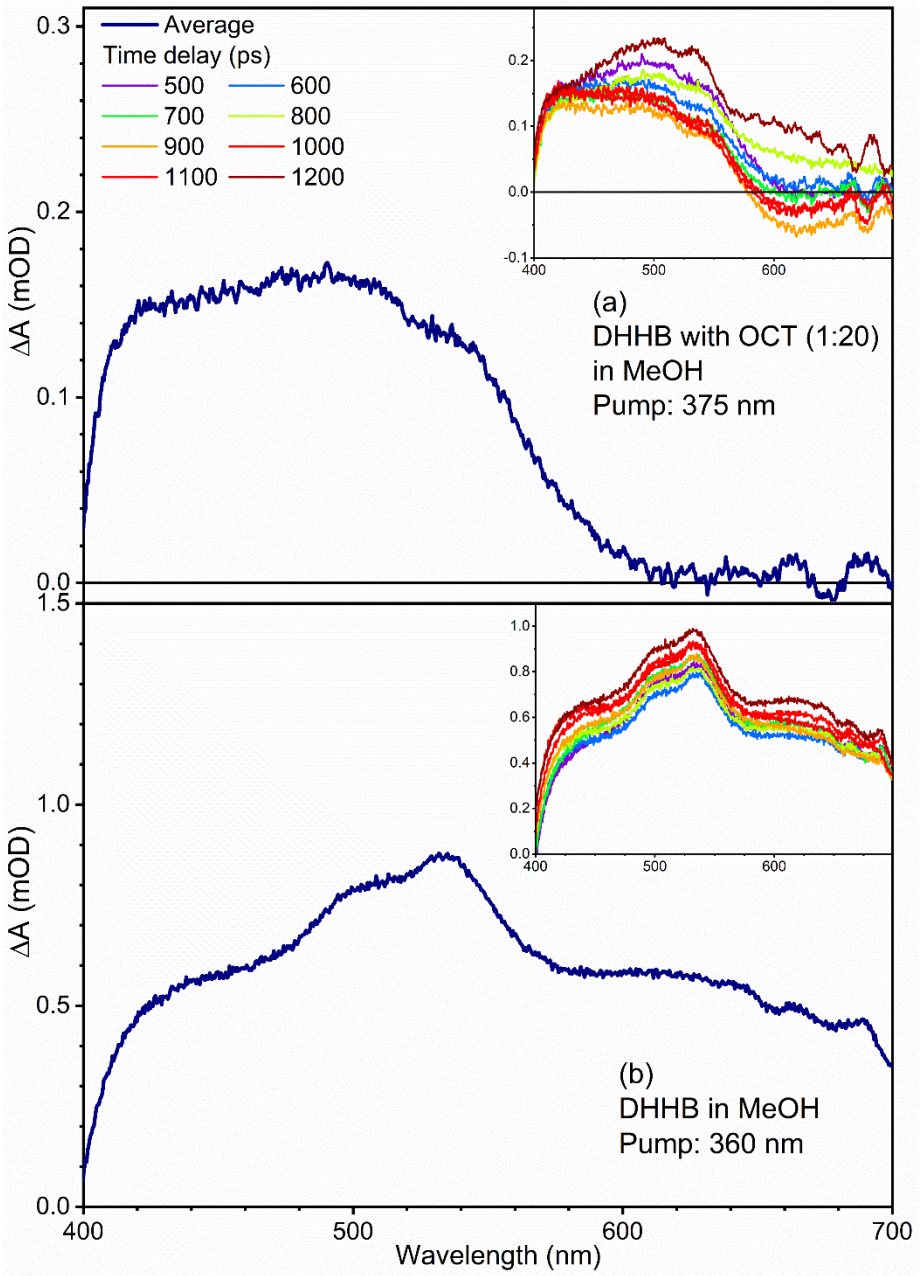

Figure 4- 19. Plots of averaged late-time (500 – 1200 ps) TEA spectra of: (a) DHHB with added octocrylene (OCT, in 20-fold excess) and (b) DHHB in methanol. The insets display the individual spectra, and the colour key shows the time delays corresponding to each spectrum.

The later time (>1000 ps) TEA spectra shown as insets in Figure 4-8 differ in their finer details in the various solvents. In MeOH, there is a long-lived absorption extending beyond 550 nm, whereas there is only weaker absorption beyond 600 nm for DHHB in CYCH. On the basis of electronic structure calculations, and quenching experiments described below, the longer-lived band seen at wavelengths beyond 550 nm is assigned to the T_1 state of DHHB. Data presented in Figure 4-19 show that the triplet-state ESA in methanol can be quenched by

adding octocrylene, which is a common UVB absorber additive in sunscreen products. Further quenching tests were performed with *trans*-β-methylstyrene, which has a similar triplet-state energy to DHHB, and the TEA spectra of these mixtures are shown in Figure 4-20.[20, 38] Again, the longer-lived signal in the long wavelength region was quenched.

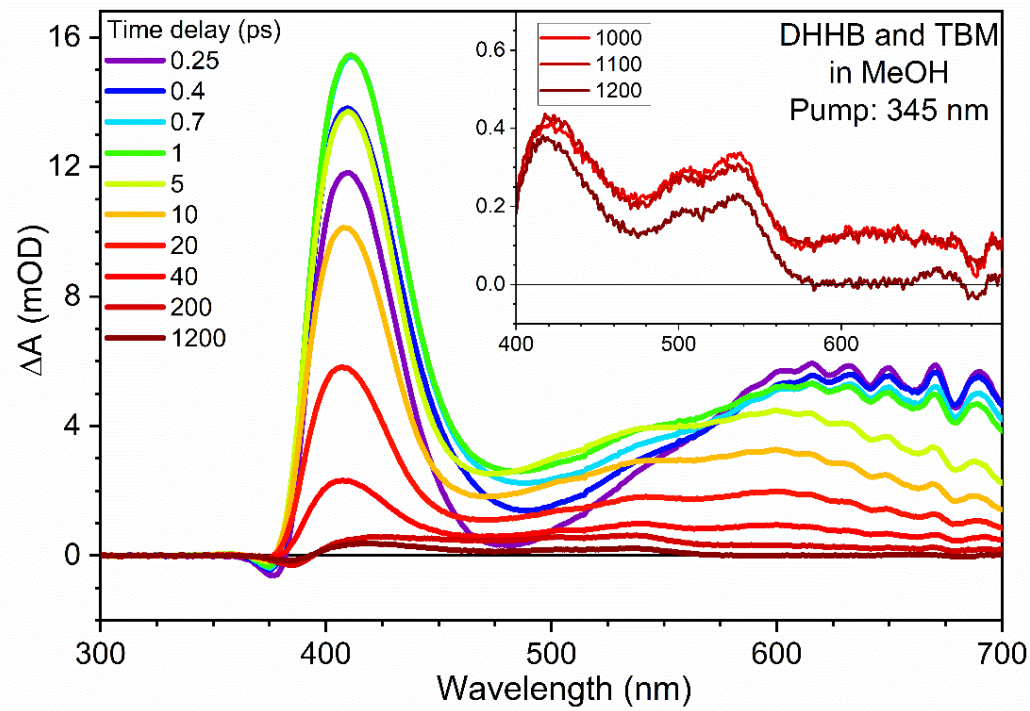

Figure 4- 20. TEA spectra of DHHB obtained in methanol with added *trans*-beta-methylstyrene (TBM, 2000 equivalents). The late time TEA spectra are shown on an expanded scale in the inset at the top right to highlight the weakness of any long wavelength absorption features attributed to the triplet enol.

Just as for the singlet manifold of states, triplet spin state DHHB can exist in enol and keto forms. The computed UV-Vis absorptions of T_1 enol and T_1 keto DHHB are shown in Figure 4-22. Guided by these calculations, the long wavelength ESA feature observed at later times in methanol is assigned to the T_1 enol, because the calculated absorption bands of the T_1 keto form are located mainly in the 400 - 500 nm wavelength region.

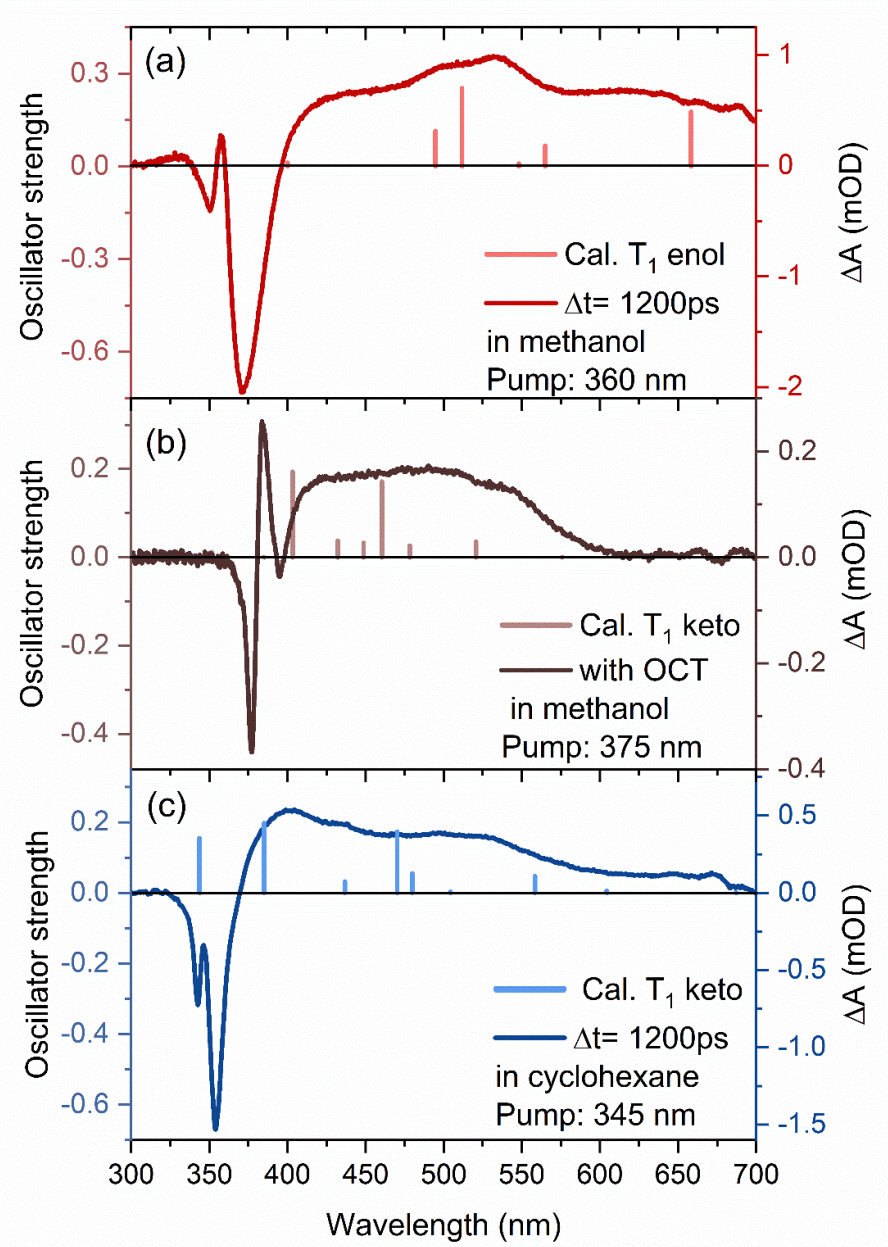

Figure 4- 21. Calculated UV-Vis ESA spectra for DHHB (T_1) in its enol and keto forms with CPCM treatment of the solvent in methanol and cyclohexane. (a) calculated T_1 enol (red bars) in methanol, and a comparison with a late-time experimental TEA spectrum (dark red). (b) calculated T_1 keto (brown bars) in methanol, and a comparison with an averaged late time spectrum with octocrylene (dark brown) from Figure 7 in the main text. (c) calculated T_1 keto (light blue bars) in cyclohexane, and a comparison with a late time experimental TEA spectrum (dark blue). The sharp features (at ~360 nm in methanol, at ~375 nm in the spectrum with octocrylene, and at ~345 nm in cyclohexane) are attributed to small amounts of pump laser scattering.

As Figure 4-19 shows, in the presence of octocrylene only a 400 - 500 nm ESA feature remains in the long-time spectra, which is attributed to the T_1-keto form of DHHB. Unlike the T_1-enol DHHB, this T_1-keto tautomer is not quenched by octocrylene because its triplet-state

excitation energy is significantly smaller than that for the T_1 enol relative to their corresponding S_0 tautomers. The S_0-keto tautomer lies higher in energy than the S_0 enol, whereas the energy ordering is reversed in the T_1 state. Hence, the $T_1 - S_0$ energy gap in the keto form is insufficient to sensitize the octocrylene or *trans*-β-methylstyrene. The late time TEA spectra in CYCH (Figure 4-21) mainly show T_1 keto signals, consistent with the proposition that ESHT from S_1-enol to S_1-keto forms is more significant in CYCH. In DMSO, the T_1-enol absorption is weaker than in the other polar solvents, and the late time spectra look similar to those obtained in CYCH. These observations are taken as further evidence that that the more viscous solvent environment in DMSO slows down C-C twisting in the S_1 enol and instead promotes ESHT.

Transient absorption spectra of DHHB in ethanol, obtained at time delays of 0.3 - 1.2 μs by Shamoto et al. show a broad ESA signature peaking near 400 nm and extending up to ~500 nm that resembles the ESA band assigned here to the T_1-keto tautomer.[20] Mechanistic arguments suggest the T_1-enol tautomer should be preferentially formed in protic solvents (e.g. MeOH or ethanol) which suppress the ESHT, but in the T_1 state, the keto form is computed to lie lower in energy than the enol form. Hence, it is possible that the T_1 enol undergoes hydrogen transfer to the T_1 keto with a nanosecond to microsecond time constant that is outside the time window of the reported ultrafast spectroscopy experiments but accessible to the measurements of Shamoto et al. In their experiments using DHHB in 3-methylpentane, this T_1 keto ESA was not observed, which suggests either that the T_1 keto lifetime is < 0.3 μs, or that S_1-state ESHT (favoured in non-polar solvents) hinders the intersystem crossing (ISC) from singlet to triplet states. The combined evidence from this prior and the current work points to the ISC occurring from the vicinity of the twisted S_1-enol geometry, in competition with internal conversion to S_0 via a conical intersection. However, the later time TEA spectra of DHHB in CYCH do not show the ESA features assigned to the T_1-enol form, although bands are evident which could correspond to the T_1-keto form (on the basis of the aforementioned calculations). Thus, there may also be an accessible ISC pathway from the S_1-keto to the T_1-keto forms.

4.4 Conclusions

Ultrafast transient absorption spectra of the sunscreen compound DHHB, photoexcited at wavelengths around 360 nm and 345 nm, differ significantly in polar and non-polar solvents. In the non-polar cyclohexane, ESHT happens in <200 fs from the Franck-Condon region of the S_1 state, converting the S_1-enol to the S_1-keto form, and is the main dynamical pathway. Evidence is presented from TEA spectra that a small fraction of the S_1-keto intermediate subsequently populates the T_1 state in its keto form via intersystem crossing. However, TVA spectra show that >98% of the photoexcited DHHB relaxes back to the ground state with an exponential time constant of ~12ps. In three chosen polar solvents, methanol, acetonitrile and DMSO, disruption of the intramolecular hydrogen bond in DHHB inhibits ESHT from the initially excited S_1-state enol. Therefore, a greater proportion of the photoexcited DHHB retains its S_1-enol character and relaxes by C-C bond torsion that quenches stimulated emission bands observed by TEAS with a solvent-dependent time constant of 300 – 800 fs. A small fraction ($\leq$5%) of the twisted S_1-enol intermediates undergoes intersystem crossing to the T_1 enol, which is observed by TEAS at later time delays. This T_1 enol population can be quenched by adding octocrylene (a UVB absorber), showing that sunscreen formulations containing both DHHB and octocrylene can influence the sun protection efficiency. The octocrylene should inhibit build-up of undesirable DHHB (T_1) photoproducts, but could itself be sensitized to an excited triplet state in the process. A competing photoproduct, the *trans*-enol isomer of DHHB, is formed via a conical intersection between the S_1 and S_0 states, and is directly observed in low yield by TVAS of photoexcited DHHB in polar solvents. The remaining 95% of photoexcited DHHB relaxes back to the minimum energy structure on the S_0 ground-electronic state with a time constant of ~15 ps that is associated with a combination of S_1-state decay and vibrational cooling of internally excited S_0 molecules. Although DHHB and oxybenzone are structurally similar, differences in their S_1 PESs for keto and enol forms substantially change the relaxation pathways that are essential for good sunscreen performance.

References

1. E. Sage, P. M. Girard and S. Francesconi, *Photochem. Photobiol. Sci.*, 2012, **11**, 74-80.
2. N. R. Attard and P. Karran, *Photochem. Photobiol. Sci.*, 2012, **11**, 62-68.
3. G. P. Pfeifer and A. Besaratinia, *Photochem. Photobiol. Sci.*, 2012, **11**, 90-97.

4. A. Sample, B. Z. Zhao, L. Qiang and Y. Y. He, *J. Biol. Chem.*, 2017, **292**, 14786-14795.
5. J. C. Sutherland and K. P. Griffin, *Radiat. Res.*, 1981, **86**, 399-410.
6. G. T. Wondrak, M. J. Roberts, D. Cervantes-Laurean, M. K. Jacobson and E. L. Jacobson, *J. Invest. Dermatol.*, 2003, **121**, 578-586.
7. F. Bruge, L. Tiano, P. Astolfi, M. Emanuelli and E. Damiani, *PLoS One*, 2014, **9**, 11.
8. U. Osterwalder, M. Sohn and B. Herzog, *Photodermatol. Photo.*, 2014, **30**, 62-80.
9. N. A. Shaath, *Photochem. Photobiol. Sci.*, 2010, **9**, 464-469.
10. C. M. Kawakami, L. N. C. Maximo, B. B. Fontanezi, R. S. da Silva and L. R. Gaspar, *Eur. J. Pharm. Sci.*, 2017, **99**, 299-309.
11. V. Lhiaubet-Vallet, M. Marin, O. Jimenez, O. Gorchs, C. Trullas and M. A. Miranda, *Photochem. Photobiol. Sci.*, 2010, **9**, 552-558.
12. Y. T. Cho, H. Su, I. C. Huang, C. Y. Lai and Y. D. Tsai, *Anal. Methods*, 2019, **11**, 6013-6022.
13. L. Ouchene, I. V. Litvinov and E. Netchiporouk, *J. Cutan. Med. Surg.*, 2019, **23**, 648-649.
14. C. A. Downs, E. Kramarsky-Winter, R. Segal, J. Fauth, S. Knutson, O. Bronstein, F. R. Ciner, R. Jeger, Y. Lichtenfeld, C. M. Woodley, P. Pennington, K. Cadenas, A. Kushmaro and Y. Loya, *Arch. Environ. Contam. Toxicol.*, 2016, **70**, 265-288.
15. L. A. Baker, M. D. Horbury, S. E. Greenough, P. M. Coulter, T. N. Karsili, G. M. Roberts, A. J. Orr-Ewing, M. N. Ashfold and V. G. Stavros, *J. Phys. Chem. Lett.*, 2015, **6**, 1363-1368.
16. C. X. Li, W. W. Guo, B. B. Xie and G. Cui, *J. Chem. Phys.*, 2016, **145**, 074308.
17. T. N. V. Karsili, B. Marchetti, M. N. R. Ashfold and W. Domcke, *J. Phys. Chem. A*, 2014, **118**, 11999-12010.
18. M. T. Ignasiak, C. Houée-Levin, G. Kciuk, B. Marciniak and T. Pedzinski, *Chemphyschem*, 2015, **16**, 628-633.
19. S. Y. Hou, W. M. Hetherington, G. M. Korenowski and K. B. Eisenthal, *Chem. Phys. Lett.*, 1979, **68**, 282-284.
20. Y. Shamoto, M. Yagi, N. Oguchi-Fujiyama, K. Miyazawa and A. Kikuchi, *Photochem. Photobiol. Sci.*, 2017, **16**, 1449-1457.
21. A. Beeby and A. E. Jones, *Photochem. Photobiol.*, 2000, **72**, 10-15.
22. A. Kikuchi, K. Shibata, R. Kumasaka and M. Yagi, *Photochem. Photobiol. Sci.*, 2013, **12**, 246-253.
23. A. Kikuchi, N. Oguchi-Fujiyama, K. Miyazawa and M. Yagi, *Photochem. Photobiol.*, 2014, **90**, 511-516.
24. S. Matsumoto, R. Kumasaka, M. Yagi and A. Kikuchi, *J. Photochem. Photobiol. A*, 2017, **346**, 396-400.
25. A. Kikuchi, Y. Nakabai, N. Oguchi-Fujiyama, K. Miyazawa and M. Yagi, *J. Lumines.*, 2015, **166**, 203-208.
26. G. M. Roberts, H. J. B. Marroux, M. P. Grubb, M. N. R. Ashfold and A. J. Orr-Ewing, *J. Phys. Chem. A*, 2014, **118**, 11211-11225.
27. K. Rottger, H. J. B. Marroux, A. F. M. Chemin, E. Elsdon, T. A. A. Oliver, S. T. G. Street, A. S. Henderson, M. C. Galan, A. J. Orr-Ewing and G. M. Roberts, *J. Phys. Chem. B*, 2017, **121**, 4448-4455.
28. S. Urahata and S. Canuto, *Int. J. Quantum Chem.*, 2000, **80**, 1062-1067.
29. V. R. Kumar, N. Rajkumar and S. Umapathy, *J. Chem. Phys.*, 2015, **142**, 12.
30. V. R. Kumar, C. Verma and S. Umapathy, *J. Chem. Phys.*, 2016, **144**, 12.
31. S. H. Wang, W. H. Fang, T. Y. Li, F. F. Li, C. L. Sun, Z. W. Li and Z. W. Men, *Opt. Express*, 2016, **24**, 10132-10141.

32. Edinburgh Instruments Ltd., Raman Scattering in Fluorescence Emission Spectra - Common Errors in Fluorescence Spectroscopy, https://www.edinst.com/blog/raman-scattering-blog/, (accessed September 21, 2021).
33. Y. Marcus, *Chem. Soc. Rev.*, 1993, **22**, 409-416.
34. J. L. Herek, S. Pedersen, L. Banares and A. H. Zewail, *J. Chem. Phys.*, 1992, **97**, 9046-9061.
35. D. A. Horke, H. M. Watts, A. D. Smith, E. Jager, E. Springate, O. Alexander, C. Cacho, R. T. Chapman and R. S. Minns, *Phys. Rev. Lett.*, 2016, **117**, 5.
36. A. Watwiangkham, T. Roongcharoen and N. Kungwan, *J. Photochem. Photobiol. A*, 2020, **389**, 11.
37. E. L. Holt, K. M. Krokidi, M. A. P. Turner, P. Mishra, T. S. Zwier, N. D. N. Rodrigues and V. G. Stavros, *Phys. Chem. Chem. Phys.*, 2020, **22**, 15509-15519.
38. P. M. Crosby, J. M. Dyke, J. Metcalfe, A. J. Rest, K. Salisbury and J. R. Sodeau, *J. Chem. Soc.-Perkin Trans. 2*, 1977, 182-185.

Chapter 5. Phenyl cation generation from photodissociation of chlorobenzene

5.1 Introduction

The phenyl cation is a reactive intermediate with wide applications in organic syntheses and nitrogen capture.[1-5] It has low-lying singlet and triplet spin-states, and details of the reactivity and applications of phenyl cations in these two states are presented in Chapter 1.4. Recent reports suggest that phenyl cations can be generated from UV photodissociation of phenyl halides,[1, 6] in competition with the well-known homolytic C-X (X = halogen) bond fission of organohalides to make radical fragments. Therefore, the work presented in this chapter focuses on the photochemistry of chlorobenzene to explore this possibility.

Photodissociation of chlorobenzene has previously been studied with time-resolved mass spectrometry in the gas phase and using quantum-chemical computations.[7] Chlorobenzene can be photo-dissociated directly by excitation at 193 nm because the S_4 state reached is a repulsive ($n\sigma^*$) state that is dissociative along the C-Cl bond without a barrier.[7-9] Moreover, photodissociation of chlorobenzene has been reported to take place with UV radiation at longer wavelengths around 248 nm to 266 nm where the S_1 state is populated.[10-13] Because the S_1 state is a bound ($\pi\pi^*$) state, the dissociation is assumed to happen after intersystem crossing or internal conversion to different electronic states. Crossings to repulsive states like the S_4 and the T_5 states are accessible from the S_1 state when the excitation wavelength is 248 nm or shorter. However, the photon energy corresponding to 266 nm excitation is insufficient to reach the conical intersections or crossings to these repulsive states, so the photodissociation pathway following 266 nm excitation is via the vibrationally hot ground state and slower.[7, 11, 12] The potential energy surfaces of chlorobenzene along the C-Cl bond extension coordination calculated by Liu *et al.* with multireference complete active space self-consistent-field second-order perturbation theory (MSCASPT2) are shown schematically in Figure 5-1.[7]

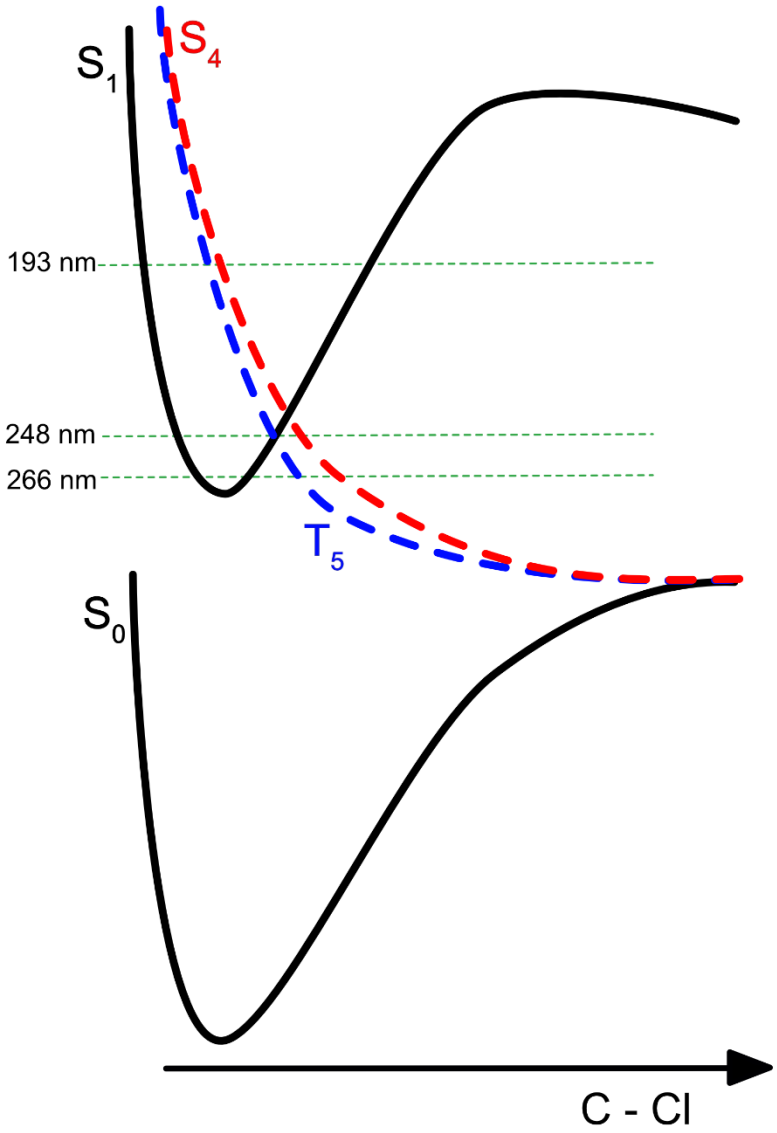

Figure 5- 1. The potential energy surfaces of chlorobenzene plotted along the C-Cl bond extension coordinate.[7] A repulsive state, S_4 (red dashed line), can be populated with excitation at 193 nm, and it leads to direct photodissociation. With excitation at 248 nm, a crossing to the T_5 repulsive state (blue dashed line) is accessible for photodissociation. The dissociation pathway from the low vibrational levels of the S_1 state is likely to occur via the vibrationally hot S_0 state after internal conversion.

In the gas phase, two time constants for relaxation of photoexcited chlorobenzene in the S_1 state were observed by time-resolved mass spectrometry after 266-nm photoexcitation. These time constants were assigned as intramolecular vibrational energy redistribution on a sub-picosecond (0.15- 0.35 ps) timescale, and the sub-nanosecond (0.75- 1 ns) lifetime of the S_1 state .[11, 14] In cyclohexane solution, the fluorescence lifetime of the chlorobenzene S_1 state is similar, and the lifetime of the triplet state in cyclohexane was measured using phosphorescence and transient absorption spectroscopy to be about 1 µs.[6, 15]

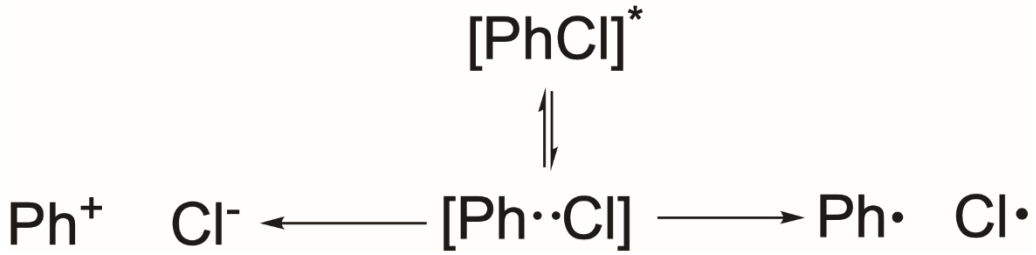

Figure 5- 2. Proposed photochemistry steps of chlorobenzene. Photoexcited chlorobenzene undergoes homolysis into a radical pair in a solvent cage, and it can rebind to recover the parent molecule. The radical pair might form an ion pair by electron transfer while in the solvent cage, or the two radicals can diffuse apart.

The photoproducts of chlorobenzene in the gas phase are suggested to be a phenyl radical and a chlorine radical,[10, 12] and homolytic bond cleavage is also expected in weakly interacting solvents such as cyclohexane because the ion-pair states of chlorobenzene cannot be reached with the excitation wavelengths used here.[16] Using nanosecond laser spectroscopy, Da Silva *et al.* proposed the mechanism of phenyl cation formation in solution to be electron transfer between a phenyl radical and a chlorine radical trapped in a solvent cage before diffusing apart (Figure 5-2).[17, 18] However, the electron transfer step was not observed directly with their nanosecond laser methods. Moreover, the ionisation energy of a phenyl radical to produce a phenyl cation is more than 8 eV,[19] and the electron affinity of a chlorine atom is 3.6 eV.[20, 21] Therefore, the mechanism would require a significant amount of energy, and it is not likely to be energetically feasible unless the ionic products are very strongly stabilised by a polar solvent and by their mutual Coulomb attraction at short range.

Phenyl radicals can abstraction a hydrogen atom from solvent molecules like cyclohexane, ethanol or acetonitrile, with solvent radicals formed.[17] On the other hand, the phenyl cation is reactive with acetonitrile and nucleophiles.[22, 23] Therefore, inert solvents like perfluorohexane are chosen for the current transient absorption spectroscopy study in place of more commonly used organic solvents. Perfluorohexane does not react with intermediates such as carbenes,[24, 25] and is likely to be unreactive towards phenyl cations. Moreover, fluorocarbons like perfluorohexane can dissolve significantly larger amounts of gases such as O_2 or N_2 than other solvents,[26] which could enable observation of nitrogen capture by phenyl cations. In addition, the effects of different substituent groups on the *para* site of chlorobenzene will be studied because the substituent can affect the stabilities of phenyl cations and the energy gaps between the singlet and triplet states of the cation.[4, 6, 27, 28] This

chapter reports the transient electronic absorption spectra of chlorobenzene and 1-chloro-4-(trifluoromethyl)benzene in solution, and possible future directions of this project are discussed.

5.2 Experimental method

Chlorobenzene (PhCl, Acros Organics, 99.9% for HPLC) and 1-chloro-4-(trifluoromethyl)benzene (CF_3PhCl, Alfa Aesar, 98+%) were used as received, and were dissolved in cyclohexane (Acros Organics, 99+% for spectroscopy) or perfluorohexane (Aldrich, 99%) using an ultrasonic bath to make 0.2 M solutions. For transient electronic absorption spectroscopy studies, and for measurements of steady state UV-Vis absorption spectra with a GENESYS 10S UV−vis spectrophotometer (Thermo Scientific), the sample pathlength was set using 200-μm-thick polytetrafluoroethylene (PTFE) spacers. For FT-IR spectra measured by a Spectrum Two FTIR Spectrometer (PerkinElmer), the PTFE spacers were 100-μm thick. Further details of the transient absorption spectroscopy methods were provided in Chapter 2. DFT calculations using the CAM-B3LYP/aug-cc-pVTZ level of theory were applied to obtain energies and vibrational frequencies of the ground state species,[29-33] and the TD-DFT CAM-B3LYP/aug-cc-pVTZ method was used to simulate the optimised structure and the vibrational frequencies of the species in their electronically excited states.[34, 35] All the calculations were performed using the Gaussian 09 package.[36]

5.3 Results and discussion

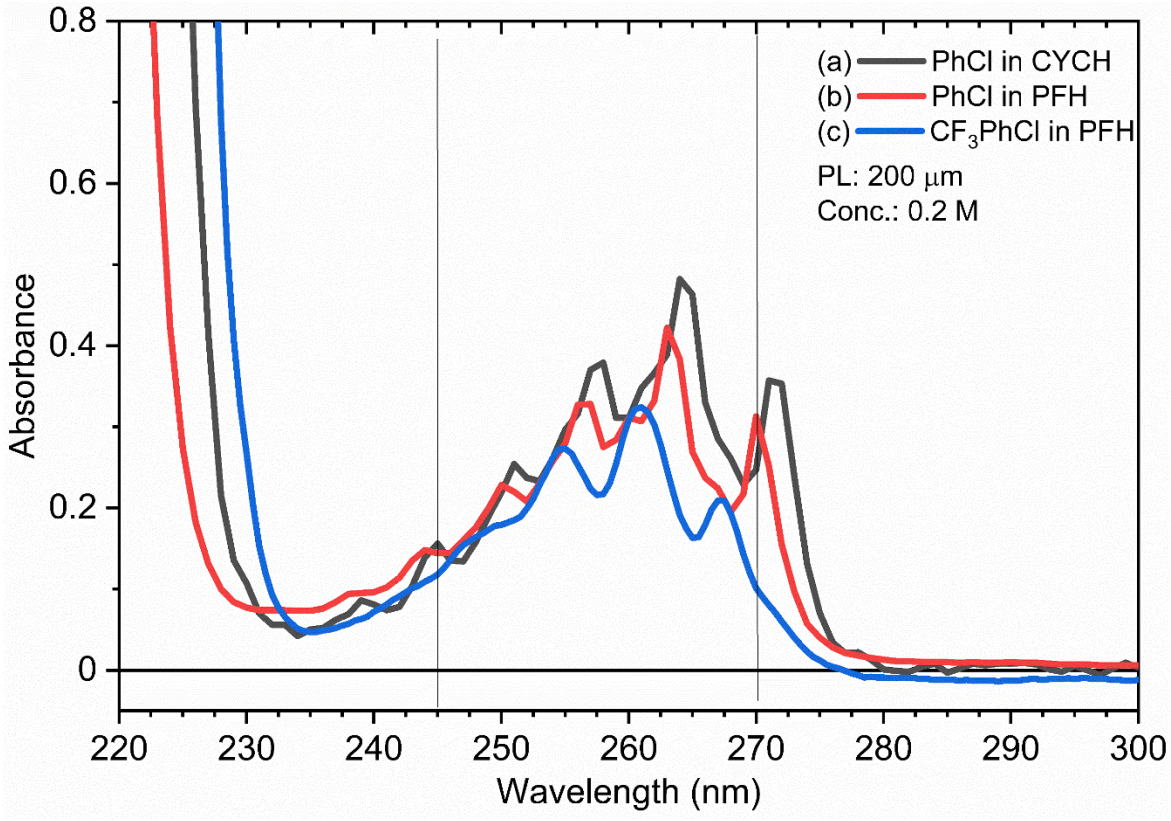

Figure 5- 3. The UV-Vis absorption spectra of (a) chlorobenzene in cyclohexane, (b) chlorobenzene in perfluorohexane (PFH), and (c) 1-chloro-4-(trifluoromethyl)benzene in PFH. The sample pathlengths are 200 μm, and the concentrations are 0.2 M.

The steady state UV-Vis absorption spectra of PhCl and CF_3PhCl are shown in Figure 5-3. Vibrational structures in the electronic absorption bands can be seen in the spectra, and the pump wavelength for transient electronic absorption spectroscopy is chosen to be 245 nm or 270 nm. With 245 nm excitation, the crossing point from the S_1 state to the repulsive T_5 state is energetically available, whereas the main photodissociation is via the vibrationally hot ground state for excitation at 270 nm.[7] The transient electronic absorption (TEA) spectra of PhCl in cyclohexane and perfluorohexane with pump laser wavelengths of 245 nm and 270 nm are shown in Figure 5-4. The most noticeable difference between the TEAS data in cyclohexane and perfluorohexane is the prominence of the band centred near 540 nm rising significantly at mid-time delays (~100 ps) and decaying when perfluorohexane is the solvent. When it comes to pump wavelength dependence, the early time (Δt= 0.35 ps) TEA spectra do not change dramatically, but some differences are apparent between the TEA spectra in cyclohexane with excitation at 245 nm and 270 nm. The rising feature at around 540 nm is

slightly stronger with a 270 nm pump wavelength than with 245 nm excitation, and the late time TEAS (Δt= 1200 ps) measurements in cyclohexane solutions excited with 270 nm (Figure 5-4b) show a peak at 400 nm. On the other hand, there are two peaks at 375 nm and 480 nm in the late time spectrum for PhCl in cyclohexane excited at 245 nm (Figure 5-4a). However, any pump wavelength dependence is not obvious in perfluorohexane.

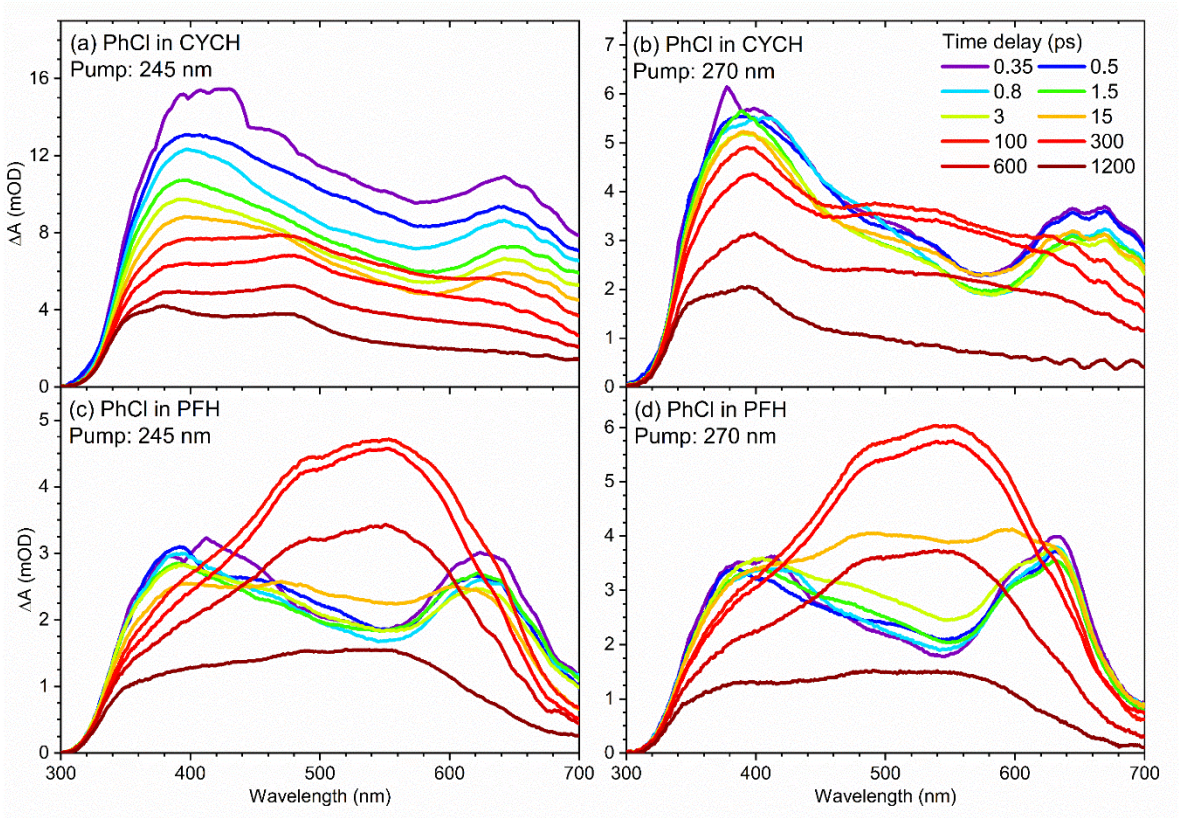

Figure 5- 4. Transient electronic absorption spectra of chlorobenzene in (a) cyclohexane with excitation at 245nm, (b) cyclohexane with excitation at 270 nm, (c) perfluorohexane with excitation at 245 nm and (d) perfluorohexane with excitation at 270 nm. The time delays of spectra are shown in the colour keys in panel (b).

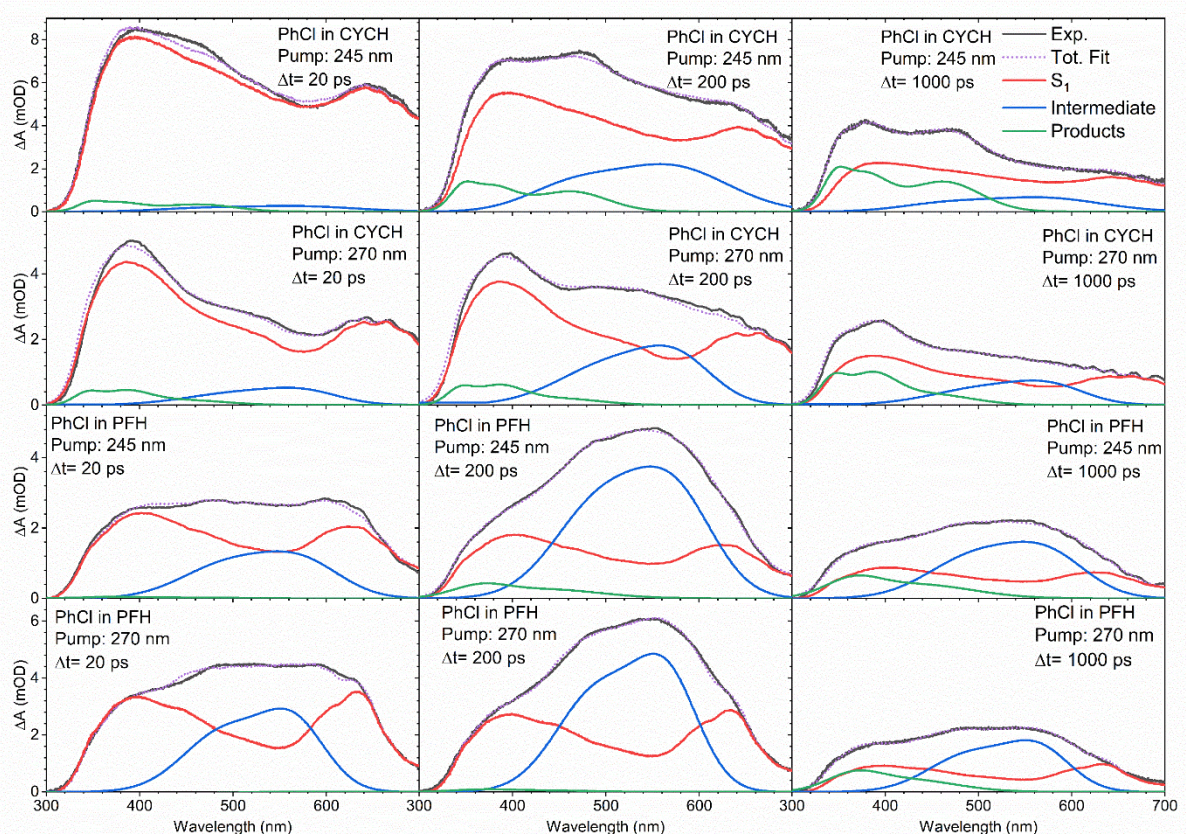

Figure 5- 5. Examples of spectral decomposition of TEA spectra of chlorobenzene for the solvents, time delays and excitation wavelengths shown in each panel. The grey solid line is an experimental spectrum, and the purple dotted line is the total fit spectrum that is the sum of three basis functions: the S_1 state absorption (red), the intermediate absorption (blue) and the products' absorption (green).

The TEA spectra are spectral decomposed using the KOALA software package to extract kinetic information.[37] Examples of this spectral decomposition are shown in Figure 5-5. The analysis uses 3 basis functions for each set of TEA spectra for chlorobenzene in the two different solvents and for the two separate excitation wavelengths. The first basis function is chosen to be the TEA spectrum at an early time delay when the S_1 state is populated and has not evolved to different states; the magnitude of this contribution to the overall spectrum at any time delay will represent the S_1 state population. The second basis function is chosen to capture the band around 540 nm and is obtained as the difference between spectra measured at mid- and early time delays, the latter scaled to account for loss of S_1 absorption. It fits the feature observed to rise at mid time delays, which becomes prominent in the late time spectra. A late-time spectrum was chosen for each set of experimental conditions to describe absorption by photoproducts in the decomposition of TEAS data sets. The product spectra

obtained at longer time delays appear to be distinguishable for different pump wavelengths in cyclohexane, as can be seen in Figure 5-5, which may suggest that the dissociation pathways are different for excitation at 245 nm and 270 nm. In contrast, the product spectra in perfluorohexane do not change obviously with different excitation energies, which suggests that the dissociation pathway in perfluorohexane does not change with different excitation energies. Again, a late-time spectrum was chosen to be the spectral basis function describing the absorption by the photoproducts in PFH solutions.

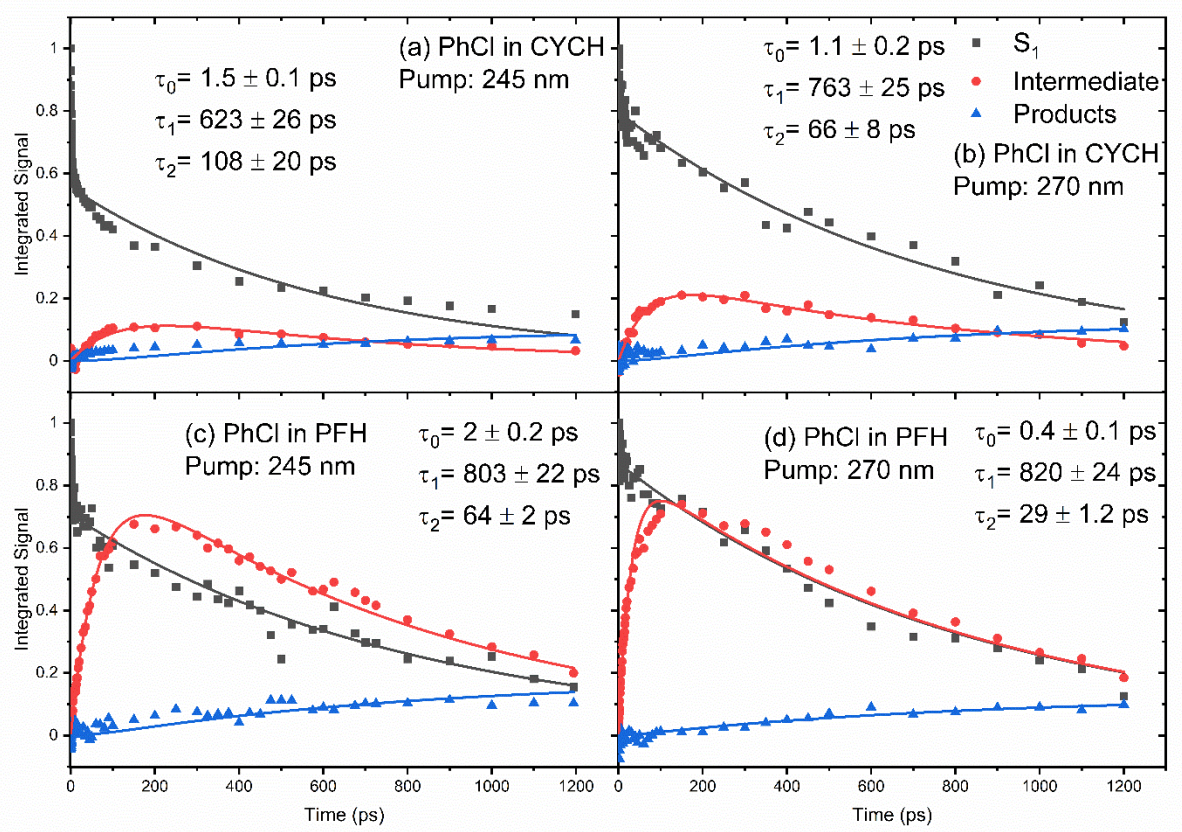

Figure 5- 6. The kinetics derived from spectral decomposition of TEA spectra for chlorobenzene in (a) cyclohexane with 245 nm excitation, (b) cyclohexane with 270 nm excitation, (c) perfluorohexane with 245 nm excitation, and (d) perfluorohexane with 270 nm excitation. These kinetic traces are globally fitted with exponential functions modelling sequential reaction kinetics (see main text) and shown in the corresponding colours in each panel to extract the time constants listed.

The integrated intensities associated with the fitted basis functions are normalised and plotted as a function of time, and the time constants with errors are obtained from exponential fitting of the kinetic traces shown in Figure 5-6. The kinetic model used here for fitting is based on a consecutive reaction model, that is, $reactant \rightarrow intermediate \rightarrow product$ where the S_1 state corresponds to the reactant. However, the kinetics of the S_1 show

bi-exponential decay, with a fast initial decay component, so an extra time constant is added to the fit function for the S_1 state population. The first of the S_1 decay time constants (τ_0) is around 1 ps, which is assigned as intramolecular vibrational energy redistribution, and the second time constant (τ_1) of around 600 – 800 ps is assigned as the lifetime of the S_1 state because it is similar to the literature value (~750 ps -1ns) reported for gas-phase PhCl when the pump wavelength is 270 nm.[11, 14, 15] This second time constant is slightly smaller following 245 nm excitation in cyclohexane, which could be a result of a component of dissociation by crossing to a repulsive state.[7] However, this pattern cannot be seen for the corresponding measurements made in perfluorohexane; instead, the time constant for the S_1 state lifetime does not change significantly with different excitation wavelengths.

The kinetics of the intermediate absorption band show a rise and a decay. At each excitation wavelength and for each solvent, the decay of the S_1 population, the growth and decay of the intermediate and the rise in product absorption can all be fitted with the same two values for the time constants τ_1 and τ_2, as shown in Figure 5.6. The late-time basis function for the spectral decomposition could therefore represent products of the photochemistry such as aryl radicals, or alternatively triplet-state PhCl formed directly from the S_1 state or via the currently unassigned intermediate species. For instance, the phenyl radical absorbs at ~400 nm,[38, 39] and it can react with oxygen dissolved in solution and form a phenylperoxyl radical absorbing around ~460 nm.[17] Absorption by the T_1 state population following intersystem crossing from the S_1 state has been assigned to appear at wavelengths around 300 nm, and a shoulder of the T_1 state absorption band may be observed extending into our probe window.[6, 17]

The identity of the species responsible for the absorption described by the intermediate basis function remains unknown, but some candidates can be discounted, and alternative suggestions are made here. The amplitude of the contribution from this intermediate basis function is larger for PhCl photoexcited in perfluorohexane compared to cyclohexane, and it may therefore be related to the unique properties of perfluorohexane, namely high gas solubility and chemical inertness. Perfluorohexane can dissolve much more gaseous nitrogen and oxygen than cyclohexane, so the intermediate band might plausibly arise from compounds contained nitrogen or oxygen such as a diazonium cation or phenylperoxyl radical. However, those compounds do not absorb around 560 nm where the intermediate absorption peaks.[17, 23, 40] When it come to the inertness of perfluorohexane, the radical pairs

formed after photodissociation will not react with the solvent, whereas cyclohexane can undergo hydrogen abstraction by a phenyl radical or a chlorine radical forming a cyclohexyl radical and benzene or HCl.[17] Therefore, the radical pairs may have longer lifetimes to undergo electron transfer and form a phenyl cation and chloride anion (i.e. an ion pair) in perfluorohexane. Moreover, the phenyl cation has singlet and triplet spin states. The singlet phenyl cation is more stable than the triplet counterpart, and CASPT2/cc-pVDZ calculations suggest that the singlet phenyl cation absorbs at 186 nm which is beyond our measurement window.[41] However, the geometry of the triplet phenyl cation is close to that of the phenyl radical, so it might be an intermediate between phenyl radical and singlet phenyl cation formation, with a lifetime that is expected to be short although the dynamics have not been simulated.[42] In addition to an ion pair which is considered as two separated ions, the intermediate absorption may come from a charge transfer band of a complex with ion-pair character, denoted here as Ph^{+}-Cl^{-}. The corresponding complexes of tetrachloromethane and chloroform (referred to in the photochemistry and pulsed radiolysis literature as *iso*-CCl_4 and *iso*-$CHCl_3$ because they are isomers of CCl_4 and $CHCl_3$, respectively) exhibit strong ion pair character (e.g. Cl^{-}-$ClCCl_2^{+}$) and have very strong absorptions around 500 nm that closely resemble the intermediate features seen here for PhCl.[43, 44] In addition to the similarity of these distinctive spectral signatures, further evidence for the charge-transfer complexes would require the energic feasibility to be investigated with computations.

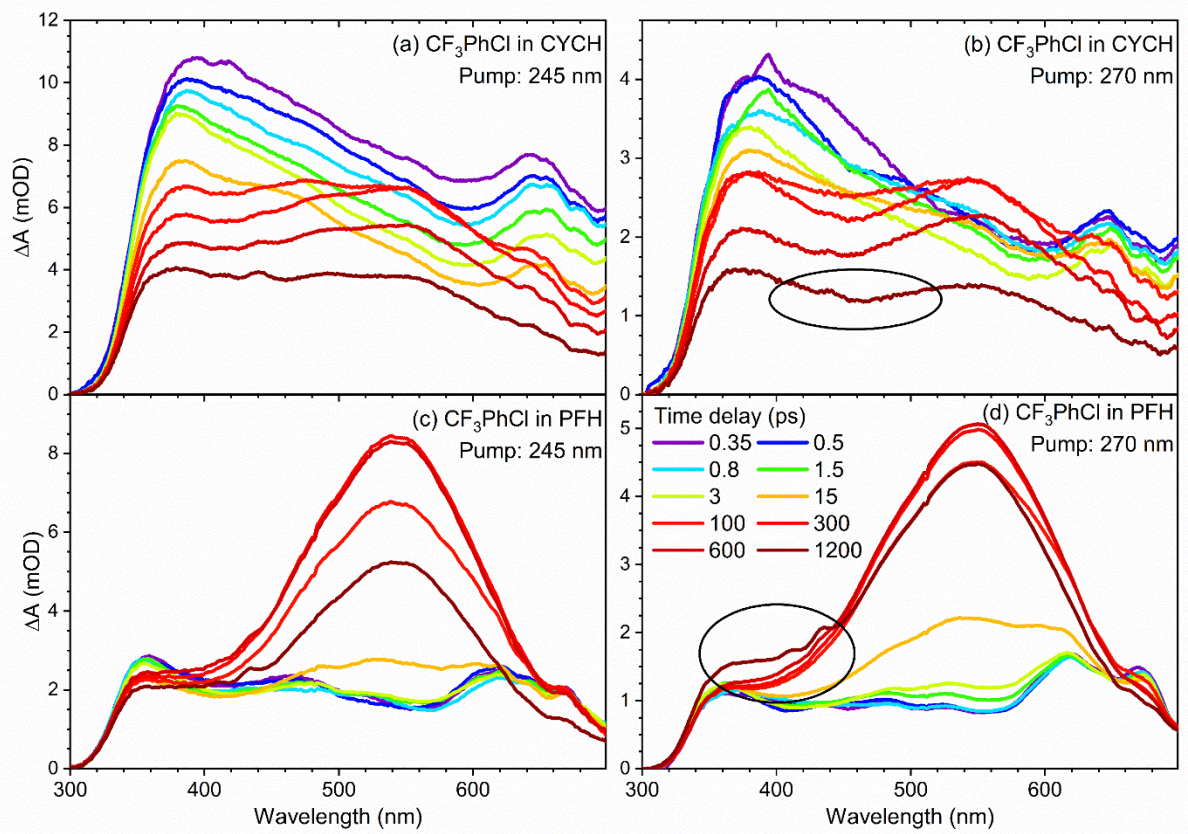

Figure 5- 7. Transient electronic absorption spectra of 1-chloro-4-(trifluoromethyl)benzene in (a) cyclohexane with excitation at 245nm, (b) cyclohexane with excitation at 270 nm, (c) perfluorohexane with excitation at 245 nm, and (d) perfluorohexane with excitation at 270 nm. The time delays of the transient spectra are shown in the colour keys in panel (d).

The TEA spectra of 1-chloro-4-(trifluoromethyl)benzene (CF_3PhCl) were also measured in cyclohexane and perfluorohexane following excitations at 245 nm and 270 nm (Figure 5-7). In cyclohexane, there are bands centred at ~560 nm rising at mid time delays and then decaying, and the relative intensities of these bands compared to the early time spectrum (Δt = 0.35 ps) are higher with excitation at 270 nm than at 245nm, which is similar to observations for the TEA spectra of chlorobenzene.

However, the difference in the relative intensities is less significant than for chlorobenzene TEA spectra. Moreover, the late time spectra of CF_3PhCl are subtly different for the two excitation energies, and the most noticeable differences are circled in Figure 5-7b and d. Although calculations for the excited-state PESs of CF_3PhCl have not been reported, the TEA spectra (Figure 5-7a and 5-7b) suggest that the photodynamics for CF_3PhCl appear to be similar to those for PhCl, with repulsive states that are accessible from high vibrational levels of the S_1 state. In perfluorohexane, the intensities and profiles of the early time spectra for

photoexcited CF_3PhCl are weaker and differ in comparison with the measurements in cyclohexane. This behaviour is not seen for chlorobenzene and may result from the excited state absorption shifting to shorter wavelengths, outside our probe window. The intermediate bands around 560 nm are stronger in perfluorohexane, and the late time spectra of CF_3PhCl in perfluorohexane do not show clearcut pump wavelength dependence, although the intensity of the product band at 400 nm in the late-time spectrum in perfluorohexane (Δt= 1200 ps) is somewhat stronger with the 270 nm pump than with the 245 nm pump. As a result, a similar approach to spectral decomposition is applied for TEA spectra of CF_3PhCl: three basis functions are used, and are labelled as absorption by the S_1 state, an intermediate, and products. Examples of the spectral decomposition are shown in Figure 5-8 at the end of this chapter. The kinetics corresponding to evolution of the contributions from each basis function used in the analysis of CF_3PhCl TEA spectra are fitted with the same sequential

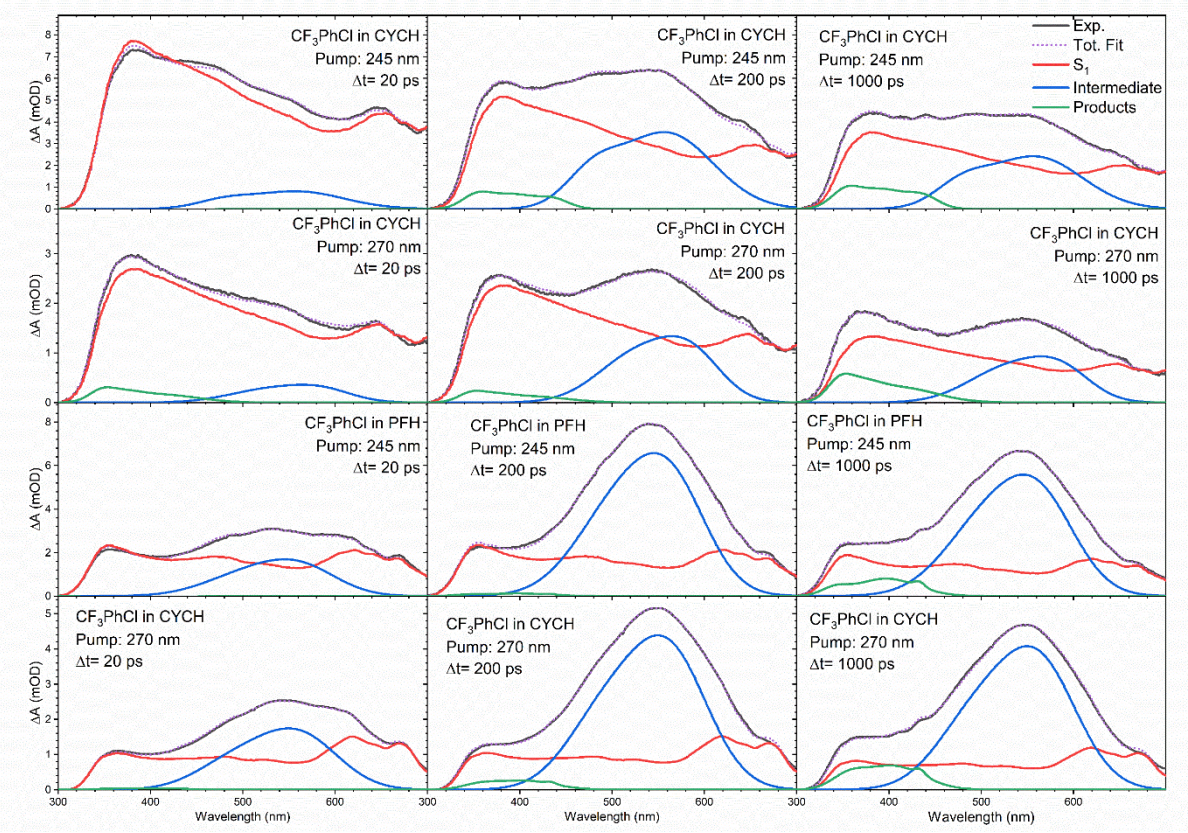

Figure 5- 8. Examples of spectral decomposition of TEA spectra of CF_3PhCl for the solvents, time delays and excitation wavelengths shown in each panel. The grey solid line is an experimental spectrum, and the purple dotted line is the total fit spectrum that is the sum of three basis functions: the S_1 state absorption (red), the intermediate absorption (blue) and the products' absorption (green).

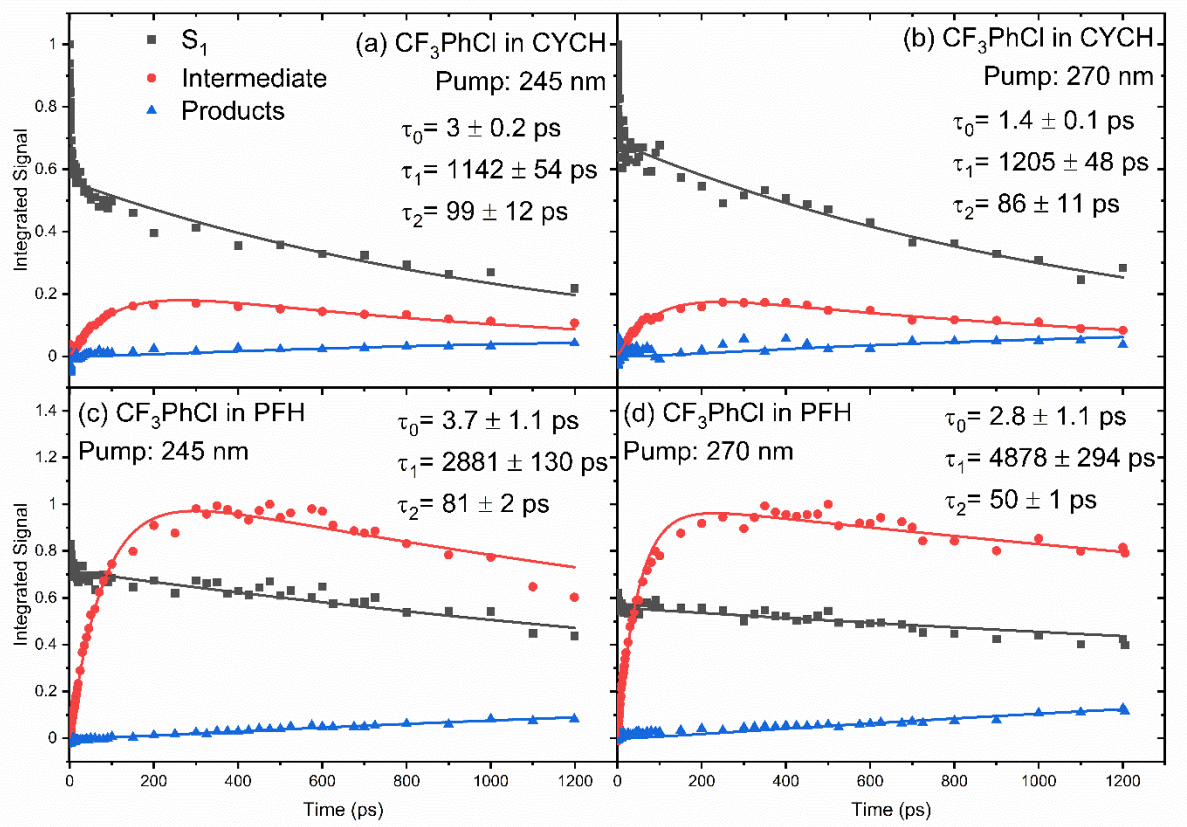

Figure 5- 9. The kinetics from spectral decomposition of TEA spectra of CF_3PhCl in (a) cyclohexane with 245 nm excitation, (b) cyclohexane with 270 nm excitation, (c) perfluorohexane with 245 nm excitation and (d) perfluorohexane with 270 nm excitation are global fitted with exponential function. The time constants are shown with corresponding colours in each panel.

reaction model as was used for chlorobenzene, and the results are shown in Figure 5-9. The time constants observed in CF_3PhCl are longer than for chlorobenzene, especially in perfluorohexane. For example, the time constant τ_1, describing S_1 population decay and formation of the intermediates, is larger than our time measurement window. Therefore, the derived values of the time constants are not reliable, although the kinetic analysis shows the S_1 state has a longer lifetime in perfluorohexane.

A limitation of the TEAS measurements reported here is that the UV-Vis absorption bands are broad, and it is therefore difficult to distinguish species based on the TEA spectra alone because of the spectral overlaps. Time-resolved infra-red spectroscopy might therefore be a more fruitful way to progress. Figure 5-10 shows the FTIR absorption spectra of PhCl and CF_3PhCl, and plans for transient vibrational absorption spectroscopy (TVAS) will be discussed in the next section.

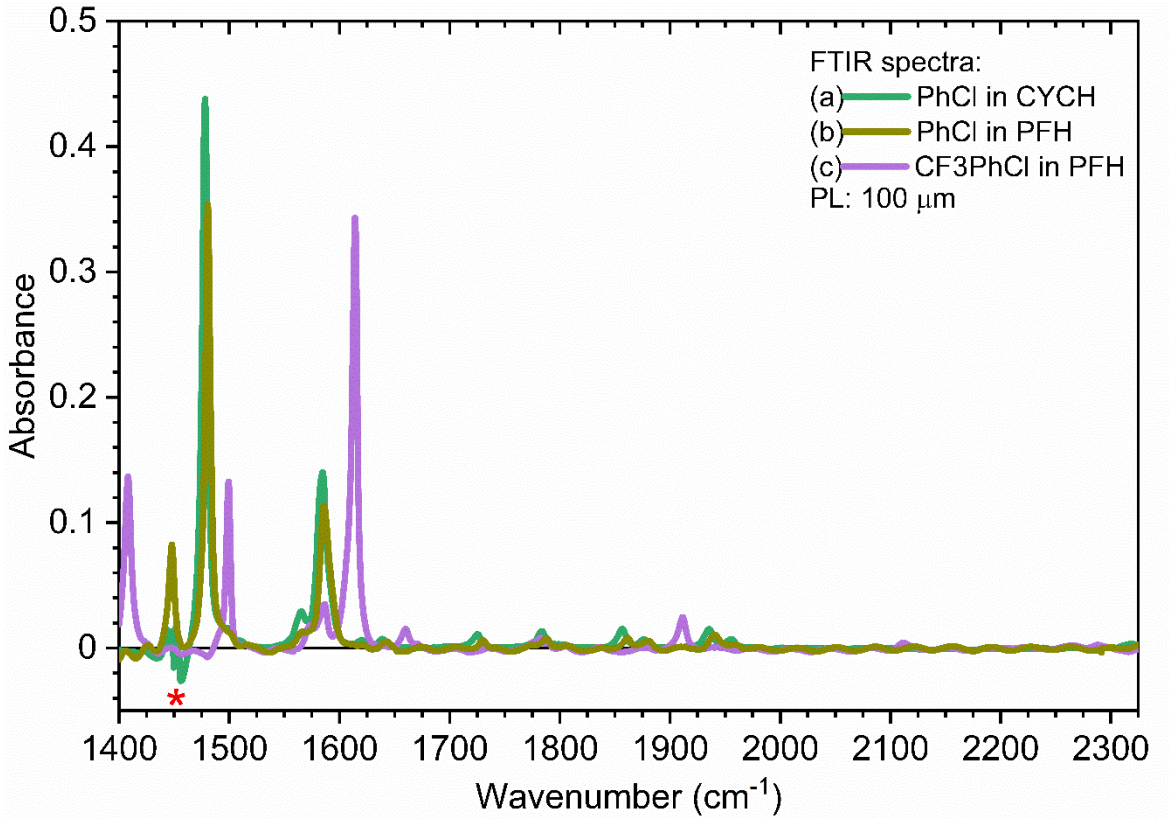

Figure 5- 10. Steady state FTIR absorption spectra of (a) chlorobenzene in cyclohexane, (b) chlorobenzene in perfluorohexane and (c) 1-chloro-4-(trifluoromethyl)benzene in perfluorohexane. The red star sign at ~ 1450 cm^{-1} is where cyclohexane absorption saturates.

5.4 Future plans

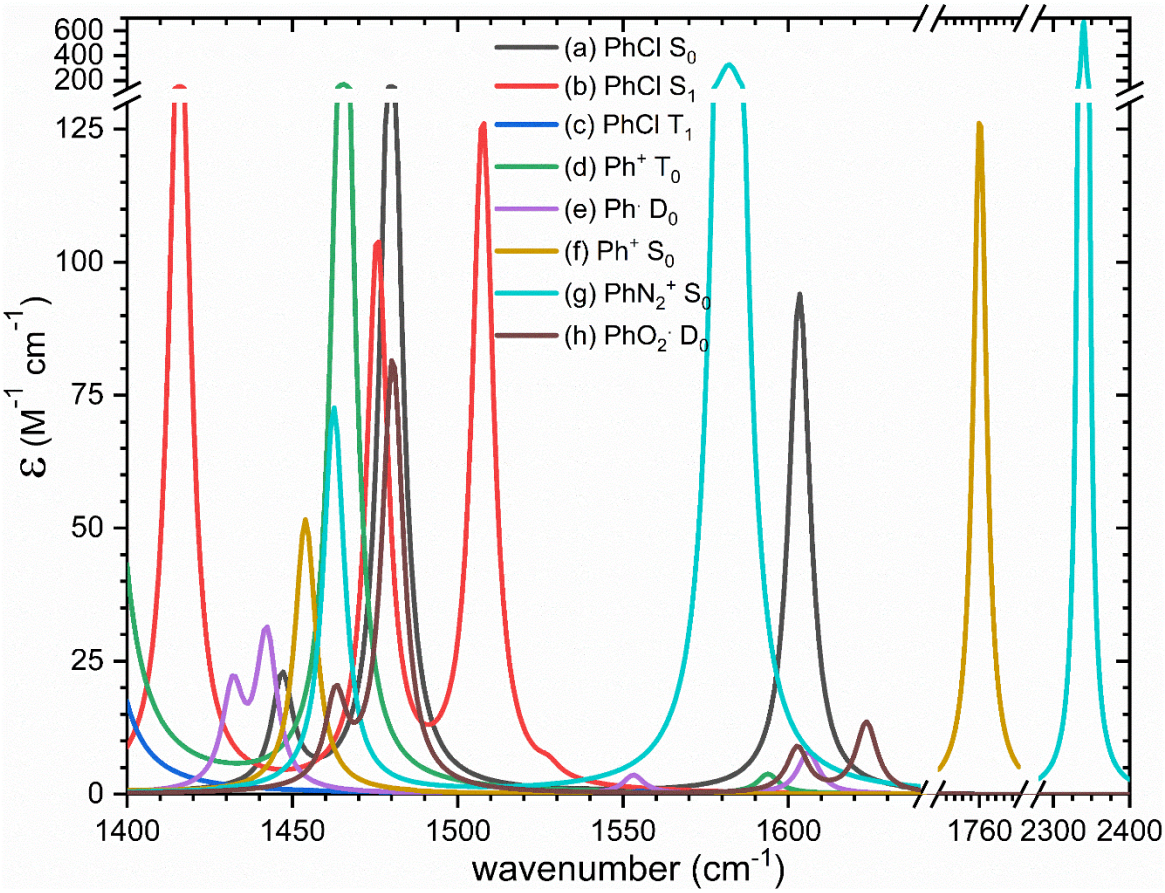

Figure 5- 11. The scaled calculated IR spectra of (a) chlorobenzene, (b) chlorobenzene in the S_1 state, (c) chlorobenzene in the T_1 state, (d) triplet phenyl cation, (e) phenyl radical, (f) singlet phenyl cation, (g) diazonium cation and (h) phenylperoxyl radical. The wavenumber scaling factor is 0.965, and the half-width at half height used is 4 cm^{-1} which is representative of the experimental resolution.

Transient vibrational absorption spectroscopy is likely to be more useful in distinguishing the intermediates and photoproducts because the IR absorption peaks are narrower. Taking chlorobenzene as an example, the calculated vibrational spectra of species of interest are shown in Figure 5-11. Despite the strongly overlapping absorptions from 1400 cm^{-1} to 1500 cm^{-1}, the crucial target species for this project, such as singlet phenyl cation and diazonium ion introduced in Chapter 1.4 should have distinct absorptions at 1760 cm^{-1} and 2240 cm^{-1}, respectively. Probing the TVA spectra around 2240 cm^{-1} could give a direct answer to whether diazonium ions can be formed in 1.2 ns by photoexciting solutions of chlorobenzene and dissolved N_2. Moreover, monitoring the kinetics of the singlet phenyl cation absorption at 1760 cm^{-1} could reveal whether homolysis is followed by electron transfer or heterolysis

happens during bond dissociation by crossing to an excited state with ion-pair character. If both of these two proposed products are not formed on our time scale, the TVA spectra around 1450 cm^{-1} should be sufficiently clear to identify phenyl radicals. TVAS experiments will therefore be conducted with the same pump wavelengths and solvents to reveal more about the photodynamics of chlorobenzene and CF_3PhCl.

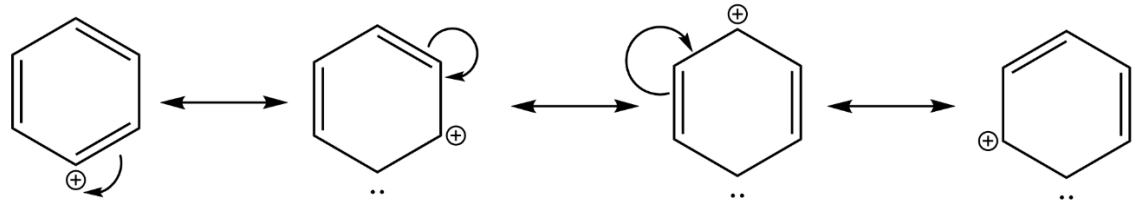

Figure 5- 12. Resonance structures of phenyl cation.

The structure of the proposed ion-pair complex Ph^+-Cl^- will be computed, and its calculated spectra could help to assign the intermediate absorption band seen in the TEA spectra. To find the potential structures of Ph^+-Cl^-, the resonance structures of phenyl cation (Figure 5-12) can be used to suggest which carbon atoms carry greater partial positive charges, and hence are more likely to bind the partner chloride ion. This analysis identifies the ortho- and the para-sites as the starting points for calculations to explore where the chloride ion might attach to make an *iso*-chlorobenzene species with both ion-pair and carbene character that makes the species too reactive with cyclohexane to be observed, whereas perfluorocarbons do not react with carbenes.[25, 45] The energies of *iso*-chlorobenzene species with optimised structures will be checked to confirm that they are energetically accessible under the reported experimental conditions.

5.5 Summary

The kinetics of chlorobenzene and 1-chloro-4-(trifluoromethyl)benzene photoexcited to the S_1 states are investigated with TEAS in cyclohexane and perfluorohexane solutions and at two different excitation wavelengths. The TEA spectra are spectrally decomposed into three components corresponding to absorption from the S_1 state, an intermediate, and photoproducts. In cyclohexane, the lifetime of the S_1 chlorobenzene is ~750 ps when excited by 270 nm UV, but the lifetime decreases to ~623 ps with 245 nm excitation. The growth and decay of the intermediate and the rise in product absorption are fitted with two time constants τ_1 (~750 ps, matching the S_1 decay) and τ_2 (<100ps). Moreover, there are absorption

bands attributed to photoproducts in the late time TEA spectra, and the profiles of these late time spectra differ with different excitation wavelengths. These observations suggest that another photodissociation pathway is available for more highly vibrationally excited S_1 state PhCl, populating a repulsive T_5 state. The TEA spectra of CF_3PhCl in cyclohexane show somewhat similar behaviour to chlorobenzene, such as an intermediate rising and decaying, and pump-wavelength dependent late time spectra, but the time constants observed in CF_3PhCl are larger, and the lifetime of the S_1 state does not decrease significantly with use of a 245 nm pump wavelength. In perfluorohexane, not only the lifetimes of the S_1 chlorobenzene but also the late time spectra barely change with excitation wavelength, and the time constants for CF_3PhCl S_1 decay are larger and beyond our time window. However, the intensities of the intermediate bands are more prominent for both PhCl and CF_3PhCl, which could be related to the unique solvent properties of perfluorohexane, i.e., high gas solubility and chemical inertness. Calculated IR spectra indicate that TVAS would be useful to identify more precisely the intermediates and photoproducts and reveal the possible mechanism of phenyl cation generation.

References

1. V. Dichiarante, S. Protti and M. Fagnoni, *J. Photochem. Photobiol. A*, 2017, **339**, 103-113.
2. M. Fagnoni and V. Dichiarante, *Synlett*, 2008, **2008**, 787-800.
3. A. Y. Li, F. P. M. Jjunju and R. G. Cooks, *J. Am. Soc. Mass Spectrom.*, 2013, **24**, 1745-1754.
4. S. Protti, V. Dichiarante, D. Dondi, M. Fagnoni and A. Albini, *Chem. Sci.*, 2012, **3**, 1330.
5. X. Xu, J. Dai, X. Guo, C. Qian, P. Zhang, Y. Duan and Y. Tian, *Phys Chem Chem Phys*, 2021, **23**, 10763-10767.
6. S. Lazzaroni, S. Protti, M. Fagnoni and A. Albini, *J Photoch Photobio A*, 2010, **210**, 140-144.
7. Y.-J. Liu, P. Persson and S. Lunell, *J. Chem .Phys.*, 2004, **121**, 11000.
8. T. Ichimura, Y. Mori, H. Shinohara and N. Nishi, *Chem. Phys. Lett.*, 1985, **122**, 51-54.
9. A. Freedman, S. C. Yang, M. Kawasaki and R. Bersohn, *J. Chem .Phys.*, 1980, **72**, 1028-1033.
10. T. Ichimura, Y. Mori, H. Shinohara and N. Nishi, *Chem. Phys.*, 1994, **189**, 117-125.
11. M. Kadi, J. Davidsson, A. N. Tarnovsky, M. Rasmusson and E. Åkesson, *Chem. Phys. Lett.*, 2001, **350**, 93-98.
12. G.-J. Wang, R.-S. Zhu, H. Zhang, K.-L. Han, G.-Z. He and N.-Q. Lou, *Chem. Phys. Lett.*, 1998, **288**, 429-432.

13. N. E. Sveum, S. J. Goncher and D. M. Neumark, *Phys. Chem. Chem. Phys.*, 2006, **8**, 592-598.
14. Y. Z. Liu, C. C. Qin, S. Zhang, Y. M. Wang and B. Zhang, *Acta Phys.-Chim. Sin.*, 2011, **27**, 965-970.
15. C. M. Previtali and T. W. Ebbesen, *J. Photochem.*, 1984, **27**, 9-15.
16. M. H. Palmer, T. Ridley, S. V. Hoffmann, N. C. Jones, M. Coreno, M. de Simone, C. Grazioli, T. Zhang, M. Biczysko, A. Baiardi and K. A. Peterson, *J. Chem .Phys.*, 2016, **144**, 21.
17. J. P. Da Silva, S. Jockusch and N. J. Turro, *Photochem. Photobiol. Sci.*, 2009, **8**, 210-216.
18. J. P. Da Silva, L. F. Vieira Ferreira, I. Osipov and I. Ferreira Machado, *J. Hazard. Mater.*, 2010, **179**, 187-191.
19. V. Butcher, M. L. Costa, J. M. Dyke, A. R. Ellis and A. Morris, *Chem. Phys.*, 1987, **115**, 261-267.
20. U. Berzinsh, M. Gustafsson, D. Hanstorp, A. Klinkmüller, U. Ljungblad and A.-M. Mårtensson-Pendrill, *Phys. Rev. A*, 1995, **51**, 231-238.
21. J. D. D. Martin and J. W. Hepburn, *J. Chem .Phys.*, 1998, **109**, 8139-8142.
22. M. Mella, P. Coppo, B. Guizzardi, M. Fagnoni, M. Freccero and A. Albini, *J. Org. Chem.*, 2001, **66**, 6344-6352.
23. S. Milanesi, M. Fagnoni and A. Albini, *Chem. Commun.*, 2003, 216-217.
24. J. M. Swanson, C. A. Dvorak, J. P. Deluca and J. M. Standard, *J. Org. Chem.*, 1994, **59**, 3026-3032.
25. N. J. Turro, Y. Cha and I. R. Gould, *J. Am. Chem. Soc.*, 1987, **109**, 2101-2107.
26. M. Ragaller, J. U. Bleyl, T. Koch and D. M. Albrecht, *Anaesthesist*, 2000, **49**, 291-301.
27. T. J. Kemp, *Prog. React. Kinet.*, 2003, **28**, 11-34.
28. C. Raviola, D. Ravelli, S. Protti, A. Albini and M. Fagnoni, *Synlett*, 2015, **26**, 471-478.
29. T. Yanai, D. P. Tew and N. C. Handy, *Chem. Phys. Lett.*, 2004, **393**, 51-57.
30. R. A. Kendall, T. H. Dunning and R. J. Harrison, *J. Chem. Phys.*, 1992, **96**, 6796-6806.
31. D. E. Woon and T. H. Dunning, *J. Chem. Phys.*, 1993, **98**, 1358-1371.
32. A. D. Becke, *J. Chem. Phys.*, 1993, **98**, 5648-5652.
33. W. Kohn and L. J. Sham, *Phys. Rev.*, 1965, **140**, A1133-A1138.
34. R. Bauernschmitt and R. Ahlrichs, *Chem. Phys. Lett.*, 1996, **256**, 454-464.
35. M. E. Casida, C. Jamorski, K. C. Casida and D. R. Salahub, *J. Chem .Phys.*, 1998, **108**, 4439-4449.
36. M. J. Frisch, G. W. Trucks, H. B. Schlegel, G. E. Scuseria, M. A. Robb, J. R. Cheeseman, G. Scalmani, V. Barone, B. Mennucci, G. A. Petersson, H. Nakatsuji, M. Caricato, X. Li, H. P. Hratchian, A. F. Izmaylov, J. Bloino, G. Zheng, J. L. Sonnenberg, M. Hada, M. Ehara, K. Toyota, R. Fukuda, J. Hasegawa, M. Ishida, T. Nakajima, Y. Honda, O. Kitao, H. Nakai, T. Vreven, J. A. Montgomery, J. E. Peralta, F. Ogliaro, M. J. Bearpark, J. J. Heyd, E. Brothers, K. N. Kudin, V. N. Staroverov, R. Kobayashi, J. Normand, K. Raghavachari, A. Rendell, J. C. Burant, S. S. Iyengar, J. Tomasi, M. Cossi, N. Rega, J. M. Millam, M. Klene, J. E. Knox, J. B. Cross, V. Bakken, C. Adamo, J. Jaramillo, R. Gomperts, R. E. Stratmann, O. Yazyev, A. J. Austin, R. Cammi, C. Pomelli, J. W. Ochterski, R. L. Martin, K. Morokuma, V. G. Zakrzewski, G. A. Voth, P. Salvador, J. J. Dannenberg, S. Dapprich, A. D. Daniels, O. Farkas, J. B. Foresman, J. V. Ortiz, J. Cioslowski and D. J. Fox, *Gaussian 09, Revision D.01*, 2013.
37. M. P. Grubb, A. J. Orr-Ewing and M. N. R. Ashfold, *Rev. Sci. Instrum.*, 2014, **85**, 064104.
38. J. M. Engert and B. Dick, *Appl. Phys. B*, 1996, **63**, 531-535.

39. J. G. Radziszewski, *Chem. Phys. Lett.*, 1999, **301**, 565-570.
40. M. Slegt, H. S. Overkleeft and G. Lodder, *Eur. J. Org. Chem.*, 2007, **2007**, 5364-5375.
41. D. M. Smith, Z. B. Maksic and H. Maskill, *J. Chem. Soc.-Perkin Trans. 2*, 2002, DOI: 10.1039/b200898j, 906-913.
42. J. N. Harvey, M. Aschi, H. Schwarz and W. Koch, *Theor. Chem. Acc.*, 1998, **99**, 95-99.
43. F. Abou-Chahine, T. J. Preston, G. T. Dunning, A. J. Orr-Ewing, G. M. Greetham, I. P. Clark, M. Towrie and S. A. Reid, *J. Phys. Chem. A*, 2013, **117**, 13388-13398.
44. R. E. Bühler and B. Hurni, *Helvetica Chimica Acta*, 1978, **61**, 90-96.
45. J. Wang, G. Burdzinski, J. Kubicki and M. S. Platz, *J. Am. Chem. Soc.*, 2008, **130**, 11195-11209.

Chapter 6. Conclusions

The effects of molecular structures and solvent environments on the ultrafast photoreactions of various organic molecules in solutions, investigated with transient absorption spectroscopy, are reported in this thesis. Ring strain effects on the potential energy surfaces along the Norrish type I reaction coordinate in the S_1 state were studied for three different ring sizes of cyclic ketones: cyclobutanone, cyclopentanone and cyclohexanone.[1] Solutions of these ketones in cyclohexane were photoexcited to different vibrational levels of the S_1 state with 255 nm, 281 nm, 290 nm, and 312 nm UV pump wavelengths. The early time TEA spectra of the cyclic ketones showed pump-wavelength dependence, with an excited state absorption (ESA) feature around 600 nm not as distinct with 312 nm excitation as when the three shorter excitation wavelengths were used. As a result, spectral decompositions used a spectral basis function extracted from the early time TEA spectra that represented the vibrationally hot population of the S_1 state of each of the cyclic ketones. A second basis function was introduced, when necessary, and was derived from medium-time or late-time transient spectra. It was interpreted as ESA from the vibrationally relaxed S_1-state population below the energy barrier for Norrish-type α-cleavage. The kinetics of the TEA spectra, obtained with different excitation wavelengths for each cyclic ketone, were globally fitted with common time constants to compare the lifetimes of different components and their amplitudes.

For all three cyclic ketones, the extracted time constants were on time scales of ≤1 ps, 7-9 ps and >500 ps. The first component was assigned to prompt cleavage of an α-C-C bond, and the second component to vibrational cooling of the hot S_1 state molecules to low-lying vibrational levels of the S_1 state. Finally, slow loss of thermalised S_1 state population via α-cleavage and internal conversion or intersystem crossing to other states such as the ground state or first excited triplet (T_1) state occurred with time constants >500 ps that became larger with larger ring size. The relative contribution of prompt α-cleavage increased with higher ring strain and with shorter excitation wavelength because the energy barrier to bond dissociation on the S_1 PES is reduced by this greater ring strain in cyclobutanone (Figure 6-1a). The three time constants could also be fitted to the kinetics measured with transient infra-red absorption spectroscopy. A photoproduct ketene compound was observed from photoexcited cyclobutanone within 1 ns (Figure 6-1b). On the other hand, the absence of ketene signatures

from photoexcited cyclopentanone and cyclohexanone suggested that other competitive reaction pathways following α-cleavage dominated, or the pathway to ketene formation was via the T_1 state, and occurred on timescales beyond the experimental time-delay window.

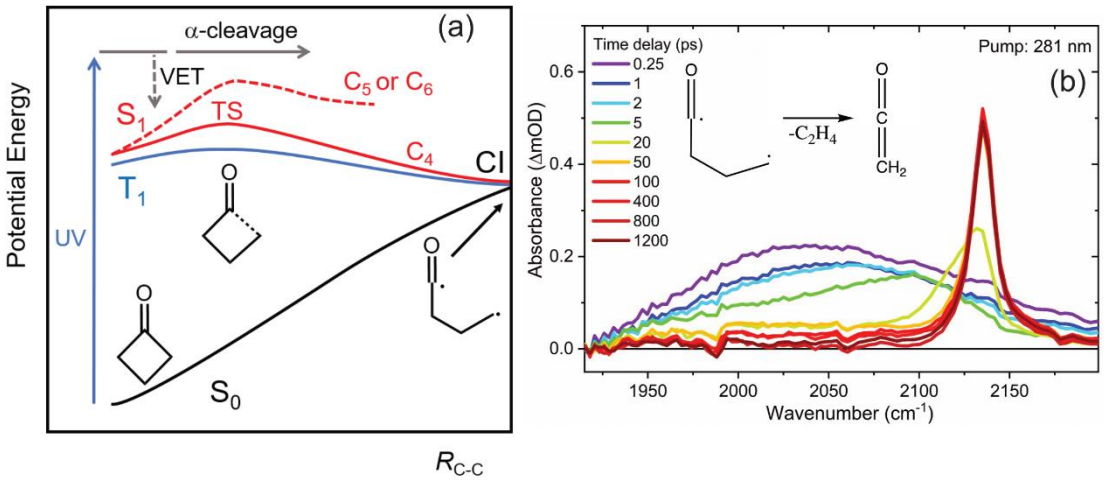

Figure 6- 1. Photochemistry of cyclic ketones. (a) Schematic potential energy surfaces of cyclic ketones along the α C-C bond extension coordinate (R_{C-C}). The greater ring strain of cyclobutanone (denoted as C_4) than other two cyclic ketones results in the smaller energy barrier to bond dissociation. (b) a photoproduct, ketene, was observed within 1 ns after α-cleavage on the S_1 state.

In addition to these systematic studies of how changes in molecular structure affect the photodynamics of organic molecules, the work presented in this thesis examined how the surrounding solvent influence photochemical outcomes. The system chosen for study was the solvent-environment dependent competition between alternative relaxation pathways of a sunscreen molecule, DHHB, again using ultrafast transient absorption spectroscopy. DHHB has two tautomers, the keto and enol forms. In the ground state, the enol form was shown to be more stable, with the tautomerisation pathway from the keto form to the enol form being barrierless. When DHHB was photoexcited to the S_1 state, it underwent two competing relaxation pathways: excited state hydrogen transfer (ESHT) to the keto form or geometric and vibrational relaxation to a twisted enol form (Figure 6-2a). To understand the effect of the solvent environment on the competition between these two pathways, four solvents were chosen to provide nonpolar (cyclohexane), aprotic polar (acetonitrile), viscous aprotic polar (DMSO) and protic polar (methanol) environments. In polar solvents, a strong stimulated emission feature was seen in the early time TEA spectra, and the intensity was stronger in protic environments, whereas the emission was weak in nonpolar environments.

Calculated energy scans along the ESHT coordinate, with the solvent treated using the CPCM method,[2, 3] revealed a small barrier for a DHHB in methanol solution, whereas no such barrier was found for DHHB in cyclohexane. Therefore, the stimulated emission was assigned to be from the vibrationally hot S_1 enol because the ESHT was inhibited in polar solvents. This hot S_1 enol decayed by relaxation to the minimum energy twisted S_1 enol structure, with torsional dynamics occurring with a time constant of 300 - 800 fs, seemingly related to the viscosity of the solvent.

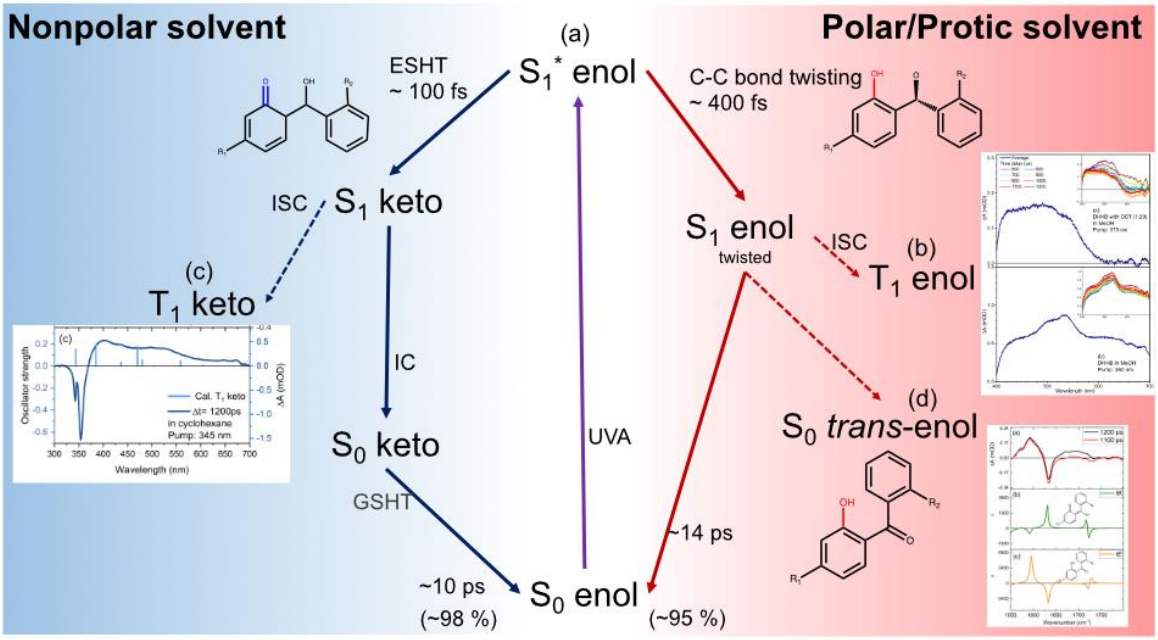

Figure 6- 2. Solvent environment dependent photochemistry of DHHB. (a) Photoexcited DHHB in the S_1 state has two relaxation pathways: excited state hydrogen transfer (ESHT) to the S_1 keto form and C-C bond twisting to the twisted S_1 enol form. (b) The absorption by the T_1 enol is seen in polar solvents, and it can be quenched by addition of a triplet quencher. (c)The T_1 keto absorptions dominant in nonpolar solvents at later time delays. (d) The formation of a photoproduct, *trans*-enol, is observed in polar solvents, and it is suspected to result from further C-C bonding twisting of the enol form in the ground electronic state.

In addition, the late time TEA spectra of DHHB also showed solvent-dependent absorption profiles. In polar solvents, there were absorption bands around 600 nm - 700 nm after time delays of 1 ns, but in a nonpolar environment, these features were significantly weaker. The absorption bands could be quenched by the triplet quenchers octocrylene and *trans*-β-methylstryene, both with similar triplet energies,[4, 5] and the calculated UV-Vis absorption spectra of the T_1 enol and T_1 keto tautomers suggested that the absorption features resulted

from the T_1 enol (Figure 6-2b). The remaining absorptions observed after addition of the quenchers arose from the T_1 keto form, which is dominant in nonpolar solvents (Figure 6-2c). These observations of the late time spectra supported the interpretation that the ESHT was less favourable in polar solvents, so the population of the S_1 enol was larger and intersystem crossing to the T_1 enol was encouraged. The kinetics of the DHHB ground state bleach observed by TEAS and TVAS revealed recovery of ground-state molecules within 10 - 25 ps, with ~95% recovery in polar solvents and ~98% in nonpolar solvents within 1 ns. Additionally, a photoproduct, *trans*-enol, was observed in polar solvents (Figure 6-2d), but too little was produced in nonpolar solvents to be observed. The formation of the *trans*-enol photoproduct was suspected to be a consequence of further torsional dynamics of internally excited molecules on the potential energy surface of the S_0 enol, and the lifetime of this metastable photoproduct was longer than 2 ns.

Not only the polarity of solvents but also the chemical properties of the solvents can affect the photochemical pathways of solute molecules. This behaviour was illustrated by the photodissociation of chlorobenzene and 1-chloro-4-(trifluoromethyl)benzene, both of which were studied in cyclohexane and perfluorohexane. To explore the possible dissociation pathways, experiments used two different excitation energies to populate the high and low vibrational levels of the S_1 state, respectively. In cyclohexane, the profiles of the late time transient absorption spectra showed a pump wavelength dependence, but such dependence was not noticeable in the chemically inert solvent perfluorohexane. The TEA spectra were decomposed into three contributions using basis functions assigned to absorption from the S_1 state, an intermediate, and photoproducts. Moreover, the intermediate absorption bands lying between 500 and 600 nm were stronger for measurements made in perfluorohexane than in cyclohexane. The kinetics of these different spectral components were fitted to a sequential reaction model, giving lifetimes for the S_1 state (denoted as τ_1) and the intermediate species (τ_2). The lifetimes of the S_1 state were τ_1 ~ 800 ps for chlorobenzene and 1-5 ns for CF_3PhCl in both solvents. The corresponding lifetimes for the decay of intermediates and growth of products in both solvents were significantly shorter at $\tau_2 < 100$ ps. Plausible candidates for the intermediate species were proposed to be reactive species such as phenyl radicals, phenyl cations or, most likely, phenyl-cation / chloride-anion charge transfer complexes with carbene character that allowed reaction with cyclohexane but not perfluorohexane solvents. Consequently, stronger intermediate bands were observed in

perfluorohexane. Calculated IR spectra showed that transient infra-red absorption spectroscopy could be used to identify more precisely the intermediates and products, and the photochemical reaction mechanisms of chlorobenzene and CF_3PhCl in solution could then be more fully interpreted.

As the work in this thesis has illustrated, transient absorption spectroscopy can reveal thorough details about photo-induced reaction mechanisms in different solvents by direct observations of the excited states and intermediates generated on picosecond time scales. The examples studied show that the photochemical dynamics are dependent on modifications to the solute structure, and choice of UV excitation wavelength and solvent. Although gas phase studies using techniques such as time-resolved photoelectron spectroscopy or mass spectrometry provide some guidance about possible photochemical pathways in solution, these pathways can be significantly modified by the solvent. This is especially the case if there are competing pathways open to the excited molecules, because the balance of the competition can be changed by the solvent environment. This work examining the structural and environmental influences on photochemical dynamics therefore has implications for research in a number of fields such as photochemical organic synthesis,[6, 7] how different formulations influence sunscreen performance,[8, 9] and N_2 or CO activation using photoexcited organic molecules.[10, 11]

References

1. S. H. Xia, X. Y. Liu, Q. Fang and G. Cui, *J. Phys. Chem. A.*, 2015, **119**, 3569-3576.
2. V. Barone and M. Cossi, *J. Phys. Chem. A*, 1998, **102**, 1995-2001.
3. M. Cossi, N. Rega, G. Scalmani and V. Barone, *J. Comput. Chem.*, 2003, **24**, 669-681.
4. A. Kikuchi, Y. Nakabai, N. Oguchi-Fujiyama, K. Miyazawa and M. Yagi, *J. Lumines.*, 2015, **166**, 203-208.
5. P. M. Crosby, J. M. Dyke, J. Metcalfe, A. J. Rest, K. Salisbury and J. R. Sodeau, *J. Chem. Soc.-Perkin Trans. 2*, 1977, 182-185.
6. G. Quinkert, *Angew Chem Int Edit*, 1965, **4**, 211-&.
7. J. A. Dantas, J. T. M. Correia, M. W. Paixão and A. G. Corrêa, *ChemPhotoChem*, 2019, **3**, 506-520.
8. P. Zhou, M. R. Hoffmann, K. Han and G. He, *J. Phys. Chem. B*, 2015, **119**, 2125-2131.
9. E. M. M. Tan, M. Hilbers and W. J. Buma, *J. Phys. Chem. Lett.*, 2014, **5**, 2464-2468.
10. X. Xu, J. Dai, X. Guo, C. Qian, P. Zhang, Y. Duan and Y. Tian, *Phys. Chem. Chem. Phys.*, 2021, **23**, 10763-10767.
11. M. Winkler and W. Sander, *J. Org. Chem.*, 2006, **71**, 6357-6367.